

1 A modular framework for multiscale, multicellular, spatiotemporal  
2 modeling of acute primary viral infection and immune response in  
3 epithelial tissues and its application to drug therapy timing and  
4 effectiveness

5 A multiscale model of viral infection in epithelial tissues

6  
7 T.J. Segó<sup>1,2\*</sup>, Josua O. Aponte-Serrano<sup>1,2\*</sup>, Juliano Ferrari Gianlupi<sup>1,2</sup>, Samuel R. Heaps<sup>1</sup>,  
8 Kira Breithaupt<sup>1,3</sup>, Lutz Brusch<sup>4</sup>, Jessica Crawshaw<sup>5</sup>, James M. Osborne<sup>5</sup>, Ellen M.  
9 Quardokus<sup>1</sup>, Richard K. Plemper<sup>6</sup>, James A. Glazier<sup>1,2</sup>

10 <sup>1</sup> Department of Intelligent Systems Engineering, Indiana University, Bloomington, IN, USA

11 <sup>2</sup> Biocomplexity Institute, Indiana University, Bloomington, IN, USA

12 <sup>3</sup> Cognitive Science Program, Indiana University, Bloomington, IN, USA

13 <sup>4</sup> Center for Information Services and High Performance Computing (ZIH), Technische Universität Dresden, Germany

14 <sup>5</sup> School of Mathematics and Statistics, University of Melbourne, Melbourne, 3010, Australia

15 <sup>6</sup> Institute for Biomedical Sciences, Georgia State University, Atlanta, GA, USA

16 \* These Authors contributed equally to this study

17

18 **Abstract**

19 Simulations of tissue-specific effects of primary acute viral infections like COVID-  
20 19 are essential for understanding disease outcomes and optimizing therapies. Such  
21 simulations need to support continuous updating in response to rapid advances in  
22 understanding of infection mechanisms, and parallel development of components by  
23 multiple groups. We present an open-source platform for multiscale spatiotemporal  
24 simulation of an epithelial tissue, viral infection, cellular immune response and tissue  
25 damage, specifically designed to be modular and extensible to support continuous  
26 updating and parallel development. The base simulation of a simplified patch of epithelial  
27 tissue and immune response exhibits distinct patterns of infection dynamics from  
28 widespread infection, to recurrence, to clearance. Slower viral internalization and faster  
29 immune-cell recruitment slow infection and promote containment. Because antiviral drugs  
30 can have side effects and show reduced clinical effectiveness when given later during

31 infection, we studied the effects on progression of treatment potency and time-of-first  
32 treatment after infection. In simulations, even a low potency therapy with a drug which  
33 reduces the replication rate of viral RNA greatly decreases the total tissue damage and  
34 virus burden when given near the beginning of infection. Many combinations of dosage  
35 and treatment time lead to stochastic outcomes, with some simulation replicas showing  
36 clearance or control (treatment success), while others show rapid infection of all epithelial  
37 cells (treatment failure). Thus, while a high potency therapy usually is less effective when  
38 given later, treatments at late times are occasionally effective. We illustrate how to extend  
39 the platform to model specific virus types (e.g., hepatitis C) and add additional cellular  
40 mechanisms (tissue recovery and variable cell susceptibility to infection), using our  
41 software modules and publicly-available software repository.

42

### 43 **Author summary**

44 This study presents an open-source, extensible, multiscale platform for simulating  
45 viral immune interactions in epithelial tissues, which enables the rapid development and  
46 deployment of sophisticated models of viruses, infection mechanisms and tissue types.  
47 The model is used to investigate how potential treatments influence disease progression.  
48 Simulation results suggest that drugs which interfere with virus replication (e.g.,  
49 remdesivir) yield substantially better infection outcomes when administered  
50 prophylactically even at very low doses than when used at high doses as treatment for  
51 an infection that has already begun.

52

## 53 **Introduction**

54           The current global pandemic of COVID-19, caused by the novel coronavirus  
55 Severe Acute Respiratory Syndrome Coronavirus 2 (SARS-CoV-2), has motivated the  
56 study of beta coronavirus diseases at multiple spatial and temporal computational  
57 modeling scales [1]. The time course, severity of symptoms and complications from  
58 SARS-CoV-2 infection are highly variable from patient to patient [2]. Mathematical  
59 modeling methods integrate the available host- and pathogen-level data on disease  
60 dynamics that are required to understand the complex biology of infection and immune  
61 response to optimize therapeutic interventions [3–5]. Mathematical models and computer  
62 simulations built on spatial and ODE frameworks have been extensively used to study in-  
63 host progression of viral infection [6], with a recent acceleration in the development of  
64 spatial COVID-19 viral infection models in response to the global pandemic [7,8].

65           Building multiscale models of acute primary viral infection requires integration of  
66 submodels of multiple biological components across scales (e.g., viral replication and  
67 internalization, immune system responses). Non-spatial, coupled ordinary differential  
68 equation (*ODE*) models can represent many aspects of pathogen-host interaction. In the  
69 context of viral infection dynamics, specialized ODE models can describe both the entire  
70 virus-host response at the tissue and organ levels and different stages of the viral  
71 replication cycle within cells, such as binding and internalization [9,10], viral genome  
72 replication and translation [11,12], assembly, packaging and release [13,14]. By fitting  
73 ODE models to clinical or experimental data, researchers have been able to estimate  
74 important parameters, such as the turnover rate of target cells, average lifetimes of viral

75 particles and infected cells and the rate of production of new viral particles by infected  
76 cells [15]. Other ODE models include pharmacokinetic models of drug availability [16].

77         The simplest non-spatial models assume that the distribution of the modelled  
78 quantities (e.g., cells, viruses, chemical species) are uniformly distributed in space and  
79 time [17]. This assumption might not be realistic in solid tissues, where viruses and host  
80 immune cells are not usually distributed homogeneously and infection propagates locally  
81 [15] or in situations where transport limits the dynamics (e.g. the migration of antigen  
82 presenting cells to lymph nodes, the transmission of virus between organs or the  
83 microdosimetry of a drug therapy). By averaging over spatio-temporal and individual cell  
84 variations, non-spatial models may not accurately reflect the effects of tissue  
85 heterogeneity and resulting viral infection dynamics [18]. Compartmental ODE models,  
86 like physiologically based pharmacokinetic models (PBPK) models or multi-compartment  
87 tissue infection models, maintain some of the simplicity of single-compartment ODE  
88 models, while recognizing the critical role transport can play in viral infection, immune  
89 response and treatment [19].

90         However, the spread of, and response to, some viruses is highly spatially localized,  
91 both *in vitro* and *in vivo* [20,21]. For example, COVID-19 often begins with infection  
92 localized to the nose and throat and then spreads to the lungs [22], with the specific  
93 location, size and distribution of lesions affecting clinical outcomes [23]. Spatial models  
94 have been increasingly used to address such issues [24], including partial differential  
95 equations [25,26] fluid-dynamic models [27] and agent-based models (ABM) [28]. ABMs  
96 represent host cells as spatially located, individual agents, and propagation of the  
97 infection emerges from individual interactions between agents. ABMs are also well suited

98 for extending existing models by modular integration of biological subcomponents, and  
99 their model parameters should be validated by experiment and studied through sensitivity  
100 analysis [17]. ABMs have been developed to account for infection dynamics in different  
101 biological compartments (such as the lung and lymph nodes [29,30]) and to model  
102 disease progression of HIV [15,25,31–33] and dissemination of influenza virus to the  
103 lower respiratory tract [18,34].

104 Spatial models often predict significantly different viral and immune dynamics,  
105 parameter estimates and therapy efficacies from their non-spatial counterparts.  
106 Stochastic effects arising from spatial conditions, such as local availability of target and  
107 immune cells, greatly influence establishment of infection and lead to different infection  
108 outcomes [15]. Non-spatial models generally produce viral load titers higher than spatial  
109 models, and the peaks of infection happen significantly earlier [17,18]. Homogenous  
110 recruitment of immune cells in spatial models matches ODE models when the number of  
111 infected is large, but not at the beginning of the infection when the number of infected  
112 cells is small [18]. These differences can lead to inaccurate estimates of important  
113 parameters such as viral infectivity [35], viral diffusion [17] and the basic reproductive  
114 ratio [35]. The basic reproductive ratio is clinically needed to determine therapeutic  
115 effectiveness [35]. Microdosimetry is another area where spatial modeling is important,  
116 since spatial variation in bioavailability can lead to low concentrations in some regions of  
117 an infected tissue, which can promote the evolution of resistant viral strains [15].

118 In this paper, we consider *primary* infection, that is, infection by a virus which the  
119 immune system has not previously encountered, so that there is no initial adaptive  
120 immune response. We focus on *acute* cases (cases with relatively rapid onset and short

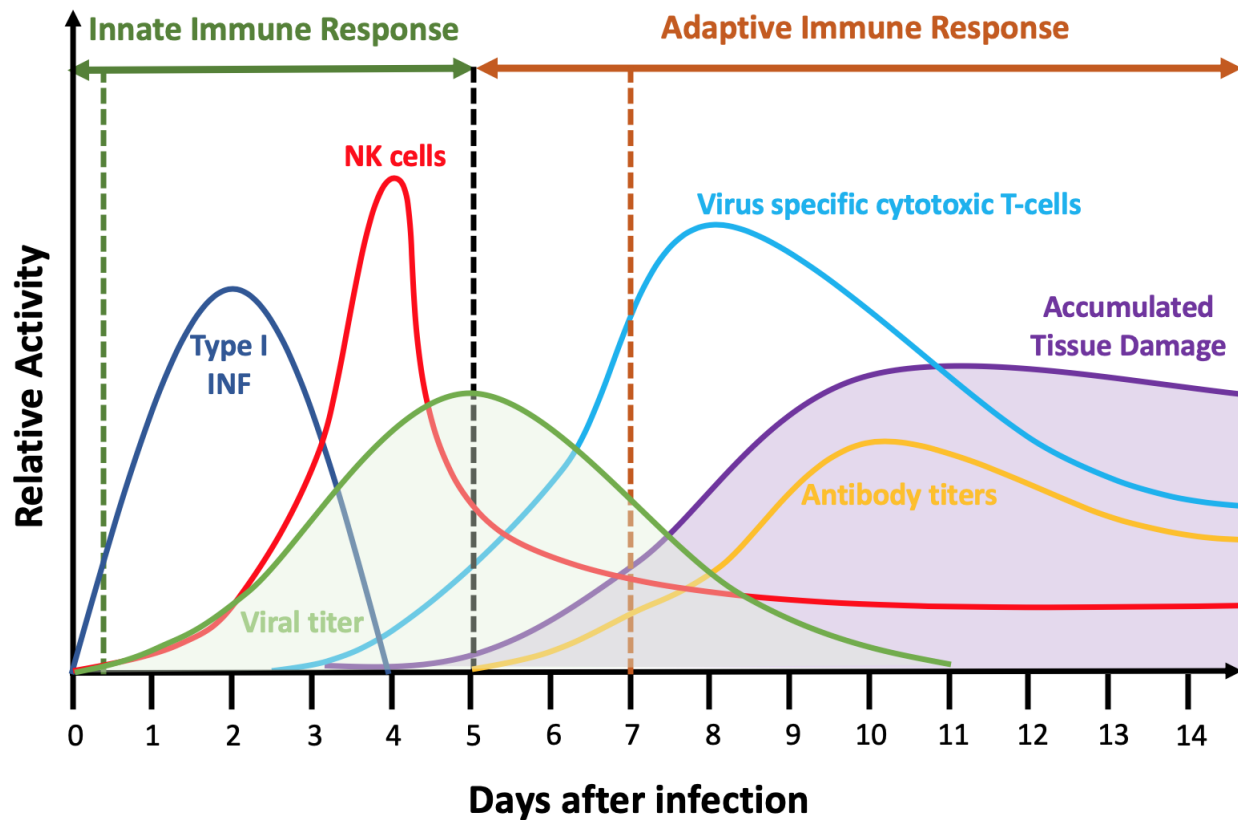
121 duration), in which a properly functioning immune system eventually eliminates the virus  
122 completely (*clearance*). Here we review relevant components of the immune system.  
123 Some of these components are included in this work and some are not modeled.  
124 However, by constructing a modular, extensible modeling framework and computational  
125 implementation, we enable the modeling of all these components.

126         While the details of infection vary by virus and patient [36], infection generally  
127 begins when a virus breaches the barrier of one or more tissues causing a limited number  
128 of target cells to be exposed and then internalize the virus (Fig 1). The virus begins to  
129 replicate within the initially infected target cells, but cells do not release any newly  
130 synthesized virus for a period of hours to days (the *eclipse* or *lag* phase of infection).  
131 Within hours, infected cells release proinflammatory cytokines and complement proteins  
132 as warning signals to neighboring cells [37,38]. Some of these cytokines, like Type 1  
133 interferons, can induce autocrine and paracrine anti-viral responses (e.g., inhibiting viral  
134 replication, viral entry or inducing cell death) [39]. Cytokines recruit circulating immune  
135 cells from the blood to the infected tissue and attract immune cells within the tissue by  
136 chemotaxis [40–42]. The early innate immune response activates a number of cell types  
137 including dendritic cells, macrophages, neutrophils, mast cells, basophils, eosinophils,  
138 leukocytes, and natural killer (*NK*) cells [43]. Many of these immune cells themselves  
139 release both pro- and anti-inflammatory signals. Immune signals also recruit circulating  
140 neutrophils in the blood and, later, activate cytotoxic innate immune cells like NK cells  
141 within the tissue, which kill infected cells through release of diffusible factors and contact-  
142 mediated interactions, respectively.

143           The temporal dynamics of the concentration of extracellular virus varies greatly  
144 among virus families, tissues and host species [44]. However, for many viruses, including  
145 influenza and coronaviruses, once infected cells begin to release virus, the amount of  
146 extracellular virus increases exponentially over a period of a few days, reaching a peak  
147 during an early phase of infection [45]. As the viral load increases, immune signaling  
148 increases rapidly (this increase is associated with the onset of fever and other symptoms)  
149 recruiting more circulating cells of the innate immune system to the infection site [46].

150           Immune signals from infected cells and innate immune cells help trigger the  
151 adaptive immune response. Macrophages and dendritic cells that have engulfed and  
152 degraded viral pathogens or fragments of dead infected cells (*i.e.*, phagocytosis) migrate  
153 over a period of days to nearby lymph nodes and serve as viral antigen presenting cells  
154 (*APCs*) to naive T-cells. Antigen presentation induces naive T-cell proliferation and  
155 differentiation into pathogen-specific memory and effector T-cells [47]. Effector T-cells  
156 migrate to the site of infection and induce apoptosis of infected cells by antigen  
157 recognition and contact killing. Both infected and uninfected cells in contact with dying  
158 cells can die through bystander-effect mechanisms. In acute infections, adaptive immune  
159 response leads to pathogen neutralization and clearance [48]. Viral loads usually  
160 decrease rapidly as adaptive immune cells like CD8+ T-cells enter the tissue and  
161 eliminate infected cells. Cells also begin to send out anti-inflammatory signals, shutting  
162 down the immune response as viral clearance proceeds. Antigen presentation within the  
163 immune system also induces activation of naive B-cell lymphocytes into antibody-  
164 producing memory B-cells and plasma cells, which leads to the production of antibodies.  
165 The adaptive immune response remembers its exposure to previous pathogens and

166 provides the body with pathogen-specific effector cells and antibodies which neutralize  
167 and clear them, providing long term immunity [49]. Tissue damage results from virus and  
168 cytokine-induced cell death (which is first noticeable after 2 or 3 days) and from killing of  
169 infected and uninfected cells by immune cells, which increases steadily until the end of  
170 viral clearance (7-10 days). Tissue recovery and healing start around the time of viral  
171 clearance and may last for several weeks.  
172



173

174 **Fig 1. Schematic of the innate and adaptive immune response during primary acute viral infection.**

175 Exposure to the virus occurs at time 0 and extracellular viral load begins to rise (shaded green curve). Initial innate  
176 immune responses include phagocytosis of virus by neutrophils and macrophages, Type I interferon-induced antiviral  
177 resistance (*IFN*) (dark blue) and killing of infected cells by Natural Killer (NK) cells and other cell types (red). The black  
178 vertical dashed line denotes the transition between innate and adaptive immune responses. The adaptive immune  
179 response is triggered both by cytokine signaling to the lymph nodes and the migration of antigen-presenting cells from



180 the tissue to the lymph nodes (not shown). In the later phases of infection, innate immune responses continue, but  
181 additional adaptive immune components come into play, including virus-specific cytotoxic T-cells (light blue) kill infected  
182 cells directly and also kill nearby cells through a variety of mechanisms. The orange vertical dashed line denotes the  
183 onset of the humoral adaptive immune response. B-cells produce virus-specific antibodies (orange line) which bind and  
184 inactivate virus directly and also allow its clearance and clearance of infected cells by other cell types. Tissue damage  
185 (shaded purple curve) accumulates due to cell death from direct responses to virus and from immune-cell killing by  
186 contact-mediated, diffusible factor-mediated and bystander-mediated mechanisms and eventually dissipates as cells  
187 proliferate to repair the damage (Adapted from [50,51]). The specific time course of all components varies among  
188 viruses, host tissues and host species, but the general sequence of events and immune response components are  
189 generally preserved.

190

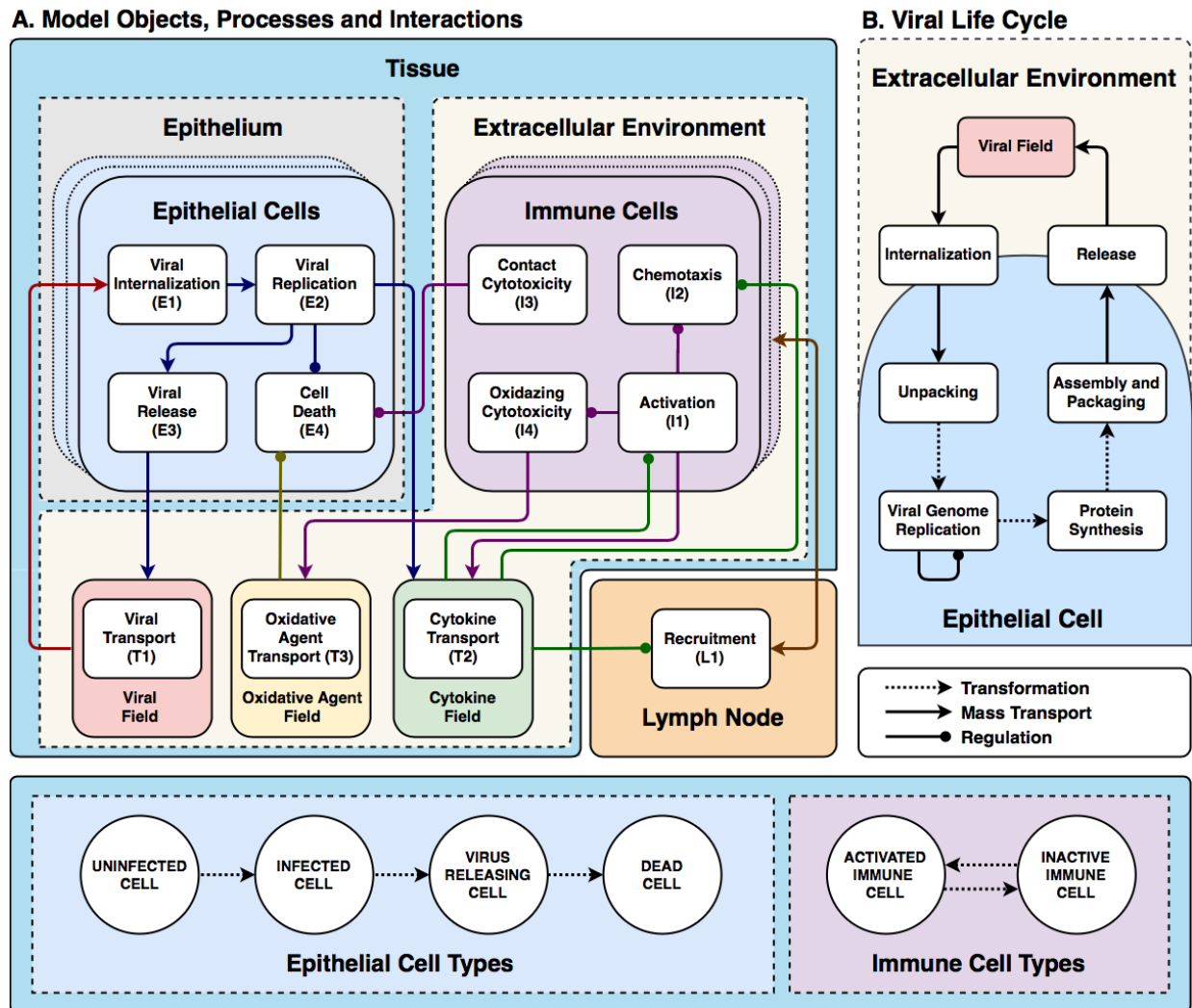
191 In this paper we develop a framework for the multiscale multicellular  
192 spatiotemporal simulation of the complex processes of infection and immune response in  
193 a small patch of epithelial tissue. The model provides a representation of the complex  
194 biology that reproduces key observed emergent behaviors of infection dynamics. We  
195 create representations of the main types of components and biological mechanisms  
196 associated with acute, primary viral infection and immune response, with a special  
197 emphasis on modularity of mathematical forms and computational implementation to  
198 support the development of more detailed models in future work (e.g., the creation of  
199 additional cell types, signals and detailed cell responses of various aspects of the immune  
200 response). We illustrate such an activity of development by integrating a detailed viral  
201 replication model for hepatitis C virus as an extension to the framework (see *Integration*  
202 *of an explicit RNA synthesis model allows the spatiotemporal modelling of hepatitis C*  
203 *virus infection*).

204 Our base model consists of three interconnected components (Fig 2A): an  
205 epithelium component, an extracellular environment component and a lymph node

206 component. The model represents the epithelium as a compact monolayer of initially  
207 identical immobile (which is appropriate for an epithelium) epithelial cells that it classifies  
208 by their current state of viral infection (*i.e.*, uninfected, infected, virus releasing, dead, Fig  
209 2C). These epithelial cells are initially identical in their number of viral receptors (though  
210 we show how to include heterogeneity in *Heterogeneous susceptibility inhibits spread of*  
211 *infection*). The cells internalize extracellular virus, modulate their number of surface  
212 receptors, replicate virus, release virus and die in response to virus production, and  
213 release an extracellular cytokine signal when infected. Our model omits interferon-  
214 induced antiviral resistance, which can be implemented as a model extension using  
215 mechanisms demonstrated in this work (*e.g.*, secretion of cytokine, modulation of  
216 internalization parameters, see *Developing a Model Extension in CompuCell3D*).

217 The model represents the extracellular environment as a space above the  
218 epithelium which provides the space in which immune cells are recruited and move, and  
219 into which cells release viruses and chemicals. We include a single type of immune cell  
220 that exhibits many key immune-cell behaviors associated with macrophage, neutrophil,  
221 NK cell and T-cell roles, including activation, chemotaxis, relaying and amplification of  
222 cytokine signals, contact killing, secretion of diffusible killing factors, and bystander killing,  
223 to represent the main types of immune-cell mediated cell killing, rather than any particular  
224 immune cell phenotype. We omit macrophages, neutrophils and their phagocytosis and  
225 signaling, which can be represented using simple extensions of the immune-cell type. We  
226 do not model contact interactions between immune cells (*e.g.*, by T-cells and APCs). We  
227 also do not model tissue recovery, though we demonstrate examples of adding tissue  
228 recovery models in *Model extensions*.

229



230

231 **Fig 2. Full model schematic.**

232 (A) Model objects, processes and interactions: Conceptual model of an epithelial tissue and lymph node. Schematic  
 233 representation of the model objects, processes and interactions. Epithelial and immune cells refer to the two main  
 234 classes of cells. Interactions occur within an extracellular environment, and a compartmental model of a lymph node  
 235 controls immune-cell recruitment to the tissue. Together the epithelial-cell, extracellular-environment and immune-cell  
 236 components represent the epithelial tissue. Each model object has associated processes that dictate its states and  
 237 behaviors. Epithelial-cell processes include viral internalization (E1), viral replication (E2), viral release (E3) and cell  
 238 death (E4). Immune cell processes include activation (I1), chemotaxis (I2), contact cytotoxicity (I3) and oxidative  
 239 cytotoxicity (I4). *Activated* immune cells participate in oxidative cytotoxicity (I4) and secrete oxidative agents into the

240 oxidizing-agent field (**T3**). Activated cells become inactive after 1 hour. The virus field (**T1**), cytokine field (**T2**) and  
241 oxidizing-agent field (**T3**) describe spatially-varying densities of extracellular components. Field processes describe  
242 diffusive transport and clearance of material in the extracellular environment and activated transport to the lymph nodes.  
243 The lymph node is a single-compartment model whose pro- or anti-inflammatory state specifies the recruitment or  
244 removal rate (**L1**) of immune cells in the epithelial tissue. The transport of cytokines to the lymph node promotes its  
245 proinflammatory state. (B) Viral Life Cycle: Interactions in the viral internalisation, replication and release models.  
246 Schematic representation of inputs, outputs and interactions between stages of the viral replication model. Extracellular  
247 viral particles (represented as continuous fields) are internalized by the viral internalization model and initiate the viral  
248 replication model. The main stages of the viral replication model are: unpacking, viral genome replication, protein  
249 synthesis and viral assembly and packaging. The output of the viral replication model passes to the viral release model,  
250 which transfers newly assembled viral particles from the cells into the extracellular environment. (C) Cell types and  
251 transitions. Epithelial cells are of type *uninfected* if they have not yet internalized any virus (**E1**). They are of type  
252 *infected* if they have internalized virus, but are not releasing virus into the virus field (viral release **E3** is inactive). They  
253 are of type *virus releasing* if they are releasing virus into the extracellular virus field (*i.e.*, viral release **E3** is activated).  
254 Immune cells are initially *inactive* and do not participate in the oxidative cytotoxicity (**I4**) or chemotax towards higher  
255 concentrations of the cytokine field (**I2**). They become *activated* when they experience activation (**I1**). In all panels,  
256 dashed arrows with barbed heads represent transformations, solid arrows with barbed heads represent transport and  
257 solid arrows with lollipop heads represent regulation.

258  
259 We simulate extracellular-virus particle density as a continuum field and particle  
260 transport and clearance as continuous diffusion and decay. We approximate the discrete  
261 process of a cell's internalization of a virus particle by a stochastic virus internalization  
262 event (**E1**) determined by time elapsed, the local concentration of the virus field, and the  
263 number of available cell-surface receptors on the cell. We simplify the complexity of viral  
264 replication into four steps: unpacking, viral genome replication, protein synthesis and  
265 packaging/assembly (**E2**, Fig 2B) [7,52–54]. The subcellular kinetics of viral replication  
266 determine the rate of release of new virus particles into the extracellular environment (**E3**).  
267 To represent the combined effect of the many types of virus-induced cell death, each

268 infected epithelial cell has a probability of dying that depends on the number of assembled  
269 viral particles inside the cell per unit time (**E4**).

270 We simplify the complex biochemistry of the many molecular signals active in  
271 epithelial tissues, which include chemokines, interferons and viral fragments, into a single  
272 generic extracellular cytokine field that acts both as a tissue-local and systemic pro-  
273 inflammatory signal. Infected epithelial cells and immune cells both secrete cytokine (**T2**).  
274 The cytokine field produces local immune effects such as activation (**I1**) and chemotaxis  
275 (**I2**) of immune cells. Activated immune cells can revert back to inactive immune cells  
276 when the cytokine signal ceases. The cytokine field also recruits immune cells to the  
277 tissue through long-distance signaling via the lymphatic system (**L1**). We model  
278 recruitment of immune cells to the simulation domain using an ordinary differential  
279 equation for the *immune signal* ( $S$ ), which represents the balance between pro- and anti-  
280 inflammatory signaling and the delay due to antigen-presenting cell transport from the  
281 tissue through the lymphatic system to the lymph node and due to the time required for  
282 T-cell amplification. In the absence of infection, the lymph node maintains a small resident  
283 immune cell population in the tissue. Immune cells can cause epithelial cell death (**E4**) by  
284 three mechanisms: 1) contact cytotoxicity; 2) the bystander effect; and 3) through the  
285 release of an oxidative agent. Immune cells kill infected epithelial cells by contact  
286 cytotoxicity, in which case neighboring uninfected, infected and virus-releasing epithelial  
287 cells can also die through a bystander effect (**I3**). In regions of the tissue with high cytokine  
288 levels, immune cells secrete a diffusive oxidative agent to the environment (**T3**) that kills  
289 uninfected, infected and virus-releasing epithelial cells (**I4**).

290

## 291 **Results**

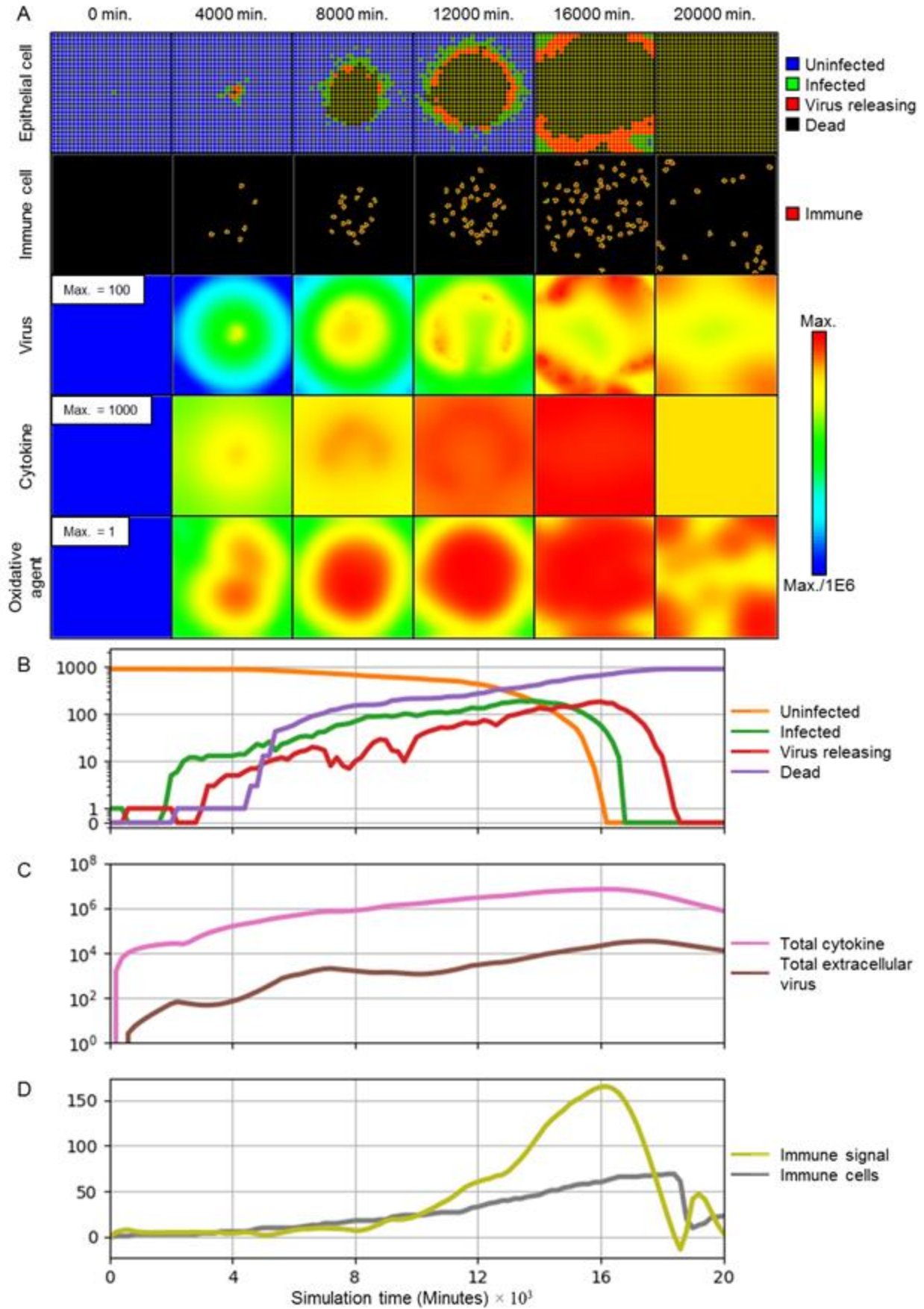
292 We begin by presenting our base multicellular model of viral infection in an  
293 epithelial tissue, along with a simulation for a baseline set of parameters and basic  
294 analyses. We then explore the simulation's dependence on critical parameters that are  
295 important to the dynamics of acute primary viral infection in airway epithelial cells. All  
296 simulations and spatial, population and system-level metrics presented in this section  
297 follow the specifications in *Simulation Specifications*. We performed simulations using the  
298 open-source modeling environment CompuCell3D [55]. *Downloading and running the*  
299 *simulation* provides instructions on how to run these simulations.

300 We initialize the simulations with periodic boundary conditions parallel to the plane  
301 of the sheet and Neumann boundary conditions perpendicular to the plane of the sheet.  
302 Initially, the extracellular environment does not contain any extracellular virus, cytokines,  
303 oxidative agents or immune cells. We introduce infection by creating a single infected  
304 epithelial cell at the center of the epithelial sheet, comparably to (but less than) initial  
305 conditions of similar works that model discrete cellular distributions [18,31] . To illustrate  
306 the full range of dynamics of viral infection in the presence of an immune response, we  
307 established a baseline set of parameters (Table 1) for which the immune response is  
308 strong enough to slow the spread of the infection, but insufficient to prevent widespread  
309 infection and death of all epithelial cells (Fig 3). While we have adjusted the parameters  
310 for the viral replication model to agree with reported time scales for SARS-CoV-2  
311 replication *in vitro* [56], and we have selected parameter values in physiologically  
312 reasonable ranges, we have not attempted to match other model parameters to a specific  
313 tissue, virus or host species. Furthermore, this baseline parameter set is not unique with

314 respect to its purpose, in that many sets of parameters can generate appreciable but  
315 insufficient inhibition of spread of infection (see *Figs S17-S22*). Rather, as is shown in  
316 subsequent sections, this parameter set presents emergent dynamics of a theoretical  
317 virus and host immune response near, but not in, a regime of successful prevention of  
318 widespread infection, which is critical to showing the effects of underlying mechanisms  
319 on emergent dynamics and resulting outcomes.

320







322 **Fig 3. Simulation of the progression of infection in a patch of epithelial tissue of size 360  $\mu\text{m}$  x 360  $\mu\text{m}$  starting**  
323 **from a single infected cell for a representative simulation using the baseline parameters given in Table 1.**

324 (A) Snapshots of spatial configuration vs time, showing progression of a simulated infection. Columns, left to right: 0  
325 minutes (time of initial infection), 4000 minutes (67 hours, 2  $\frac{3}{4}$  days) after infection, 8000 minutes (133 hours, 5  $\frac{1}{2}$   
326 days), 12000 minutes (200 hours, 8  $\frac{1}{3}$  days), 16000 minutes (267 hours, 11 days), and 20000 (333 hours, 14 days)  
327 minutes. First row: epithelial-cell layer composed of uninfected (blue), infected (green), virus-releasing (red) and dead  
328 epithelial cells (black). Second row: position of immune cells in the extracellular environment layer. Third row:  
329 concentration of extracellular virus field. Fourth row: concentration of extracellular cytokine field. Fifth row: concentration  
330 of extracellular oxidative agent field. Fields are shaded on a logarithmic scale: red corresponds to the chosen maximum  
331 value specified in the first panel and blue corresponds to six orders of magnitude lower than the maximum value; colors  
332 saturate for values outside this range. (B-D) Simulation time series. (B) Number of uninfected (orange), infected (green),  
333 virus-releasing (red) and dead (purple) epithelial cells vs time on a logarithmic scale (0 values are overlaid at a non-  
334 logarithmic tick for clarity). (C) Total extracellular cytokine (magenta) and total extracellular virus (brown) vs time on a  
335 logarithmic scale. (D) Value of the immune recruitment signal  $S$  (yellow) and number of immune cells (grey) vs time on  
336 a linear scale. Simulations use periodic boundary conditions in the plane of the epithelial sheet, and Neumann  
337 conditions [57] normal to the epithelial sheet.

338

339 The infected cell immediately starts releasing cytokines into the extracellular  
340 environment. After an incubation period ( $\sim 150$  minutes, 2  $\frac{1}{2}$  hours), the first infected  
341 epithelial cell (green) transitions from infected to virus releasing (red), and starts releasing  
342 viruses into the extracellular environment. Initial release of extracellular virus causes  
343 additional epithelial cells to become infected. Release of cytokines leads to delayed  
344 addition of immune cells to the simulation domain (Fig 3D). By 4000 minutes (67 hours,  
345 2  $\frac{3}{4}$  days), the number of infected cells increases 10-fold and the epithelial cells start  
346 undergoing virally-induced death as the infection spreads radially outward from the initial  
347 site. The increase in the number of infected cells and the local cytokine concentration is  
348 accompanied by a similar increase in the local immune cell population. By 8000 minutes

349 (133 hours, 5 ½ days), the number of dead epithelial cells around the initial infection site  
350 increases sharply. Following this phase of rapid cell death, the number of infected, virus-  
351 releasing and dead epithelial cells continues to increase exponentially but at a slower  
352 rate. This transition results in the formation of an annular region of infected cells spreading  
353 radially outwards from the initial infection site (Fig 3A), analogous to the Fisher equation  
354 for deterministic front propagation [58]. Total extracellular virus and cytokine continue to  
355 increase exponentially. The increase in cytokine results in continued recruitment of  
356 additional immune cells. By 16000 minutes (267 hours, 11 days), the number of  
357 uninfected epithelial cells reaches zero and the number of infected and virus-releasing  
358 cells peaks. Despite the declining number of infected and virus-releasing epithelial cells,  
359 the delayed immune response continues to add immune cells to the tissue. After about  
360 16000 minutes (267 hours, 11 days), the extracellular virus and the amount of cytokine  
361 decrease exponentially as the remaining virus-releasing epithelial cells die. By 20000  
362 minutes (333 hours, 14 days), all epithelial cells die and many immune cells leave the  
363 tissue.

364

### 365 **Classification of spatiotemporal infection dynamics**

366 The rate at which infection propagates and the strength (speed and amplitude) of  
367 the immune response depend on multiple model parameters. Interplay between these  
368 rates leads to a wide spectrum of qualitatively-distinct spatiotemporal dynamics. The  
369 virus-receptor binding affinity  $k_{on}$  and the immune response delay coefficient  $\beta_{delay}$  are  
370 critical parameters affecting the rate of infection of epithelial cells and the strength of the

371 immune response, respectively. Larger  $k_{on}$  corresponds to a higher rate of infection  
372 propagation (increasing  $k_{on}$  increases the rate of internalization of extracellular viral  
373 particles into epithelial cells, see Equation (3) in *Models and methods*). Larger  $\beta_{delay}$   
374 corresponds to weaker immune response (decreasing  $\beta_{delay}$  increases the strength of  
375 immune-cell recruitment, see Equations (12)-(14) in *Models and methods*).

376 Varying these two parameters around the baseline simulation values yields six  
377 patterns of spatiotemporal infection dynamics, ranging from unopposed infection to  
378 clearance (Fig 4). We defined these classes based on the transient dynamics and the  
379 final state of the simulation at 20000 minutes (333 hours, 14 days). We terminated the  
380 simulations at 20000 minutes (333 hours, 14 days) because we assume that, in real  
381 tissues, additional adaptive immune responses at this time generally lead to rapid viral  
382 clearance. As a result, any epithelial cells uninfected at the end of the simulation would  
383 likely remain uninfected if we included these additional immune mechanisms. We define  
384 the six patterns (*classes*) of infection dynamics as follows:

385

386 **No immune response:** a limiting case (corresponding to *in vitro* and organoid  
387 culture experiments on viral infection, which lack immune cells) that serves as a  
388 reference simulation showing the spread of unopposed infection. When the cellular  
389 immune response is absent, an infection front travels across the epithelium until  
390 all epithelial cells have died due to intracellular virus (Figs 4A and S1).

391 **Widespread infection:** when the immune response is weak (large  $\beta_{delay}$ ) or the  
392 rate of infection propagation is large (large  $k_{on}$ ), the immune cells kill enough  
393 infected epithelial cells to reduce both the concentration of extracellular virus and

394 the propagation of the infection front. However, at the end of the simulation no  
395 uninfected epithelial cells survive (Figs 3 and 4B).

396 **Slowed infection:** for moderate immune response (moderate  $\beta_{delay}$ ) and a  
397 moderate rate of infection propagation (moderate  $k_{on}$ ), both uninfected and  
398 infected epithelial cells and some extracellular virus remain at the end of the  
399 simulation (Fig 4C). These cases are functionally distinct from widespread  
400 infection, since even a single remaining uninfected epithelial cell could initiate  
401 tissue regeneration. In most cases of slowed infection, the numbers of infected  
402 cells and the extracellular virus continue to increase. A special case of slowed  
403 infection occurs when oscillations in the amount of virus (Fig S2A).

404 **Containment:** for strong immune response (small  $\beta_{delay}$ ) and low to moderate rate  
405 of infection propagation (moderate  $k_{on}$ ), a few infected and virus-releasing cells  
406 are present for most of the simulation. However, the immune cells eventually kill  
407 all infected and virus-releasing epithelial cells. At the end of the simulation, no  
408 infected or virus releasing cells remain, while uninfected cells survive and some  
409 extracellular virus remains in the extracellular environment (Fig 4D).

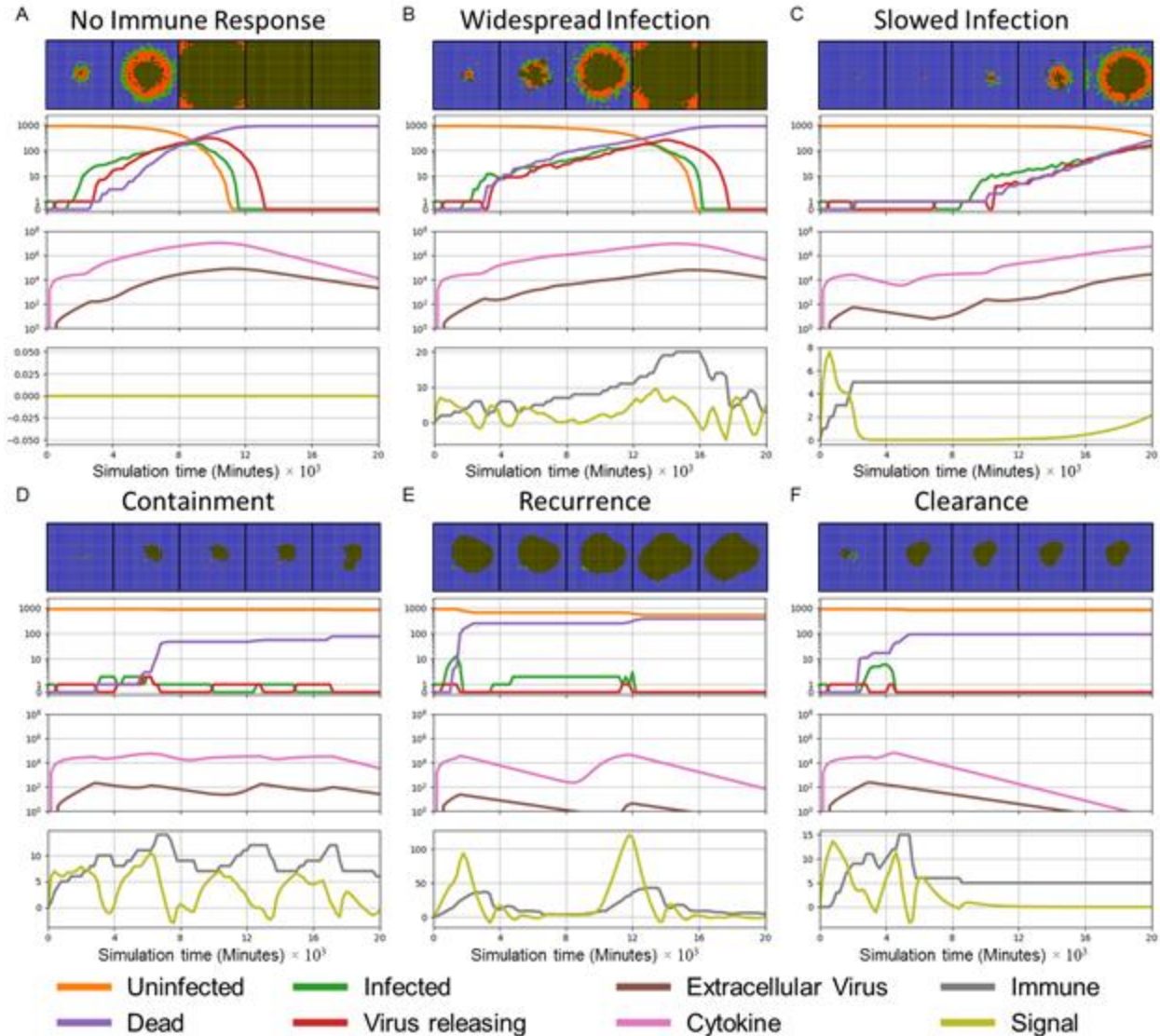
410 **Recurrence:** for strong immune response (small  $\beta_{delay}$ ) and a fast infection  
411 propagation (large  $k_{on}$ ), relatively few epithelial cells become infected early in the  
412 simulation. All infected and virus-releasing epithelial cells die. However, the  
413 remaining extracellular virus infects additional epithelial cells later on, restarting  
414 the spread of infection (Fig 4E).

415 **Clearance:** for strong immune response (small  $\beta_{delay}$ ) and a slow infection  
416 propagation (small  $k_{on}$ ), the number of infected and virus-releasing epithelial cells

417 goes to zero without recurrence and the extracellular virus drops below a threshold  
418 (of 1/900 per cell in our analysis), rendering the frequency of recurrence negligible  
419 (Fig 4F). A special case of clearance (**Failure to infect**) occurs when the initially  
420 infected epithelial cells fail to infect any other epithelial cells (Fig S2B).

421  
422 To quantitatively characterize simulation results, we measured the number of  
423 uninfected, infected, virus-releasing and dead epithelial cells, the total number of immune  
424 cells, the number of activated immune cells, the total amount of extracellular virus  
425 (integral over the virus field), the total diffusive cytokine (integral over cytokine field), the  
426 maximum total extracellular virus (over all simulation time) and the maximum total  
427 diffusive cytokine (over all simulation time). Fig 4 shows these quantitative metrics,  
428 together with a series of spatial configurations for all model components, corresponding  
429 to each pattern of infection dynamics.

430



431

432 **Fig 4. Patterns (classes) of spatiotemporal infection dynamics.**

433 First row: snapshots of spatial configurations of the epithelial cells. Color coded: uninfected (blue), infected (green),

434 virus releasing (red), dead (black). Times from left to right 4000 minutes (67 hours, 2  $\frac{3}{4}$  days), 8000 minutes (133

435 hours, 5  $\frac{1}{2}$  days), 12000 minutes (200 hours, 8  $\frac{1}{3}$  days), 16000 (267 hours, 11 days) and 20000 minutes (333 hours,

436 14 days). The right border of each snapshot aligns with the corresponding time in the time series. Second row: number

437 of uninfected (orange), infected (green), virus-releasing (red) and dead (purple) epithelial cells vs time on a logarithmic

438 scale (with 0 included for clarity). Third row: total extracellular cytokine (magenta) and total extracellular virus (brown)

439 vs time on a logarithmic scale. Fourth row: value of the immune recruitment signal  $S$  (yellow) and number of immune

440 cells (grey) vs time on a linear scale. (A) No immune response: infection propagates unopposed until all epithelial cells

441 have died from intracellular virus. (B) Widespread infection: weak immune response slows propagation of the infection,

442 but no uninfected cells survive at the end of the simulation. (C) Slowed infection: uninfected and infected epithelial cells  
443 coexist at the end of the simulation. (D) Containment of infection: no infected or virus-releasing epithelial cells remain,  
444 uninfected cells survive and virus remains in the extracellular environment at the end of the simulation. (E) Recurrence:  
445 the number of infected and virus releasing epithelial cells goes to zero, but persistent extracellular virus infects new  
446 epithelial cells later on. (F) Clearance: the number of infected and virus-releasing epithelial cells goes to zero and the  
447 level of extracellular virus is negligible at the end of the simulation. The model in (A) omits the immune response  
448 (components **L1**, **I1-I4**). All parameter values are as in Table 1 and Fig 3 except for  $k_{on}$  and  $\beta_{delay}$  (Table S1).

449  
450 In the absence of an immune response, spread of the infection follows the diffusion  
451 of extracellular virus, resulting in concentric rings of different types of epithelial cells (see  
452 Fig 4A top row for epithelial cell types, Fig S1B shows the extracellular virus field). The  
453 viral propagation front, where uninfected epithelial cells transition to infected epithelial  
454 cells, moves radially outwards from the initial site of infection. Due to the stochastic  
455 internalization events, the front's outer contour is diffuse, with scattered infected epithelial  
456 cells ahead of the front, followed by a dense rim of infected and virus-releasing epithelial  
457 cells and a core of dead epithelial cells at the center. Similar waves, with a slower speed,  
458 are seen in the other cases where infection has occurred (Fig 4B and C top row).

459  
460 **Stronger immune response and lower rates of virus internalization promote**  
461 **containment of infection**

462 To explore the effects of the rate of virus internalization and the strength of the  
463 immune response, we performed a multidimensional parameter sweep of the virus-  
464 receptor association affinity  $k_{on}$  and immune response delay coefficient  $\beta_{delay}$ . Variations  
465 in virus receptor association affinity represent factors that affect the binding affinity of  
466 cellular viral receptors (e.g., ACE2 and TMPRSS-2 in the case of SARS-CoV-2) with a

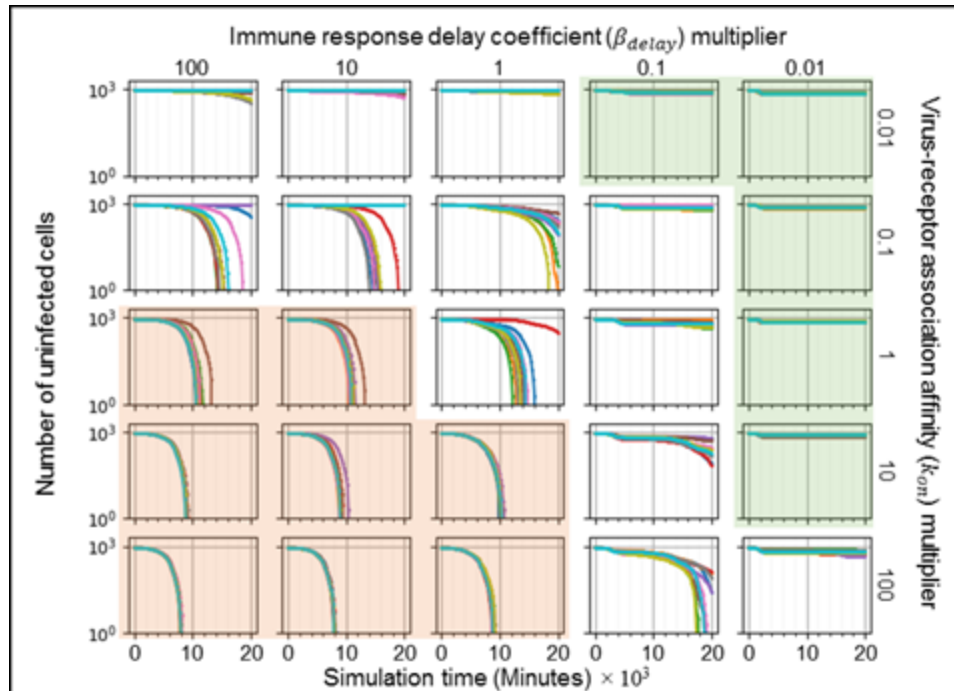


467 virus (e.g., mutations in viral coat protein or drugs to block viral entry). Variations in  
468 immune response delay coefficient represent factors that affect the strength of the  
469 systemic immune response (e.g., anti-inflammatory corticosteroids, IL-7 treatment or age,  
470 since older individuals tend to have slower adaptive immune responses)[36].

471 We ran ten simulation replicas for each parameter set, increasing and decreasing  
472 the baseline parameter values 10-fold and 100-fold (Figs 5-7). For each simulation  
473 replica, we examined the number of uninfected epithelial cells (Fig 5), the number of  
474 infected epithelial cells (Fig 6), the total extracellular virus (Fig 7), the number of dead  
475 epithelial cells (Fig S3), the number of virus-releasing cells (Fig S4) and the number of  
476 immune cells (Fig S5). We identified regions of the parameter space where all ten  
477 simulation replicas resulted in either containment/clearance (green-shaded subplots) or  
478 widespread infection (orange-shaded subplots). In the intermediate regions (unshaded  
479 subplots) different replicas for the same set of parameters exhibited other (and sometimes  
480 multiple) classes of dynamics.

481





482

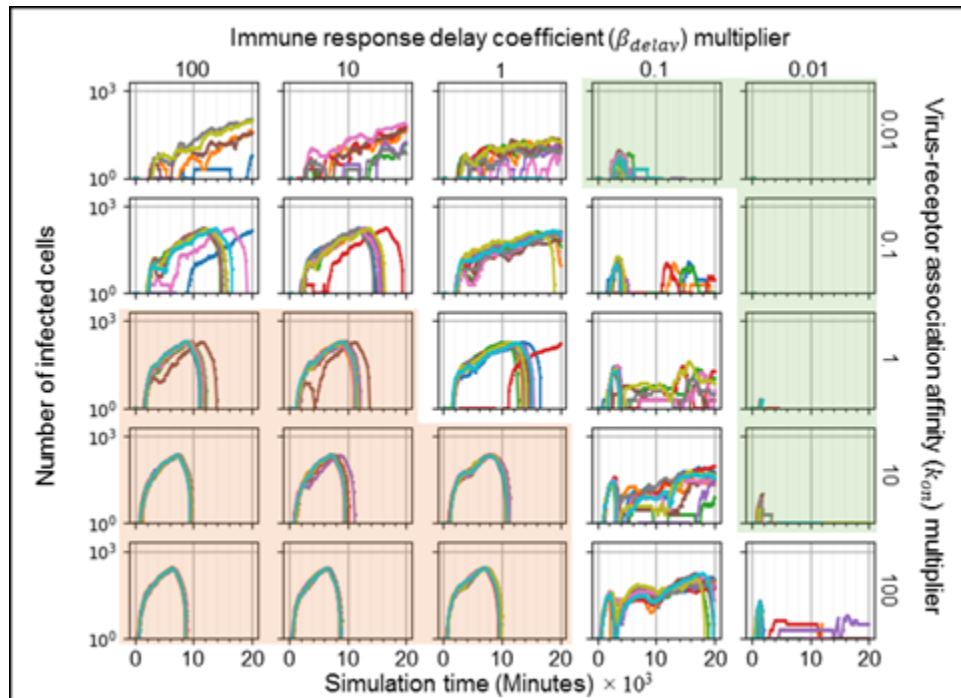
483 **Fig 5. Sensitivity analysis of the number of uninfected epithelial cells vs time for variations in virus-receptor**  
484 **association affinity  $k_{on}$  and immune response delay coefficient  $\beta_{delay}$ , showing regions with distinct infection**  
485 **dynamics.**

486 Logarithmic pairwise parameter sweep of the virus-receptor association affinity  $k_{on}$  and the immune response delay  
487  $\beta_{delay}$  ( $\times 0.01, \times 0.1, \times 1, \times 10, \times 100$ ) around their baseline values, with ten simulation replicas per parameter set (all  
488 other parameters have their baseline values as given in Table 1). The number of uninfected epithelial cells for each  
489 simulation replica for each parameter set, plotted on a logarithmic scale, vs time displayed in minutes. See Fig 4 for  
490 the definitions of the classes of infection dynamics.

491

492 For large  $k_{on}$  and large  $\beta_{delay}$  (Figs 5-7, orange-shaded regions), all simulation  
493 replicas result in widespread infection and variability between simulation replicas is small.  
494 In this region, the initial release of virus into the extracellular environment results in a  
495 rapid increase in the number of infected and virus releasing epithelial cells early during  
496 the simulation, between 0 and 2000 minutes (0 to 33 hours, 0 to 1  $\frac{1}{2}$  days) (Figs 6 and  
497 S4). Between 5000 and 20000 minutes (83 to 333 hours, 3  $\frac{1}{2}$  to 14 days), the number of

498 uninfected epithelial cells rapidly decays to zero. As in all simulation replicas with a large  
499  $\beta_{delay}$ , the immune recruitment signal (Fig S6) is less responsive to the cytokine signal  
500 produced by infected and virus-releasing epithelial cells and no significant recruitment of  
501 immune cells occurs throughout the simulations (Fig S5). The number of virus-releasing  
502 epithelial cells peaks around 7500 minutes (125 hours, 5 days), the level of extracellular  
503 virus peaks around 9000 minutes (150 hours, 6 ¼ days) and the number of dead epithelial  
504 cells peaks around 10000 minutes (167 hours, 7 days, Fig S3). With no remaining  
505 uninfected epithelial cells to infect, all remaining infected epithelial cells become virus-  
506 releasing epithelial cells, which then die, causing the total amount of extracellular virus to  
507 decrease.  
508



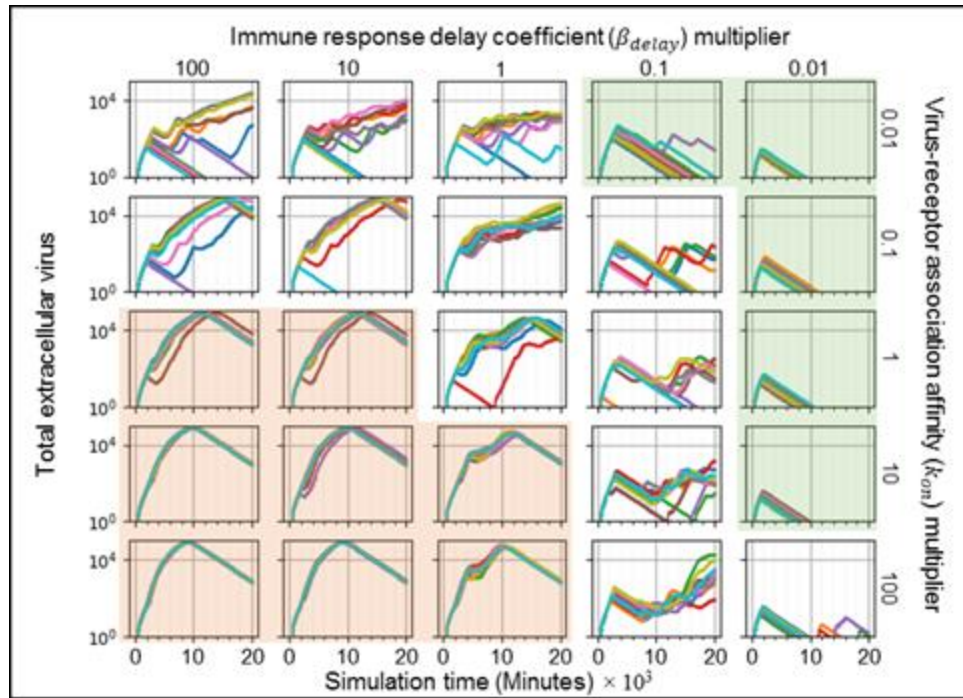
509  
510 **Fig 6. Sensitivity analysis of the number of infected epithelial cells vs time for variations in virus-receptor**  
511 **association affinity  $k_{on}$  and immune response delay coefficient  $\beta_{delay}$ , showing regions with distinct infection**  
512 **dynamics.**

513 Same parameter sweep as Fig 5. The number of infected epithelial cells for each simulation replica for each parameter  
514 set, plotted on a logarithmic scale, vs time displayed in minutes. See Fig 4 for the definitions of the classes of infection  
515 dynamics.

516

517 For small  $k_{on}$  and small  $\beta_{delay}$  (Figs 5-7, green-shaded subplots), all simulation  
518 replicas result in either clearance or containment and variability between simulation  
519 replicas is small. Initial release of virus to the extracellular environment results in a small  
520 change in the number of uninfected and infected epithelial cells. As in all simulation  
521 replicas with a small  $\beta_{delay}$ , the immune recruitment signal (Fig S6) is very sensitive to  
522 the cytokine produced by virus-releasing epithelial cells, resulting in rapid recruitment of  
523 immune cells and an early first peak in the population of immune cells around 2000  
524 minutes (33 hours, 1  $\frac{1}{3}$  days, Fig S5). In these simulations, the increase in the number of  
525 immune cells is followed by a rapid increase in the number of dead epithelial cells (Fig  
526 S3). The number of immune cells and the number of dead epithelial cells peak around  
527 the same time (2000 minutes, 33 hours, 1  $\frac{1}{3}$  days), after which the number of immune  
528 cells decreases. With no remaining virus-releasing epithelial cells, the total extracellular  
529 virus decays until the infection is cleared. Increasing  $\beta_{delay}$  primarily increases the time  
530 when all infected epithelial cells have died.

531



532

533 **Fig 7. Sensitivity analysis of the total amount of extracellular virus vs time for variations in virus-receptor**  
534 **association affinity  $k_{on}$  and immune response delay coefficient  $\beta_{delay}$ , showing regions with distinct infection**  
535 **dynamics.**

536 Same parameter sweep as Fig 5. The total amount of extracellular virus for each simulation replica for each parameter  
537 set, plotted on a logarithmic scale, vs time displayed in minutes. See Fig 4 for the definitions of the classes of infection  
538 dynamics.

539

540 For moderate to high  $k_{on}$  and moderate to low  $\beta_{delay}$  (right unshaded subplots in  
541 Figs 5-7), the rate of new infection nearly balances the rate of elimination of infected and  
542 virus-releasing epithelial cells, resulting in replicas showing clearance, contaminant,  
543 recurrence and slowed infection for the same parameter values, with very few cases of  
544 widespread infection. The initial release of virus into the extracellular environment by the  
545 first virus-releasing epithelial cell infects a moderate number of uninfected epithelial cells.  
546 The resulting cytokine secretion elicits a moderate to high response of the immune  
547 recruitment signal (Fig S6) and number of immune cells (Fig S5). The early recruitment

548 of immune cells leads to many epithelial cells dying before 4000 minutes (66 hours,  $2\frac{2}{3}$   
549 days) (Fig S3). For a high probability of virus internalization (high  $k_{on}$ ), even low amounts  
550 of extracellular virus are sufficient to cause recurrence. For moderate to low  $k_{on}$  and  
551 moderate to high  $\beta_{delay}$  (upper left unshaded subplots in Figs 5-7), rate of new infection  
552 of epithelial cells is slightly faster than the immune system's response, resulting in a  
553 combination of widespread infection, slowed infection and containment, and a few cases  
554 of clearance. The immune system is only moderately responsive to the cytokine signal,  
555 resulting in a slow to moderate increase in the immune recruitment signal (Fig S6) and in  
556 the number of immune cells (Fig S5). Cases of clearance and containment occur for a  
557 smaller final number of dead epithelial cells (Fig S3) compared to previously discussed  
558 cases.

559

560 **Even moderate inhibition of genomic replication by antiviral therapies significantly**  
561 **reduces the spread of infection, but only when initiated soon after infection**

562 Optimal therapeutic use of antiviral drugs requires considering the relationship  
563 between molecular *efficacy* (how effectively the drug blocks a particular aspect of the viral  
564 life cycle at saturation concentration), *potency of therapy* (the effect of the drug at a  
565 molecular level at a given dose) and clinical *effectiveness* (how well the drug reduces the  
566 severity or duration of the infection), as well as the tradeoff between side effects and  
567 bioavailability. One drug might have moderate efficacy but have few side effects. Another  
568 drug might have high efficacy, but have severe side effects at high doses that limit the  
569 maximum tolerated dose or use of even moderate doses in prophylaxis. A drug might  
570 also have a combination of beneficial and adverse effects (e.g., it might reduce viral

571 replication early in infection, but also be immunosuppressive) [13,37]. Antiviral drugs like  
572 Tamiflu retain their ability to block aspects of the viral life cycle (efficacy), but become  
573 much less clinically effective as the time before treatment increases: (in adults Tamiflu is  
574 most effective when given within 48 hours after exposure and thus is often used  
575 prophylactically) [38].

576 In this section we use our model to show the trade-offs between time-of-use and  
577 potency of a drug that targets viral genome replication in a host cell. Several antiviral  
578 medications for RNA viruses reduce the net viral replication rate by inhibiting synthesis of  
579 viral RNA by the viral RNA polymerase. We focus on RNA-synthesis blockers in this paper  
580 because viral genome synthesis exponentially increases the production rate of viruses  
581 per cell, while the other stages of viral replication have linear amplification effects (see  
582 Equations (6)-(9) in *Models and methods*).

583 To simulate the effects of treatment that targets RNA synthesis using different drug  
584 efficacies and times of administration, we generated a series of simulations in which we  
585 reduced  $r_{max}$ , the replication rate of genomic material in the viral replication model  
586 (Equation (7) in *Models and methods*), by different amounts and at different times in the  
587 simulation. The “viral replication multiplier” represents the potency of the treatment, the  
588 factor by which  $r_{max}$  is reduced (either a low dose with high efficacy, or a high dose with  
589 a less efficacy). The “time delay of application” is the simulation time at which  $r_{max}$  is  
590 reduced, which corresponds to the time after infection at which the treatment is  
591 administered. To characterize therapeutic effectiveness, we distinguished three classes  
592 of simulation outcomes:

593

594           **Positive outcomes:** effective treatment, where at least 50% of the epithelial cells  
595 remain uninfected at the end of the simulation (green-shaded subplots).

596           **Negative outcomes:** ineffective treatment, where less than 10% of the epithelial  
597 cells remain uninfected at the end of the simulation (orange-shaded subplots).

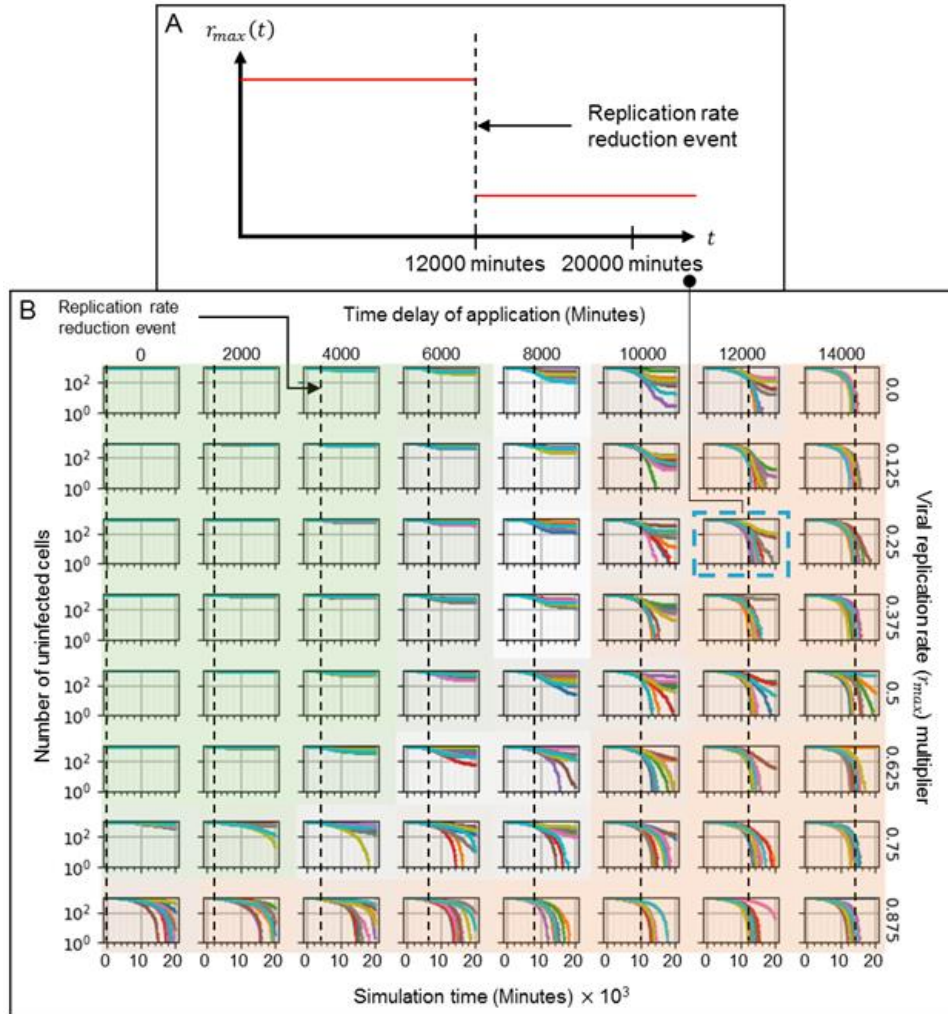
598           **Intermediate outcomes:** partially effective treatment, where between 10-50% of  
599 the epithelial cells remain uninfected at the end of the simulation (unshaded or  
600 intermediate-shaded subplots).

601

602           To characterize how the potency and time of initiation of treatment affect the  
603 dynamics of the simulation and treatment effectiveness, we examined the time courses  
604 of the number of uninfected epithelial cells (Fig 8), virus-releasing epithelial cells (Fig 9),  
605 the total amount of extracellular virus (Fig 10), the number of dead epithelial cells (Fig S7)  
606 and the number of immune cells (Fig S9). Intensity of green indicates the percent of  
607 simulation replicas that produced positive outcomes for a given set of parameters.  
608 Intensity of orange indicates the percent of simulation replicas that produced negative  
609 outcomes.

610





611  
 612 **Fig 8. Number of uninfected cells vs time in simulations of a hypothetical drug treatment reducing the viral**  
 613 **genome (e.g. RNA for SARS-CoV-2) replication rate ( $r_{max}$ ) as a function of treatment potency and of**  
 614 **initiation of treatment.**

615 Drug therapy is administered at a fixed time after infection and remains activated for the duration of the simulation. (A)  
 616 Sample treatment, showing the time course of  $r_{max}$ .  $r_{max}$  is reduced by a multiplier which is one minus the potency of  
 617 the drug at the given dose, 75% in (A), at a particular time of initiation of treatment (time delay of application), 12000  
 618 minutes (200 hours, 8  $\frac{1}{3}$  days) in (A). (B) A parameter sweep of the potency of treatment (reduction in baseline viral  
 619 replication rate  $r_{max}$ , vertical) and the time of treatment (dashed lines, horizontal) shows parameter regions where the  
 620 majority of simulation replicas produce positive outcomes (green-shaded subplots), negative outcomes (orange-shaded  
 621 subplots) and intermediate cases (intermediate shading or unshaded). Intensity of green and orange indicates the  
 622 number of positive and negative outcome replicas for each parameter combination (treatment effectiveness). Green  
 623 regions show that early intervention leads to positive outcomes (is effective) for most ranges of treatment potency, with

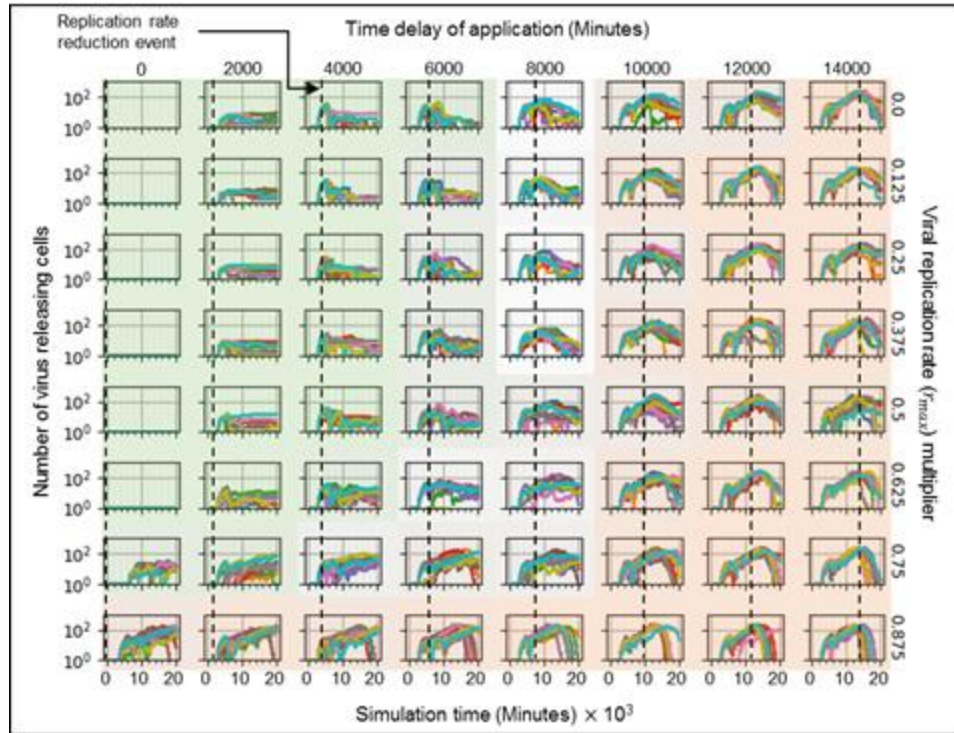


624 high numbers of uninfected epithelial cells at the end of the simulation for almost all simulation replicas. Orange regions  
625 show that late interventions result in mostly negative outcomes (ineffective treatment) regardless of the potency, and  
626 that outcomes are more variable between replicas, with both positive and negative outcomes for most parameter sets.  
627 The number of uninfected epithelial cells for each simulation replica for each parameter set, plotted on a logarithmic  
628 scale, vs time displayed in minutes.

629

630         When the treatment is given early, while the level of extracellular virus is increasing  
631 rapidly and exponentially (before 6000 minutes, 100 hours, 4 days) after infection, most  
632 of the simulation replica outcomes are positive, showing effective treatment (Figs 9-11,  
633 green-shaded subplots). If the drug is administered prophylactically or very soon after  
634 infection (at 0 minutes) the treatment potency needs to be only 25% to achieve mostly  
635 positive outcomes (effective treatment). Increasing the time to treatment increases the  
636 potency required to achieve similar numbers of positive outcomes: the treatment is  
637 effective for a potency of at least 37.5% if administered by 4000 minutes (67 hours, 2 <sup>3</sup>/<sub>4</sub>  
638 days), and at least 87.5% if administered by 6000 minutes (100 hours, 4 days). For all  
639 potencies greater than 12.5%, early intervention prevents significant increase in the  
640 number of virus-releasing cells (Fig 9, green-shaded subplots), and a small number of  
641 immune cells suffices to stop the spread of infection (Fig S9, green-shaded subplots). In  
642 this region, delaying treatment results both in a higher level of extracellular virus (Fig 10,  
643 green-shaded subplots) and more dead epithelial cells at the end of simulation (Fig 8,  
644 green-shaded subplots). With inhibited viral replication in the infected epithelial cells, the  
645 extracellular virus decays until it is mostly cleared by the end of simulation (Fig 10).  
646 Variability between simulation replicas for a given parameter set increases with both  
647 decreasing potency and increasing time of initiation of treatment.

648



649

650 **Fig 9. Number of virus releasing cells vs time in simulations of a hypothetical drug treatment reducing the viral**  
 651 **genome (e.g. RNA for SARS-CoV-2) replication rate ( $r_{max}$ ) as a function of treatment potency (one minus the**  
 652 **viral replication rate multiplier) and time of initiation of treatment.**

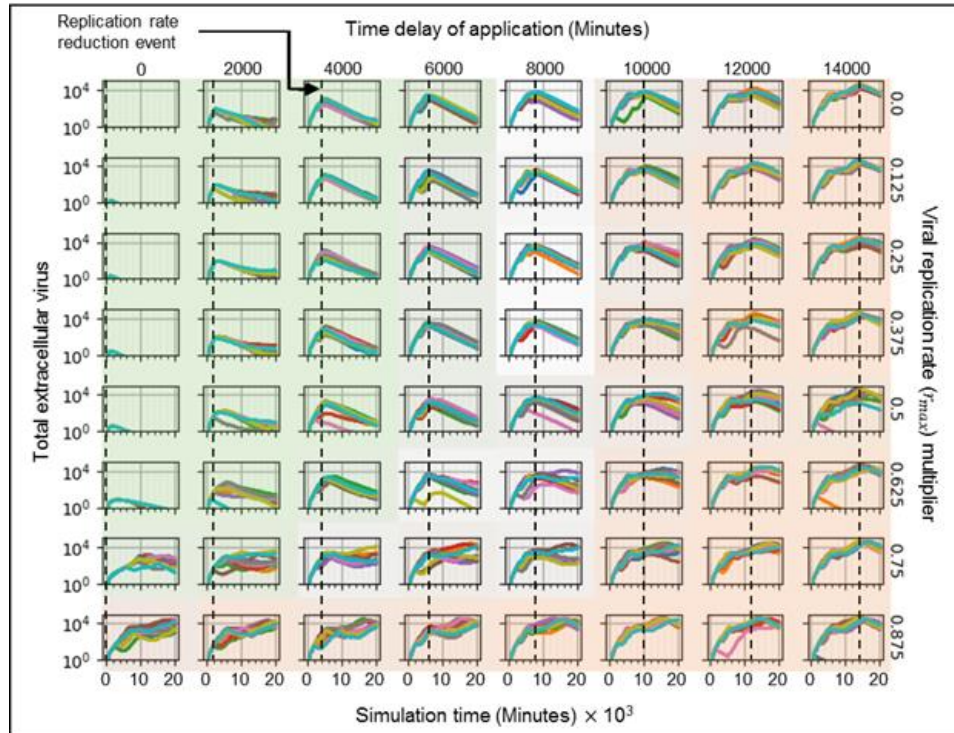
653 The number of virus-releasing epithelial cells stays low when the intervention occurs early during infection (when the  
 654 amount of extracellular virus is increasing rapidly), but continues to increase when the intervention occurs later (when  
 655 the level of extracellular virus is at or near its maximum in the untreated case). Parameter values, axis types and time-  
 656 scale and shading as in Fig 8.

657

658 If the potency of the treatment is 12.5% (or less), most of the simulation replicas  
 659 have negative outcomes (low effectiveness), even if the drug is administered  
 660 prophylactically or soon after infection (at 0 minutes) (Figs 9-11, bottom row). In these  
 661 cases, the time after infection at which the drug is given makes no significant difference  
 662 to the treatment effectiveness. When the treatment is given late (time delay of application  
 663 of at least 10000 minutes, 167 hours, 7 days), regardless of the potency of the drug, most  
 664 simulation replicas have negative outcomes (Figs 9-11, orange-shaded regions). By the

665 time of treatment, a significant number of epithelial cells have been infected (more than  
666 10% in most cases – Fig 9, orange-shaded regions) and a significant amount of virus has  
667 been released into the extracellular environment (Fig 10, orange-shaded regions). In  
668 addition, a significant number of epithelial cells have died (more than 10% in most cases  
669 – Fig S7, orange-shaded regions) and significant recruitment of immune cells has  
670 occurred (Fig S9, orange-shaded regions). For higher treatment potency, the level of virus  
671 in the extracellular environment starts decreasing immediately after treatment, even when  
672 a significant number of virus-releasing epithelial cells remain, indicating that viral  
673 replication inside cells has been significantly reduced. Later intervention also increases  
674 variability between simulation replicas and, although most simulation replicas have  
675 negative outcomes, the same set of parameter values produced two distinct qualitative  
676 outcomes (some more and some less favorable) for higher potency (Fig S11, orange-  
677 shaded regions). Thus in a few cases, even late treatment can be effective.

678



679

680 **Fig 10. Levels of extracellular virus vs time in simulations of a hypothetical drug treatment reducing the viral**  
 681 **genome (e.g. RNA for SARS-CoV-2) replication rate ( $r_{max}$ ) as a function of drug potency (one minus the viral**  
 682 **replication rate multiplier) and time of initiation of treatment.**

683 Extracellular virus is cleared or near-cleared when intervention occurs soon after infection. Parameter values, axis  
 684 types and time-scale and shading as in Fig 8.

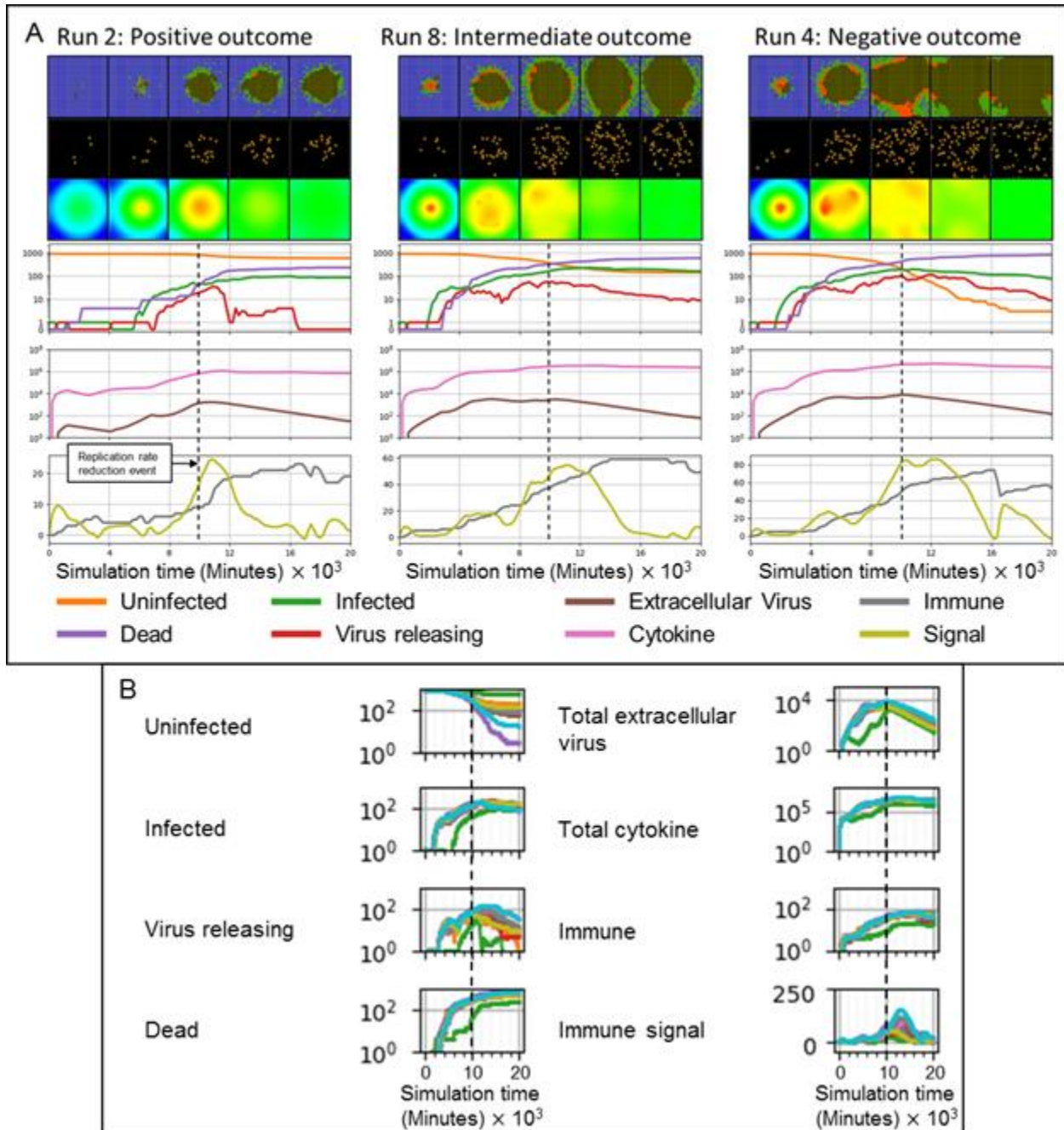
685

686 When the treatment is given at intermediate times (times between 6000 and 10000  
 687 minutes, 100 to 167 hours, 4 to 7 days), most simulation replicas have intermediate  
 688 outcomes. For potencies above 50%, the fraction of uninfected epithelial cells at the end  
 689 of simulation is relatively high (around 50%) and the treatment is usually moderately  
 690 effective (Fig 8). For potencies below 50%, the number of virus-releasing epithelial cells  
 691 remains approximately constant or continues to increase after treatment (Fig 9) and  
 692 significant levels of extracellular virus remain at the end of the simulation, and so in most



693 cases the treatment is ineffective (Fig 10). In this regime, variability between outcomes  
 694 for the same parameter values is higher than for potencies above 50%.

695



696

697 **Fig 11. Difference in treatment effectiveness for different simulation replicas for perfect treatment potency (0**  
698 **viral replication rate multiplier) near the time when the extracellular virus amount would reach its maximum in**  
699 **the untreated case (10000 minutes, 167 hours, 7 days).**

700 (A) Select simulation replicas for this parameter set showing the variety of possible outcomes (treatment effectiveness).  
701 Spatial results show the epithelial and immune cell layers, and the extracellular virus field, at 4000, 8000, 12000, 16000,  
702 and 20000 minutes (67, 133, 200, 267 and 333 hours,  $2\frac{3}{4}$ ,  $5\frac{1}{2}$ ,  $8\frac{1}{3}$ , 11 and 14 days). Cell type colors are the same  
703 as in Fig 3A. Virus field values are scaled as in Fig 3A. (B) Time series for all simulation replicas for the selected  
704 parameter set: Right column, from top to bottom, number of uninfected epithelial cells, number of infected epithelial  
705 cells, number of virus-releasing epithelial cells, number of dead cells. Left column, from top to bottom: total amount of  
706 extracellular virus, total amount of cytokine, number of immune cells and immune response state variable. All variables  
707 except the immune signal plotted on a logarithmic scale vs time.

708

709 A particular parameter set (time delay of application of 10000 minutes, 100%  
710 potency) produced simulation replicas that had instances of all three outcomes (Fig 11).  
711 In a simulation replica with a positive outcome (Run 2, Fig 11A), the first uninfected  
712 epithelial cell dies (as well as a few uninfected epithelial cells) before 4000 minutes (67  
713 hours,  $2\frac{3}{4}$  days), after which the total extracellular virus gradually decreases. At around  
714 4000 minutes (67 hours,  $2\frac{3}{4}$  days), an epithelial cell near the initially-infected cell  
715 becomes infected, causing a recurrence of infection, whose spread was stopped by the  
716 treatment. In contrast, simulation replicas with intermediate and negative outcomes (Runs  
717 8 and 4, respectively, Fig 11A) have comparable, and significantly more, numbers of  
718 infected and virus-releasing epithelial cells at 4000 minutes (67 hours,  $2\frac{3}{4}$  days), while  
719 total extracellular virus is greater in the replicas with a negative outcome than in the  
720 replicas with an intermediate outcome. For the positive outcome replica, after 10000  
721 minutes (167 hours, 7 days), the remaining extracellular virus infects just a few individual  
722 epithelial cells throughout the tissue. For the intermediate outcome replica, after 10000

723 minutes (167 hours, 7 days) the number of infected epithelial cells continues to increase  
724 until around 12000 minutes (200 hours, 8 ½ days) and then declines, while the number  
725 of uninfected epithelial cells slightly decreases at the end of the simulation. For the  
726 negative outcome replica, after 10000 minutes (167 hours, 7 days) the already depleted  
727 number of uninfected epithelial cells continues to rapidly decrease to near zero.

728

## 729 **Model extensions**

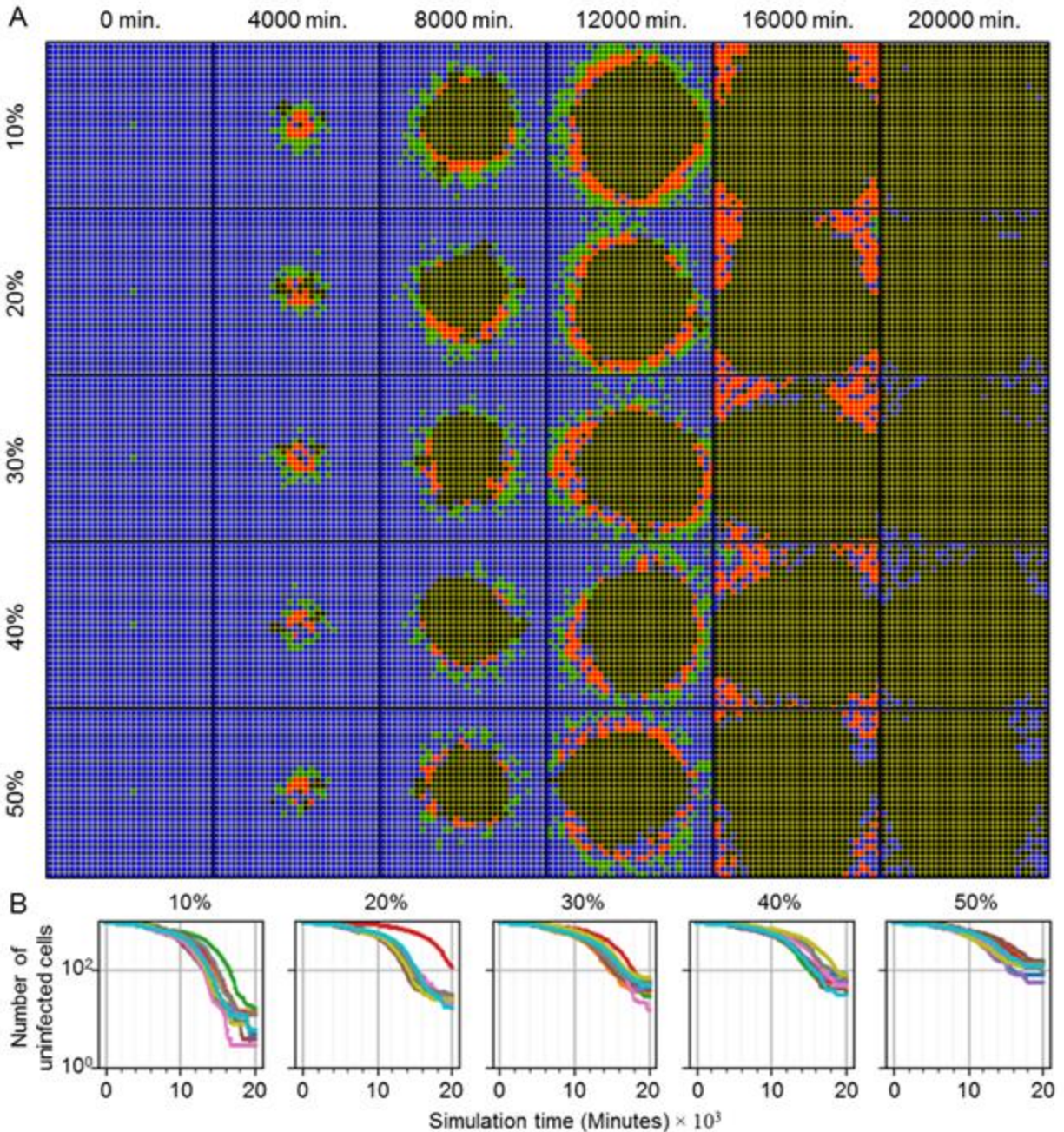
730 In this section we demonstrate the deployment of extensions to the framework  
731 described in *Models and methods*, which we will refer to as the “main framework” when  
732 discussing extensions in this and subsequent sections, as well as particularization of the  
733 framework to specific biological problems like a different virus. We accomplish this  
734 through integration of an existing model in the literature of hepatitis C virus (HCV), and  
735 elementary examples of adding models of heterogeneous epithelia and tissue recovery,  
736 one model of which is constructed from another. We include schematic representations  
737 where appropriate of the software implementation according to the architecture we have  
738 developed (and will continue to develop) to support broad scientific use through rapid,  
739 parallel model development, flexible model integration, and model sharing through our  
740 publicly available online repository (see *Collaborative viral infection modeling*  
741 *environment* for an overview of basic deployment, implementation, and public distribution  
742 of extensions).

743

744 **Heterogeneous susceptibility inhibits spread of infection.** To demonstrate basic  
745 extensibility of the framework to model additional complexity associated with viral

746 infection, we introduced a basic notion of heterogeneity to the epithelium of simulated  
747 scenario with the premise that not all epithelial cells can be infected (*i.e.*, some cells are  
748 unsusceptible, as in an actual heterogeneous respiratory epithelium) [22]. We  
749 implemented heterogeneous susceptibility by randomly selecting a fraction of the  
750 epithelial cell population at the beginning of simulation and setting the number of surface  
751 receptors of each to zero (*i.e.*, these cells have no surface receptors for internalization of  
752 the virus). Otherwise, all mechanisms and model parameter values used in simulations  
753 of heterogeneous susceptibility were the same as those used to generate results shown  
754 in Fig 3 (*i.e.*, all mechanisms described in *Models and methods* using the baseline  
755 parameter set). Implementation of randomly selected heterogeneous susceptibility is  
756 available in the add-on modules library and is hosted on our repository for public use with  
757 the module name “RandomSusceptibility”. For each set of replicas we simulated ten  
758 replicas using the RandomSusceptibility module while varying the fraction of  
759 unsusceptible cells (like different locations in the lungs), from 10% to 50% unsusceptible  
760 in intervals of 10% (Fig 12).  
761





762

763 **Fig 12. Randomly distributed unsusceptible cells inhibit but do not stop spread of infection throughout the**  
764 **tissue.**

765 (A) Distributions of epithelial cells during simulation time (columns) for varying fraction of unsusceptible cells (rows).  
766 From top to bottom, replicas were simulated with 10%, 20%, 30%, 40% and 50% of epithelial cells unsusceptible to  
767 viral internalization. Cell type colors are the same as in Fig 3A. (B) Number of uninfected cells during simulation time  
768 for ten replicas of each fraction of epithelial cells unsusceptible.

769

770 For all fractions of unsusceptible cells, infection spread throughout the epithelial  
771 sheet (Fig 12A). No replica produced the exact definition of widespread infection, since  
772 all replicas had at least some remaining uninfected cells at the end of simulation.  
773 However, only eight out of fifty total replicas had a few epithelial cells that were not either  
774 uninfected or dead at the end of simulation (for infected cells, 1 replica for 10%  
775 unsusceptible, and for virus-releasing 1 replica for 10% and 20% unsusceptible, and 2  
776 replicas for 30%, 40% and 50% unsusceptible). The distributions of infected and virus-  
777 releasing cells were notably different from all previous simulations with appreciable  
778 infection in that both subpopulations were noticeably intermixed with uninfected  
779 (presumably unsusceptible) cells and increasingly so with increasing fraction of  
780 unsusceptible cells. Most of these intermixed, uninfected cells (particularly those nearer  
781 to the initial site of infection) also died due to immune response mechanisms (*i.e.*,  
782 bystander effect and oxidative killing).

783 The final number of uninfected cells at the end of simulation increased with an  
784 increasing fraction of unsusceptible cells (Fig 12B). The rate of spread of infection  
785 decreased with an increasing fraction of unsusceptible cells (as observed by inspection  
786 in a rightward shift in the total number of uninfected cells). One replica for 20%  
787 unsusceptible cells exhibited significantly delayed spread of infection, though this was not  
788 observed in other replicas for any other fraction of unsusceptible cells.

789

790 **Integration of an explicit RNA synthesis model allows the spatiotemporal modelling**  
791 **of hepatitis C virus infection.** The viral replication model described in *Models and*

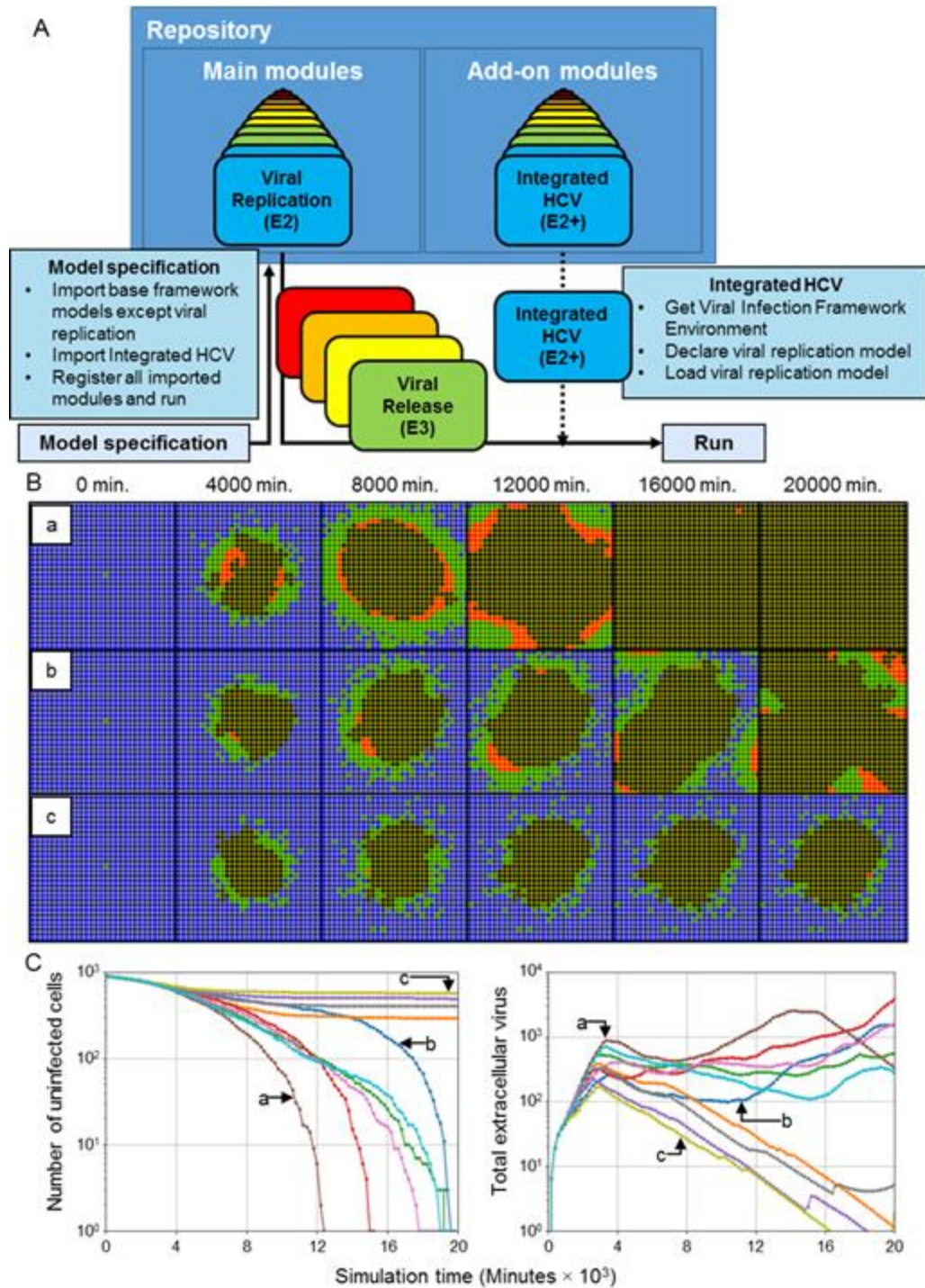
792 *methods* describes the viral life cycle, from internalization to release, as occurring over  
793 four stages and in unitless quantities. As such, it is possible to integrate detailed models  
794 of various stages of the viral life cycle into the main framework through appropriate  
795 substitution of viral replication model terms and assignment of unit quantities as  
796 necessary (*i.e.*, one unit in the original viral replication model corresponds to a physical  
797 unit in an integrated model that explicitly describes a lifecycle process). Integration of a  
798 detailed model of some viral process then particularizes the virus represented in the main  
799 framework to the level of biological information introduced by the integrated model.

800 As a demonstration of model integration, we particularized viral replication of the  
801 framework to hepatitis C virus (HCV) using an existing model of subgenomic HCV RNA  
802 synthesis in Huh-7 cells [59]. The model of HCV RNA synthesis describes various aspects  
803 of subgenomic HCV replication like translation of HCV polyprotein in the cytoplasm,  
804 replication kinetics in vesicular-membrane structures and availability of host ribosomes,  
805 and explicitly models quantities of HCV RNA molecules, translation complexes, HCV  
806 polyprotein molecules, and necessary enzymes in both the cytoplasm and vesicular-  
807 membrane structures.

808 Integration of the HCV replication model casts the viral genome taking part in  
809 genome replication  $R$  of the viral replication module described in *Models and methods* as  
810 the cytoplasmic plus-strand HCV RNA molecules of the HCV replication model (denoted  
811  $R_p^{cyt}$ , see *Integration of an explicit RNA synthesis model*). We assumed that internalized  
812 virus from the viral internalization module converts into cytoplasmic RNA, and that some  
813 of the decay of cytoplasmic RNA molecules described in the HCV model leads to the  
814 production of quantities produced by replicating viral genome from the viral replication

815 module. To relate the unitless viral replication model described in *E2 - Viral Replication*  
816 to the biological quantities of the HCV replication model, we assumed that one unit of  
817 replicating viral genome corresponds to 100 HCV RNA molecules, which was found to  
818 produce total infection dynamics comparably to the main framework (for comparison with  
819 results of this work, rather than for reproduction *in silico* of any specific HCV data) when  
820 using both the baseline parameter set demonstrated in Fig 3 and all model parameters  
821 reported in [59] when the virus-receptor association affinity coefficient  $k_{on}$  was increased  
822 by a factor of 100 (Table S2). The integrated HCV model is implemented in the add-on  
823 modules library using the aforementioned software architecture and is hosted on our  
824 repository for public use with the module name “HCVIntegrated” (Fig 13A).  
825





826

827 **Fig 13. Basic integration of an explicit model of hepatitis C virus subgenomic replication in a spatial context**  
 828 **presents stochastic outcomes in ten simulation replicas.**

829 (A) Schematic of implementing the integrated HCV model using the available modules described in *Models and*  
 830 *methods* ("Main modules") and add-on modules libraries hosted in the framework public repository. All main modules

831 are imported except Viral Replication, which is replaced with Integrated HCV. Modules used in a simulation are  
832 specified in model specification. The integrated HCV model module is available in the add-on modules library. (B)  
833 Distributions of epithelial cells during simulation time for select replicas (labeled “a”, “b” and “c”) using the integrated  
834 HCV model. Cell type colors are the same as in Fig 3A. (C) Number of uninfected cells (left) and total extracellular virus  
835 (right) during simulation time for ten replicas using the integrated HCV model. Select results shown in (B) are annotated  
836 according to replica labels “a”, “b” and “c”.

837

838         Ten simulations were executed using the integrated HCV model for a simulation  
839 time of two weeks using initial conditions similar to some used in [59], where the initially  
840 infected cell was seeded with 500 cytoplasmic viral RNA molecules (*i.e.*, initial  $R = 5$ ,  
841 rather than initial  $U = 1$  as in all other simulations). Spread of infection with the integrated  
842 HCV model produced comparable patterns of spread of infection, where an infection front  
843 radially advanced outward from the initial site of infection (Fig 13B). However, one notable  
844 difference was that the prominent band of virus-releasing cells during spread of infection  
845 only occurred in some simulation replicas (Fig 13B, replica “a”), while in other replicas  
846 only small, isolated groups of cells became virus releasing (Fig 13B, replicas “b” and “c”).  
847 Variability of outcomes was particularly notable among the ten simulation replicas. Some  
848 simulation replicas produced widespread infection at a comparable timescale to that of  
849 the baseline parameter set, between one and two weeks (Fig 13C). Such simulation  
850 replicas were those that produced comparable spatial distributions of infected and virus-  
851 releasing cells (specifically, with a prominent band of virus-releasing cells) to those of the  
852 main framework using the baseline parameter set. In other simulation replicas (*e.g.*, Fig  
853 13B, replica “c”), slowed infection occurred due to early elimination of many virus-  
854 releasing cells. In such cases, the epithelial sheet had very few virus-releasing cells and  
855 scattered infected cells around the region of dead cells.

856 Many infected cells remained infected over a period of over a week, which was not  
857 observed using the viral replication model of the main framework. Such infected cells did  
858 not contribute to spread of infection, but rather diminished the likelihood of widespread  
859 infection by increasing the distance between uninfected and virus-releasing cells. By the  
860 end of simulation in replicas that produced slowed infection, total extracellular virus was  
861 negligible despite a significant number of infected cells, which presents an outcome not  
862 described in *Classification of spatiotemporal infection dynamics* that could be called  
863 “benign infection”.

864

865 **An extensible framework architecture enables the inclusion of tissue recovery.** As  
866 a demonstration of modularity and extensibility, we developed, implemented and tested  
867 two models of tissue recovery, where dead cells are replaced over time with uninfected  
868 cells. Since epithelial cells in the simulated epithelial sheet are static, removal of dead  
869 cells and proliferation of uninfected cells was modeled as the changing of the type of a  
870 dead cell to uninfected (rather than explicitly modeling mitosis, [18]). To generate a  
871 scenario of viral clearance and significant tissue damage, we simulated the baseline  
872 parameter set with the parameter variations in the top-right corner of Figs 5-7, where viral  
873 internalization is severely inhibited and the immune response is very strong and fast (*i.e.*,  
874 parameters  $k_{on}$  and  $\beta_{delay}$  were reduced by a factor of 100 so that the virus is cleared but  
875 many uninfected cells die).

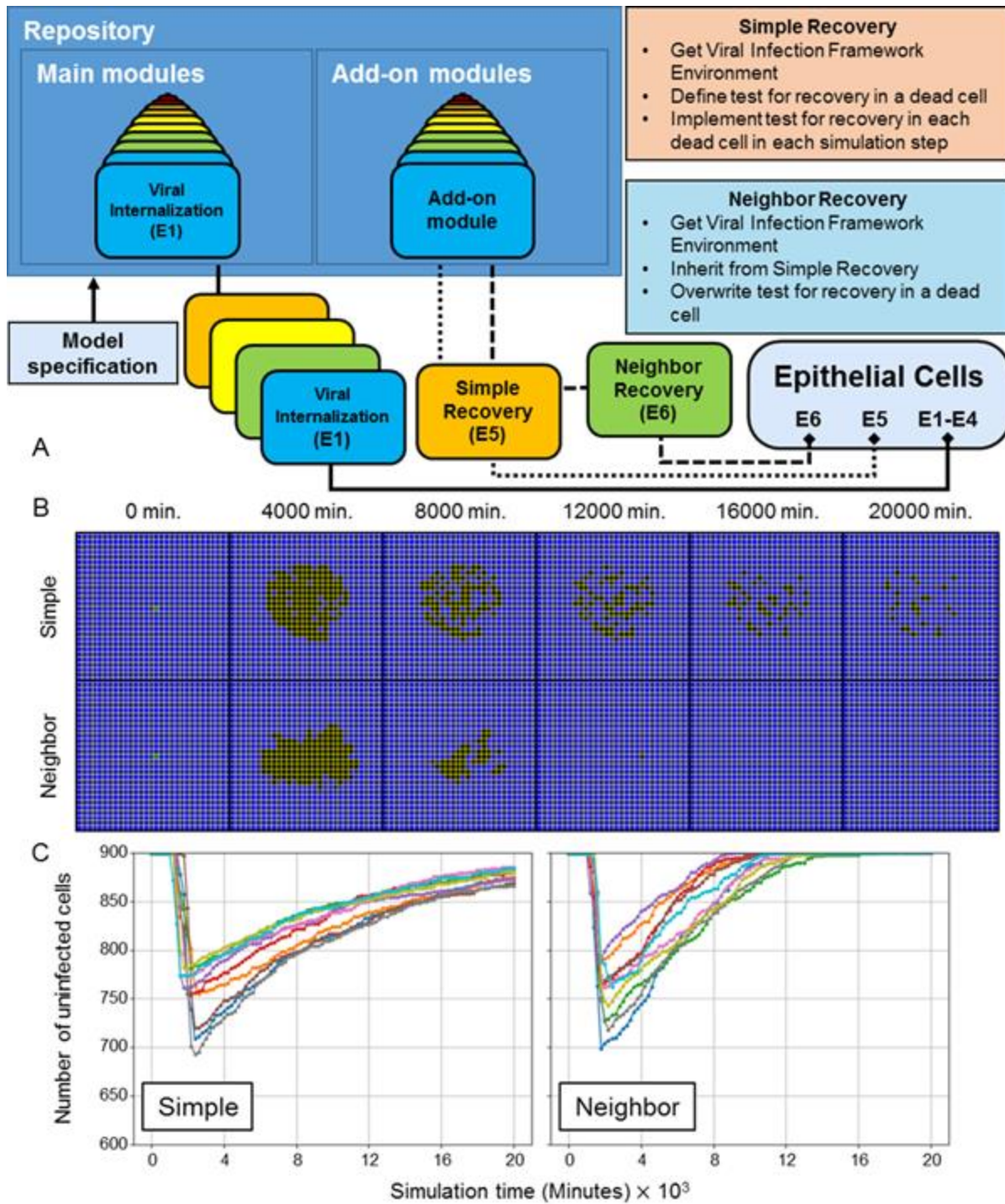
876 In the first model of tissue recovery, called “Simple Recovery”, dead cells are  
877 replaced by an assumed layer of proliferative cells underneath the simulated epithelial  
878 patch, and so each dead cell has a fixed probability of recovering. We approximated the



879 probability of recovery based on an assumed onset of tissue recovery of 7 days, in which  
880 case the probability of recovery for each dead cell over a 20-minute simulation step was  
881  $1.98 \times 10^{-3}$ . In the second model of tissue recovery, called “Neighbor Recovery”, dead  
882 cells are replaced by nearby uninfected cells similarly to wound healing, and so each  
883 dead cell has a probability of recovery equal to the number of neighboring uninfected cells  
884 multiplied by a coefficient. For comparison of results to those from the Simple Recovery  
885 add-on module, we used the same probability coefficient value such that the probability  
886 of recovery according to Simple Recovery for each dead cell over a 20-minute simulation  
887 step was  $1.98 \times 10^{-3}$  per unit of contact area with neighboring uninfected cell (measured  
888 in number of neighboring lattice sites).

889 Both models were implemented in CompuCell3D in the add-on modules library  
890 using the aforementioned software architecture and is hosted on our repository for public  
891 use. The Simple Recovery model is hosted with the module name “RecoverySimple”, and  
892 the Neighbor Recovery model is hosted with the module name “RecoveryNeighbor”.  
893 Since the only difference between the two recovery models is the criterion for cell recovery  
894 (*i.e.*, whether a fixed probability, or a probability according to the neighborhood of a cell),  
895 the implementation of the Neighbor Recovery model inherits all features of the Simple  
896 Recovery model implementation using basic Python class inheritance, and required  
897 overwriting only one function that implements a criterion of cell recovery during  
898 development (Fig 14A, see *Extending a model in CompuCell3D*).

899



900

901 **Fig 14. Even simple model extensions and extensions of extensions can produce notably different**  
 902 **spatiotemporal emergent features.**

903 (A) Schematic of implementing a modified epithelial cell model using the available modules described in *Models and*  
 904 *methods* ("Main modules") and add-on modules libraries hosted in the framework public repository. Modules used in a

905 simulation are specified in model specification. The Simple Recovery and Neighbor Recovery model modules are  
906 available in the add-on modules library. (B) Distribution of epithelial cells during simulation time using the Simple  
907 Recovery (top) and Neighbor Recovery (bottom) models. Cell type colors are the same as in Fig 3A. (C) Number of  
908 uninfected cells during simulation time for ten simulation replicas using the Simple Recovery (left) and Neighbor  
909 Recovery (right) models.

910

911 All simulation replicas for each recovery model began with tissue insult due to  
912 oxidative killing by a strong and fast immune response through the first few days (Fig  
913 14B). All simulation replicas experienced a loss of approximately 100-200 uninfected cells  
914 (Fig 14C). An increasing number of uninfected cells clearly demonstrated immediate  
915 effects of modeling recovery after oxidative killing subsided (a trend not seen in previous  
916 results), where the Simple Recovery model almost completely replenished all killed  
917 uninfected cells by the end of simulation, and the Neighbor Recovery model replenished  
918 all killed uninfected cells between 8,000 and 13,000 minutes. Neighbor-dependence of  
919 the Neighbor Recovery model generated a significantly different distribution of dead cells  
920 after oxidative killing, where dead cells were scattered throughout the original region  
921 where cells died when using the Simple Recovery model while the region where cells died  
922 shrank over time when using the Neighbor Recovery model.

923

## 924 **Discussion**

925 Our spatial, multicellular model of primary acute viral infection of an epithelial  
926 tissue includes key aspects of viral infection, viral replication and immune response. By  
927 investigating sensitivity to model parameters and simulating drug therapies, we identified  
928 six distinct spatiotemporal classes of infection dynamics based on the model's transient

929 behaviors and final configurations. Each of our simulation-defined classes corresponds  
930 to biologically or clinically observable factors and outcomes. The case of no immune  
931 response would be useful for analyzing *in vitro* experiments (e.g., organoids). Widespread  
932 infection corresponds to an initial infection that is likely to spread to surrounding tissue  
933 and cause major tissue damage. Slowed infection corresponds to an initial infection  
934 whose spread is more likely to be eliminated by the adaptive immune response.  
935 Containment corresponds to immune-cell elimination of all infected cells but where  
936 remaining extracellular virus could result in new sites of infection elsewhere. Recurrence  
937 corresponds to the situation when new lesions form within the observed tissue patch.  
938 Clearance corresponds to immune-cell-based elimination of all infected cells and  
939 extracellular virus (classical viral clearance).

940 We showed that key parameters of the model, such as those affecting viral  
941 internalization (i.e., virus-receptor association affinity  $k_{on}$ ), can lead to both  
942 containment/clearance (e.g., small  $k_{on}$ , Figs 5-7) and widespread infection (e.g., large  
943  $k_{on}$ , Figs 5-7). Multidimensional parameter sweeps showed how the interplay between  
944 immune response (e.g. immune response delay coefficient  $\beta_{delay}$ ) and viral spread could  
945 lead to widespread infection (e.g., large  $\beta_{delay}$ , large  $k_{on}$ , Figs 5-7), rapidly cleared  
946 infection (e.g., small  $\beta_{delay}$ , small  $k_{on}$ , Figs 5-7) or containment/clearance after substantial  
947 damage (e.g., small  $\beta_{delay}$ , moderate  $k_{on}$ , Figs 5-7). Some of these outcomes would be  
948 expected biologically (e.g., very fast internalization with a slow immune response is likely  
949 to lead to widespread infection; faster and stronger immune responses should control the  
950 spread of viral infection within the tissue [Figs 5-7]) and would also occur in deterministic  
951 non-spatial models. Others, like the coexistence of replicas with containment/clearance

952 or failure to control for the same parameter set, are less expected, and could not occur in  
953 a deterministic non-spatial model (though they might occur in some stochastic non-spatial  
954 models). We have observed this interplay of parameters, as well as the potential for  
955 stochastic outcomes, in variations of other parameters of the model, whether related to  
956 spatial (e.g., viral and cytokine diffusion coefficients) or deterministic and stochastic  
957 cellular aspects (oxidative agent threshold for death and virally-induced apoptosis  
958 dissociation coefficient, see *Figs S17-S22*).

959 We studied the influence of timing and potency of an RNA-polymerization inhibitor  
960 like remdesivir [60] on the spread of viral infection within tissue (Figs 9-11). As expected,  
961 in our model, drugs with this mode of action can improve viral control in tissue if  
962 administered prophylactically at high potency, and their effectiveness decreases the later  
963 they are administered. Less obviously, the lower-left region of Figs 9-11 shows how  
964 therapies with even reduced potency could control the infection when administered  
965 sufficiently early, consistently with predictions from a deterministic, non-spatial ODE  
966 model published after submission of this manuscript for publication (though the mode of  
967 action is not explicitly described) [61]. While we expect prophylactic or early treatment at  
968 the same potency to be more effective than later treatment, our model suggests that, for  
969 antivirals, time of treatment is a more significant factor than potency in determining the  
970 effectiveness of the therapy. Our model thus suggests that drugs that interfere with virus  
971 replication are significantly more effective if used even at very low doses prophylactically  
972 or very soon after infection, than they would be if used even at a high dose as a treatment  
973 given later after exposure. Specifically, a prophylactic treatment in simulation which  
974 reduces the rate of viral RNA synthesis by only 35% (35% potency) is more effective than



975 a treatment with 100% potency given two and a half days after infection, and has about  
976 the same efficacy as a treatment with 50% potency given one day after infection. Our  
977 model also showed that because of stochasticity in viral spread, later treatment at  
978 moderate to high potency may still be effective in a subset of individuals.

979 Both parameter sweeps had regions with little variation in outcome between  
980 replicas (*e.g.*, the upper-right and lower-left corners of Fig 5). In regions of the parameter  
981 space between these extremes (*e.g.*, the unshaded areas in Figs 5 and 9), different  
982 replicas showed dramatically different outcomes. One such parameter set in our drug  
983 therapy simulations produced three distinct qualitative outcomes (*i.e.*, positive,  
984 intermediate and negative outcomes, Fig 11). For these parameters, replica outcomes  
985 were particularly sensitive to stochasticity early in infection when only a few cells were  
986 infected (Fig 11A), with delayed spread of infection from the first infected cell producing  
987 more positive outcomes. Simulation replicas with negative outcomes (Fig 11A, Run 8)  
988 had higher extracellular virus levels at earlier times than those with intermediate  
989 outcomes (Fig 11A, Run 4), even though the fraction of each cell type was similar. Since  
990 the viral replication module is deterministic, the primary cause of this difference is the  
991 spatial distribution of cells. Spatial structure (*e.g.*, infection of neighboring cells),  
992 stochastic events (*e.g.*, early cell death of infected cells before significant virus release)  
993 and cell-to-cell variation (*e.g.*, difference in viral release between cells) all affect the  
994 variation between replicas.

995 Differences in spatiotemporal dynamics and variability of outcomes thus critically  
996 depend on the ability of the model to resolve the spread of virus and immune response  
997 spatially. The intrinsic stochasticity of many model processes makes the spatial patterns

998 of the infection front and distribution of tissue damage nontrivial. The spectrum of  
999 outcomes in our parameter sweeps (Figs 5-7 and 9-11) depends not only on parameter  
1000 values and model immune response, but also on the emergent spatial patterns of cytokine  
1001 and virus fields (e.g., variations within the infection front expose different numbers of  
1002 uninfected epithelial cells to the immune response). Such stochastic and spatial aspects  
1003 can also introduce new considerations to ODE models that have been primarily employed  
1004 in a non-spatial context. For example, as described in the original presentation of the HCV  
1005 model that was integrated in *Integration of an explicit RNA synthesis model allows the*  
1006 *spatiotemporal modelling of hepatitis C virus infection*, the subgenomic kinetics of the  
1007 HCV model require a minimum number (seven) of cytoplasmic viral RNA molecules to  
1008 reach a saturated state. When employing the HCV model in a multicellular,  
1009 heterogeneous context, insufficient internalization of a spatially heterogeneous  
1010 extracellular viral field for subgenomic replication to produce rampant viral production,  
1011 leading to insufficient cytokine signaling to invoke further immune response, makes  
1012 possible the so-called outcome of benign infection.

1013

#### 1014 **Future perspectives**

1015 Our modeling framework can improve with the inclusion of additional cellular and  
1016 immune mechanisms discussed in Fig 1. The modularity of model modules and built-in  
1017 extensibility of the publicly available software implementation enables us, and other  
1018 interested members of the scientific community, to accomplish such activities  
1019 collaboratively or independently, concurrently, and even when in theoretical  
1020 disagreement (see *Collaborative viral infection modeling environment*). Modules



1021 accounting for viral clearance, tissue recovery and persistent adaptive immune response  
1022 can be added to model later stages of disease progression (as demonstrated in *Model*  
1023 *extensions*). The current immune model does not include important signaling factors (*e.g.*,  
1024 interferon-induced viral resistance in epithelial cells) and the different roles of tissue-local  
1025 and systemic signals (*e.g.*, various cytokines). It also omits many cell types associated  
1026 with both innate and adaptive immune response and their roles (*e.g.*, viral scavenging by  
1027 macrophages, relaying and amplification of immune signals by dendritic cells). Of special  
1028 interest to results like those presented in this work is the effect of specific roles by  
1029 individual immune cell phenotypes on emergent dynamics and outcomes, considering  
1030 that the timing of their activities during progression of events can be quite different (*e.g.*,  
1031 early neutrophil release of oxidative agent contrasted with later effector T-cell contact-  
1032 mediated killing). Such details, which we are currently pursuing, are particularly important  
1033 for using framework to interrogate the spatiotemporal details of the immune response,  
1034 which are poorly understood. The model does not currently consider the production and  
1035 role of antibodies in the humoral immune response or tissue recovery after damage (like  
1036 the demonstration models presented in *An extensible framework architecture enables the*  
1037 *inclusion of tissue recovery*). The model also greatly simplifies the structure of the  
1038 epithelium and its environment, but could be easily generalized to a detailed, three-  
1039 dimensional geometry, albeit at the cost of computational performance.

1040 Our current results suggest priorities for improving the biological realism within  
1041 existing modules, and for including modules representing additional biological  
1042 components and mechanisms. We are currently implementing virus-scavenging by  
1043 immune cells and local antiviral resistance due to Type 1-IFN paracrine signaling by

1044 epithelial cells. We are calibrating the virus replication module to existing experimental  
1045 data for SARS-CoV-2 and influenza A. Because different tissues within the body have  
1046 different responses to local viral infection, developing our framework to support the  
1047 modeling and simulation of multi-organ disease progression (*e.g.*, by identifying model  
1048 parameters corresponding to specific tissues and physiological compartments) would  
1049 allow us to understand the highly variable whole-body progression of many viral diseases.

1050         The immune response to viral infection depends on locus of infection, degree of  
1051 infection and patient immune state. Understanding the reasons for immune failure to  
1052 contain infection, or pathological responses like cytokine storms or sepsis, requires  
1053 models of immune response at multiple locations and scales. The same is true for  
1054 understanding and predicting the possible protective or adverse effects of coinfection.  
1055 The number of permutations of infection timing and combination of pathogens is too large  
1056 to address purely by experiments, but could be addressed by simulations. Spatial  
1057 modeling is also important because the spatiotemporal dynamics of coinfection within  
1058 tissues may be important to the outcome (*e.g.*, whether individual cells can be  
1059 superinfected, whether viral lesions with a tissue are disjoint or overlap, whether the main  
1060 foci of the pathogens are in the same or different tissues).

1061         We can also study the systemic effects of possible therapies with known molecular  
1062 modes of action (as seen in *Results*). Evaluating therapies in a simulated context prior to  
1063 performing animal or human trials could lead to more effective and rapid drug discovery  
1064 and to optimized dosage and timing of treatments. Understanding the origins of  
1065 population variability in disease progression is crucial to providing optimal personalized  
1066 treatment. While the simulations presented here begin with a single infected cell, a

1067 simulation which begins with multiple infected cells might better represent the infection  
1068 dynamics of patients that have been subject to high level exposure, such as healthcare  
1069 workers. Factors such as hypertension, immunosuppression and diabetes affect tissue  
1070 state and immune response and could also be incorporated into our model. More detailed  
1071 studies of these factors using our model could reveal more about the effects of population  
1072 variability (due to age, genetic variation, prior drug treatment or immune status) on  
1073 disease progression. Such computational studies could be accomplished using  
1074 concomitant, calibrated ODE-based simulations of COVID-19 treatment published as  
1075 recently as after the initial submission of this manuscript for publication [61].

1076 We are working to implement validated non-spatial models of viral infection and  
1077 immune response as agent-based spatial models (e.g., viral production, cytokine  
1078 secretion, tissue damage). By starting with a validated model that uses ordinary  
1079 differential equations and adding spatial components gradually, we can calibrate our  
1080 spatial models and validate our results. In ongoing work, we have developed a formal  
1081 method for spatializing ODE models and employing their parameters such that these  
1082 analogous spatial models reproduce the ODE results in the limit of large diffusion  
1083 constants. Using this method, we can combine the ability to do rapid formal parameter  
1084 identification of ODE-based models and to leverage published ODE model parameters  
1085 with the flexibility of spatial modeling. In these cases, any differences between the ODE  
1086 results and the spatial model can be definitively attributed to spatialization (e.g. the local  
1087 spread of virus or cytokine or the limited speed of movement of immune cells), or to  
1088 additional factors which are difficult to include in an ODE model (e.g., the variability of  
1089 individual cells or the complex time course of virus release by individual infected cells).

1090 We have developed formal spatializations of a number of interesting ODE models of  
1091 COVID, such as [61,62], to explore the effects of stochasticity of outcomes, the effects of  
1092 spatial mechanisms, and infection dynamics at a particular site of infection on the  
1093 predictions of these models. An additional benefit of our approach is that we can easily  
1094 and consistently combine and integrate ODE models which focus on different aspects of  
1095 the complex process of infection, spread and clearance (*e.g.*, combining published  
1096 models of intracellular INF-induced viral resistance with spatial models of plaque spread  
1097 *in vitro* [20,63]). We illustrate both of these strengths in *Integration of an explicit RNA*  
1098 *synthesis model allows the spatiotemporal modelling of hepatitis C virus infection*, where  
1099 we integrate a published HCV model of subgenomic replication into our framework. We  
1100 can also conduct simultaneous, cross-platform validation of spatial models by building  
1101 multiple implementations of the same conceptual and quantitative models on independent  
1102 modeling platforms (here Chaste [64,65] and Morpheus [66]).

1103         The COVID-19 crisis has shown that drug discovery and therapy development both  
1104 require new predictive capabilities that improve their effectiveness and efficiency. We  
1105 have developed our framework to explore the relationship between molecular, cellular-  
1106 level and systemic mechanisms and outcomes of acute viral infections like SARS-CoV-  
1107 2, and to support development of optimal, patient-specific treatments to combat existing  
1108 and new viruses.

1109

## 1110 **Models and methods**

1111         In this section we first present our model as a high-level conceptual model where  
1112 we list each process included in an implementation-independent manner. We then detail

1113 the quantitative model and its computational implementation, which uses a Cellular Potts  
1114 representation of cellular dynamics. All quantitative models are implemented in a  
1115 modular, extensible simulation architecture built using the CompuCell3D simulation  
1116 environment, which is publicly available for download and further development by  
1117 interested members of the scientific community (see *Collaborative viral infection modeling*  
1118 *environment*).

1119

### 1120 **Conceptual model: biological hypotheses and assumptions**

1121 As discussed in *Introduction* (Fig 2A) we consider viral propagation in an epithelial  
1122 tissue and a lymph node. The tissue contains two interacting spatial components: an  
1123 epithelium component (consisting of a monolayer of epithelial cells), and an extracellular  
1124 environment component (containing immune cells, extracellular virus and chemicals).  
1125 The lymph node component (whose state is affected by signaling from the tissue) adds  
1126 immune cells to the extracellular space when in a proinflammatory state and removes  
1127 them when in an anti-inflammatory state. A set of processes and interactions govern how  
1128 the states of these components evolve in time. We detail these components, processes  
1129 and interactions in the following subsections and in Fig 2.

1130

1131 **Epithelium component.** The epithelium component of the model represents the layer of  
1132 epithelium in the tissue, and is composed of epithelial cells of four types: uninfected,  
1133 infected, virus-releasing and dead (Fig 2C). We assume that the epithelial cells are  
1134 immobile. We implicitly model the ECM by considering its influence on all processes in  
1135 the epithelium component. The epithelial cells contain modules that describe the viral life

1136 cycle and approximate the amount of virus as a continuous quantity (Fig 2B), including:  
1137 binding and internalization of viral particles from the extracellular environment (**E1**),  
1138 intracellular replication (**E2**) and release (**E3**) of synthesized virus into the extracellular  
1139 environment, as well as cell death caused by viral-replication-associated damage,  
1140 immune-cell killing and oxidative agent killing (**E4**).

1141  
1142 *E1 - Viral internalization.* Module E1 models extracellular virus binding to epithelial cell  
1143 receptors and internalization (including endocytosis-dependent and -independent routes).  
1144 Internalization of viral particles involves binding of the viral spike protein to target cell-  
1145 surface receptors, truncation by surface proteins and receptor-mediated endocytosis or  
1146 fusion with the host plasma membrane. We assume the dynamics of internalization can  
1147 be represented by describing the dynamics of virus-surface-receptor binding, determined  
1148 by the amount of extracellular virus and target surface receptors, and by the binding  
1149 affinity between them (**T1**→**E1**). We also consider the dynamic depletion of unbound  
1150 target surface receptors on a cell when it internalizes a virus and superinfection of infected  
1151 cells. Internalized viral particles initiate the viral replication process (**E1**→**E2** and Fig 2B).

1152  
1153 *E2 - Viral replication.* Module E2 models the viral replication cycle inside a host epithelial  
1154 cell (Fig 2B). Individual cells infected with many non-lytic viruses show a characteristic  
1155 three-phasic pattern in their rate of viral release. After infection and during an *eclipse*  
1156 *phase*, a cell accumulates but does not yet release newly assembled viruses. In a second  
1157 phase, the rate of viral release increases exponentially until the virus-releasing cell either  
1158 dies or, in a third phase, saturates its rate of virus synthesis and release. Viral replication

1159 hijacks host synthesis pathways and may be limited by the availability of resources (amino  
1160 acids, ATP, *etc.*), synthesis capability (ribosomes, endoplasmic reticulum, *etc.*) or  
1161 intracellular viral suppression. A quantitative model of viral replication needs to be  
1162 constructed and parameterized such that it reproduces these three phases.

1163 We model viral replication based on processes associated with positive sense  
1164 single-stranded RNA (+ssRNA) viruses. +ssRNA viruses initiate replication after  
1165 unpacking of the viral genetic material and proteins into the cytosol (**E1**→**E2**). The viral  
1166 RNA-dependent RNA polymerase transcribes a negative RNA strand from the positive  
1167 RNA strand, which is used as a template to produce more RNA strands (denoted by “Viral  
1168 Genome Replication” in Fig 2B). Replication of the viral genome is the only exponential  
1169 amplification step in the growth of most viruses within cells. Subgenomic sequences are  
1170 then translated to produce viral proteins (“Protein Synthesis” Fig 2B). Positive RNA  
1171 strands and viral proteins are transported to the endoplasmic reticulum (ER) where they  
1172 are packaged for release. After replication, newly synthesized viral genetic material is  
1173 translated into new capsid protein and assembled into new viral particles (“Assembly and  
1174 Packaging” in Fig 2B). These newly assembled viral particles initiate the viral release  
1175 process (**E2**→**E3**). We assume the viral replication cycle can be modeled by defining four  
1176 stages: unpacking, viral genome replication, protein synthesis, and assembly and  
1177 packaging. Fig 2B illustrates these subprocesses of replication and their relation to viral  
1178 internalization and release.

1179  
1180 *E3 - Viral release.* Module E3 models intracellular transport of newly assembled virions  
1181 and release into the extracellular environment (**E3**→**T1** and Fig 2B “Release”). We



1182 conceptualize the virus being released into the extracellular fluid above the apical  
1183 surfaces of epithelial cells. Newly assembled virions are packed into vesicles and  
1184 transported to the cell membrane for release into the extracellular environment (**E2**→**E3**).  
1185 We assume that no regulation occurs after assembly of new virus particles, and that  
1186 release into the extracellular environment can be modeled as a single-step process  
1187 (**E3**→**T1**).

1188

1189 *E4 - Cell death.* Module E4 models death of epithelial cells due to various mechanisms.  
1190 Models the combined effect of the many types of virus-induced cell death (*e.g.*, production  
1191 of viral proteins interferes with the host cell's metabolic, regulatory and delivery pathways)  
1192 as occurring due to a high number of assembled viral particles in the viral replication cycle  
1193 (**E2**→**E4**). Models cell death due to contact cytotoxicity (**I3**→**E4**). Models cell death due  
1194 to oxidizing cytotoxicity (**T3**→**E4**).

1195

1196 **Extracellular environment component.** The extracellular environment contains the  
1197 immune cells, extracellular virus, cytokines and oxidative agent, and is the space where  
1198 transport of viral particles (**T1**), cytokine molecules (**T2**) and the oxidizing agent (**T3**)  
1199 occurs. We implicitly model the ECM in the extracellular environment by subsuming its  
1200 geometrical, biochemical and biophysical influences on immune cell motility and  
1201 virus/cytokine/agent spreading in the chosen rate laws and parameter set. Immune cells  
1202 are mobile and can be either activated or inactive (**I1**). Inactive immune cells move  
1203 through random cell motility and activated immune cells chemotax along the cytokine field

1204 **(I2)**. The immune cell modules also account for cytotoxic effects of immune cells on  
1205 contact due to antigen recognition **(I3)** and through the secretion of oxidizing agents **(I4)**.

1206

1207 *T1 - Viral transport.* Module T1 models diffusion of viral particles in the extracellular  
1208 environment and their decay. Viral particles are transported by different mechanisms  
1209 (e.g., ciliated active transport, diffusion) and media (e.g., air, mucus) at different  
1210 physiological locations and through different types of tissue (e.g., nasopharyngeal track,  
1211 lung bronchi and alveoli). Viral particles are eliminated by a variety of biological  
1212 mechanisms. We represent these mechanisms by modeling transport of viral particles as  
1213 a diffusive virus field with decay in the extracellular environment. We model transport in  
1214 a thin layer above the apical surfaces of epithelial cells. Viral internalization results in the  
1215 transport of a finite amount of virus from the extracellular environment into a cell and  
1216 depends on the amount of local extracellular virus and number of cell surface receptors  
1217 **(T1-E1)**. Infected cells release viral particles into the extracellular environment as a result  
1218 of the viral replication cycle **(E3-T1)**.

1219

1220 *T2 - Cytokine transport.* Module T2 models diffusion and clearance of immune signaling  
1221 molecules in the extracellular environment. The immune response involves multiple  
1222 signaling molecules acting upon different signaling pathways. We assume that the  
1223 complexity of immune signaling can be functionally represented using a single chemical  
1224 field that diffuses and decays in the extracellular environment. Once infected, epithelial  
1225 cells secrete signaling molecules to alert the immune system **(E2-T2)**. Locally, exposure  
1226 to cytokine signaling results in activation of immune cells **(T2-I1)**. Upon activation,

1227 immune cells migrate towards infection sites guided by cytokine (**T2-I2**). Lastly, activated  
1228 immune cells amplify the immune signal by secreting additional cytokines into the  
1229 extracellular environment (**I1-T2**). We model long-range effects by assuming that cytokine  
1230 exfiltrates tissues and is transported to immune recruitment sites (**T2-L1**).

1231  
1232 *T3 - Oxidizing agent burst and transport.* Module T3 models diffusion and clearance of a  
1233 general oxidizing agent in the extracellular environment. One of the cytotoxic mechanisms  
1234 of immune cells is the release of different oxidizing agents, reactive oxygen species like  
1235 H<sub>2</sub>O<sub>2</sub> and nitric oxide. The mechanism of action of such agents varies but we assume that  
1236 we can generalize such effects by modeling a single diffusive and decaying oxidizing  
1237 agent field in the extracellular environment. The oxidizing agent is secreted by activated  
1238 immune cells after persistent exposure to cytokine signals (**I4→T3**). We assume that the  
1239 range of action of the oxidizing agent is short. Cell death is induced in uninfected, infected  
1240 and virus-releasing epithelial cells when sufficiently exposed to the oxidizing agent  
1241 (**T3→E4**).

1242  
1243 *I1 - Immune cell activation.* Module I1 models immune cell maturation due to cytokine  
1244 signaling. Immune cells mature at the recruitment site before being transported to the  
1245 infection site as inactive immune cells (**L1→Immune Cells**). After infiltration, immune  
1246 cells need to be exposed to local cytokine signals before activating (**T2→I1**). Once  
1247 activated, immune cells chemotax along the cytokine field (**I2**) and amplify immune  
1248 signaling by releasing cytokine molecules into the extracellular environment (**I1→T2**).  
1249 Immune cells can also deactivate after a period of activation (**I1** and Fig 2C).

1250

1251 *I2 - Immune cell chemotaxis.* Module I2 models activated immune cell chemotactic  
1252 migration towards infection sites. We assume that upon activation (**I1**→**I2**), immune cells  
1253 move preferentially towards higher concentrations of local cytokine (**T2**→**I2**).

1254

1255 *I3 - Immune cell direct cytotoxicity and bystander effect.* Module I3 models immune cell  
1256 cytotoxicity when immune cells (both activated and inactive) identify and induce death in  
1257 epithelial cells with internal virus. Immune cells identify epithelial cells with internal virus  
1258 on contact by antigen recognition and induce cell death by activating the caspase  
1259 cascade (**I3**→**E4**). Uninfected, infected, and virus-releasing epithelial cells in contact with  
1260 an epithelial cell that is killed by direct cytotoxicity can die through a bystander effect.

1261

1262 *I4 - Immune cell oxidizing agent cytotoxicity.* Module I4 models activated immune cell  
1263 killing of target cells through the release of a diffusive and decaying oxidizing agent into  
1264 the environment. Cell death is induced in uninfected, infected and virus-releasing  
1265 epithelial cells when sufficiently exposed to the oxidizing agent (**T3**→**E4**).

1266

1267 **Lymph node component.** The lymph node component models the net pro- or anti-  
1268 inflammatory state of the immune system. It responds to cytokines received from the  
1269 tissue and adds or removes immune cells from the tissue (**L1**).

1270

1271 *L1 - Immune cell recruitment.* Module L1 models immune cell recruitment and infiltration  
1272 into the tissue in response to cytokine signaling by infected cells and activated immune

1273 cells. Infected cells secrete signaling molecules into the extracellular environment  
1274 (**E2**→**T3**), which alerts resident immune cells and recruits new immune cells from the  
1275 blood, distant lymph nodes and bone marrow. We model the local strength of the cytokine  
1276 signal as causing an increase in the strength of the signal at the immune recruiting sites.  
1277 We model long-distance signaling by assuming that cytokine molecules in the  
1278 extracellular environment exfiltrate the infection site and are transported through the  
1279 lymphatic system to the lymphatic system to lymph nodes and through the bloodstream  
1280 to initiate immune-cell recruitment (**T2**→**L1**). A delay on the order of minutes to hours  
1281 would represent semi-local recruitment (e.g., at the blood vessels). A delay on the order  
1282 of days would represent long-range, systemic recruitment (e.g., the time required for a  
1283 dendritic cell to reach a lymph node and an induced T cell to return). Recruited immune  
1284 cells are then transported and infiltrate the infection site (**L1**→**Immune Cell**).

1285

## 1286 **Quantitative model and implementation**

1287 For model construction and integration we use the open-source multicellular  
1288 modeling environment CompuCell3D ([www.compuCell3d.org](http://www.compuCell3d.org)) which allows rapid and  
1289 compact specification of cells, diffusing fields and biochemical networks using Python and  
1290 the Antimony language [55,67]. CompuCell3D is specifically designed to separate model  
1291 specification (conceptual and quantitative models) from the details of model  
1292 implementation as a simulation and to make simulation specification accessible to  
1293 biologists and others not specializing in software development. In this paper, we  
1294 specifically designed the Python modules and their cross-scale integration to have clear  
1295 and stable APIs, allowing modules to be rapidly swapped out by collaborating developers.

1296 CompuCell3D runs on Windows, Mac and Linux platforms without change of model  
1297 specification, and allows cluster execution for parameter exploration.

1298

1299 **Cellular Potts model (CPM).** *Cell types.* Cells are divided into two broad groups,  
1300 epithelial and immune cells, and have a *type* (see Fig 2C) which determines their  
1301 properties, the processes and interactions in which they participate, and their events and  
1302 dynamics. Epithelial cells can have one of four types (uninfected, infected, virus releasing  
1303 and dead). Immune cells can have one of two types (activated and inactive). Cell types  
1304 can change according to outcomes of various modules, and a module specifying such an  
1305 event describes both the initial and final cell types of the transition. A cell type in the model  
1306 is not a phenotype in the biological sense (*e.g.*, *epithelial cell*), but an identifier for the  
1307 various states that a particular cell can assume (*e.g.*, *dead epithelial cell*). When an  
1308 epithelial cell changes to the dead type, all epithelial modules are disabled and the cell is  
1309 generally inactive.

1310

1311 *Cellular dynamics.* Cellular spatial dynamics is modeled using the Cellular Potts model  
1312 (also known as *CPM*, or Glazier-Graner-Hogeweg model), which represents generalized  
1313 cells and medium as occupying a set of sites in a lattice [68]. Random cell motility is  
1314 modeled as the stochastic exchange of sites at intercellular and cell-medium interfaces.  
1315 Configurations evolve to minimize the system's effective energy  $\mathcal{H}$ ,

$$\begin{aligned}
 \mathcal{H} = & \sum_{\sigma} \lambda_{volume} \left( v(\sigma) - V(\tau(\sigma)) \right)^2 \\
 & + \sum_x \sum_{x' \in N(x)} (1 - \delta_{\sigma(x), \sigma(x')}) J(\tau(\sigma(x)), \tau(\sigma(x'))) \\
 & + \mathcal{H}_{chemotaxis}.
 \end{aligned} \tag{1}$$

1316 Here  $\sigma$  is the integer identification of a cell and  $\tau(\sigma)$  is the type of cell  $\sigma$ .  $v(\sigma)$  and  $V(\sigma)$   
 1317 are the current and target volumes of cell  $\sigma$ , respectively, and  $\lambda_{volume}$  is a volume  
 1318 constraint coefficient.  $N(x)$  is the neighborhood of site  $x$ ,  $\delta_{i,j}$  is the Kronecker-delta, and  
 1319  $J(\tau, \tau')$  is the effective contact energy per unit surface area between cells of types  $\tau$  and  
 1320  $\tau'$ . The final term,  $\mathcal{H}_{chemotaxis}$ , models chemotaxis-directed cell motility, and is prescribed  
 1321 by module I2. The cell configuration evolves through asynchronous lattice-site copy  
 1322 attempts. A lattice-site copy attempt starts by random selection of a site  $x$  in the lattice as  
 1323 a target, and a site  $x'$  in its neighborhood as a source. A configuration update is then  
 1324 proposed in which the value  $x'$  from the source site overwrites the value of  $x$  in the target  
 1325 site. The change in total effective energy  $\Delta\mathcal{H}$  due to the copy attempt is calculated, and  
 1326 the update is executed with a probability given by a Boltzmann acceptance function,

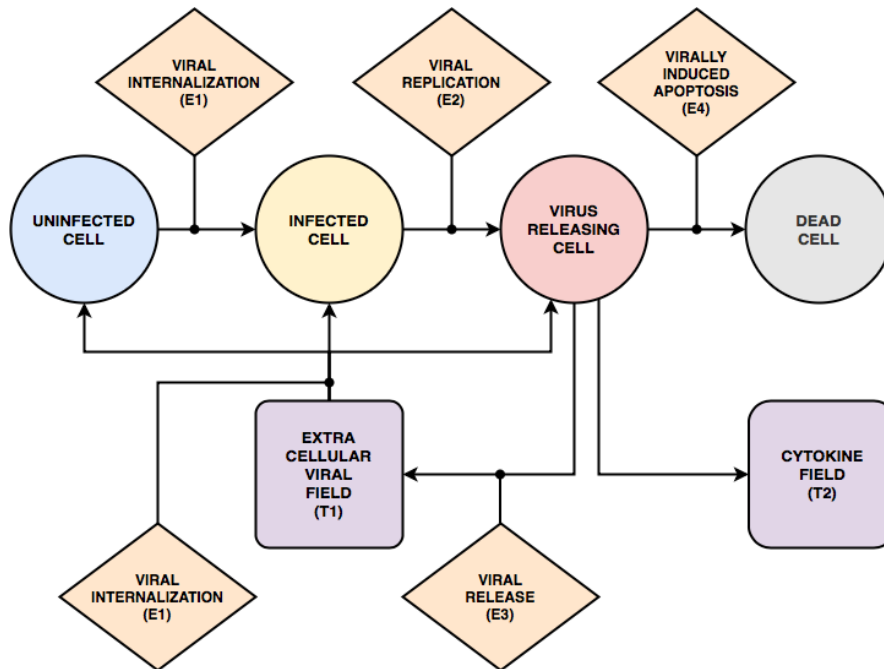
$$\Pr(\sigma(x) \rightarrow \sigma(x')) = e^{-\max\{0, \frac{\Delta\mathcal{H}}{\mathcal{H}^*}\}}. \tag{2}$$

1327 Here the intrinsic random motility  $\mathcal{H}^*$  controls the stochasticity of accepted copy attempts.  
 1328 Updates that reduce the system's effective energy are always accepted. The unit of  
 1329 simulation time is the Monte Carlo step (MCS)—taken to be 20 minutes in this work. One  
 1330 MCS corresponds to considering a number of copy attempts equal to the number of lattice  
 1331 sites.

1332



1333 **Epithelial component modules.** Processes **E1-E4** describe epithelial cell functions as  
1334 defined below. **E1**, **E2** and **E4** govern the cell-type transitions of epithelial cells (see Fig  
1335 15). **E1** transforms an uninfected epithelial cell into an infected epithelial cell. **E2**  
1336 transforms an infected epithelial cell into a virus-releasing epithelial cell. **E4** transforms  
1337 a virus-releasing epithelial cell into a dead cell.  
1338



1339  
1340 **Fig 15. State diagram and interactions of epithelial cells.**  
1341 Epithelial cells can have one of four “cell types”: uninfected, infected, virus-releasing and dead. Uninfected cells become  
1342 infected cells when the viral uptake model (**E1**) internalizes viruses from the extracellular virus field (**T1**). Infected cells  
1343 continue internalizing viruses from the extracellular virus field and become virus-releasing cells when the viral  
1344 replication model (**E2**) produces sufficient newly assembled virions. Virus-releasing cells secrete viruses into the  
1345 extracellular virus field (**T1**) according to the viral release module (**E3**) and secrete cytokines directly into the  
1346 extracellular cytokine field (**T2**). Virus-releasing cells can die if the conditions of the virally induced cell-death model  
1347 (**E4**) are met.  
1348

1349 *E1 - Viral internalization.* To capture the stochasticity associated with internalization of  
 1350 discrete virus particles in terms of discrete binding events, we assign each uninfected,  
 1351 infected and virus-releasing epithelial cell a probability of absorbing diffusive viral particles  
 1352 from the extracellular virus field (**T1**). The uptake probability  $\Pr(Uptake(\sigma) > 0)$  for each  
 1353 cell  $\sigma$  is given by a Hill equation of the total amount of diffusive viral particles in the domain  
 1354 of the cell  $c_{vir}(\sigma)$ , the number of unbound cell surface receptors  $SR(\sigma)$  and the binding  
 1355 affinity between them.

$$\Pr(Uptake(\sigma) > 0) = \frac{\Delta t}{\alpha_{upt}} \frac{(c_{vir}(\sigma))^{h_{upt}}}{(c_{vir}(\sigma))^{h_{upt}} + V_{upt}}, \text{ where } V_{upt} = \frac{R_o k_{off}}{2k_{on} v(\sigma) SR(\sigma)}. \quad (3)$$

1356 Here  $h_{upt}$  is a Hill coefficient,  $R_o$  is the cell's initial number of unbound receptors,  $k_{on}$  is  
 1357 the virus-receptor association affinity,  $k_{off}$  is the virus-receptor dissociation affinity,  $\alpha_{upt}$   
 1358 is a characteristic time constant of uptake and  $\Delta t$  is the time represented by one MCS. At  
 1359 each simulation time step, the uptake probability is evaluated against a uniformly-  
 1360 distributed random variable. When uptake occurs, the uptake rate is proportional to the  
 1361 local amount in the virus field (**T1**), and the probability of uptake is used to define the  
 1362 amount (*Uptake*) of virus taken up during the MCS,

$$Uptake(\sigma) = \frac{1}{\Delta t} \Pr(Uptake(\sigma) > 0) c_{vir}(\sigma), \quad (4)$$

$$\frac{dSR(\sigma)}{dt} = -Uptake(\sigma). \quad (5)$$

1363 The amount absorbed by each cell (*Uptake*) is uniformly subtracted from the virus field  
 1364 over the cell's domain and the cell's number of cell surface receptors is reduced by the  
 1365 same amount. The amount of virus taken up (*Uptake*) is also passed to the cell's instance

1366 of the viral replication model (**E2**). Infected epithelial cells continue taking up viral particles  
1367 from the environment until their cell surface receptors are depleted.

1368

1369 *E2 - Viral replication*. Our viral replication model combines equations and parameters  
1370 from several sources to represent the replication of a generic virus [7,9,52,53]. The model  
1371 contains four variables representing viral quantities in different states of the viral  
1372 replication process: internalized virus  $U$  (Equation (6), the process of unpacking), viral  
1373 genome taking part in genomic replication  $R$  (Equation (7), the process of viral genome  
1374 replication), synthesized protein  $P$  (Equation (8), the process of protein synthesis), and  
1375 assembled and packaged virions  $A$  (Equation (9), the process of assembly and  
1376 packaging). Biologically, the only process which can exponentially increase the rate of  
1377 virus production by a single cell is viral genome replication, so the equations include the  
1378 positive feedback by  $R$  in Equation (7). Biologically, factors like the cell's metabolism,  
1379 limited number of ribosomes, maximum rate of endoplasmic reticulum function and  
1380 activation of intracellular viral suppression pathways all limit production of viral  
1381 components, so we include a Michaelis-type saturation term for the rate of replication in  
1382 Equation (7). Each uninfected, infected and virus-releasing cell in the simulation contains  
1383 an independent copy of the system of ordinary differential equations modeling the viral  
1384 replication process,

$$\frac{dU}{dt} = U_{\text{uptake}} - r_u U, \quad (6)$$

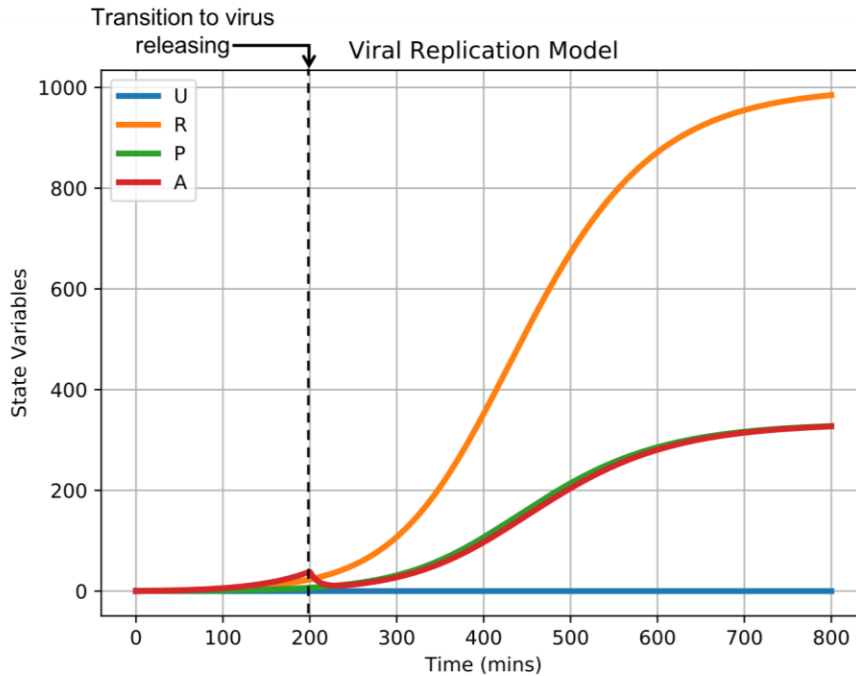
$$\frac{dR}{dt} = r_u U + r_{\text{max}} R \frac{r_{\text{half}}}{R + r_{\text{half}}} - r_t R, \quad (7)$$

$$\frac{dP}{dt} = r_t R - r_p P, \quad (8)$$

$$\frac{dA}{dt} = r_p P - \text{Release}. \quad (9)$$

1385 Here  $r_u$  is the unpacking rate,  $r_{max}$  is the viral replication rate,  $r_t$  is the translating rate  
1386 (rate at which viral genomes turn into RNA templates for protein production) and  $r_p$  is the  
1387 packaging rate. *Uptake* is defined in **E1** and *Release* is defined in **E3**. The saturation of  
1388 the rate of viral genome replication is represented by a Michaelis-Menten function,  $\frac{r_{half}}{R + r_{half}}$ ,  
1389 where  $r_{half}$  is the amount of  $R$  at which the viral genome replication rate is reduced to  
1390  $\frac{r_{max}}{2}$  (and the flux is reduced to  $\frac{1}{2} r_{max} r_{half}$ ). The duration of the eclipse phase of single-  
1391 cell infection (the time between the first entry of the virus into the cell and the first release  
1392 of newly synthesized virus) is approximately  $t_{eclipse} \approx \frac{1}{r_u} + \frac{1}{r_{max}} + \frac{1}{r_t} + \frac{1}{r_p}$  (11.7 hours for  
1393 the reference parameter set in Table 1), with the additional complication that in our model,  
1394 an epithelial cell does not release virus until  $A$  reaches a threshold value. The timescale  
1395 for tenfold increase of virus release when viral replication is maximal is  $t_{10} \approx \frac{\log(10)}{r_{max}}$  (7.7  
1396 hours for the reference parameter set in Table 1). The number of newly assembled virions  
1397 is passed to the cell's instance of the viral release module (**E3**). See Fig 2B for a  
1398 schematic of the viral replication process and Fig 16 for a representative time series from  
1399 the viral internalization, replication and release modules.

1400



1401

1402 **Fig 16. Representative time series of viral internalization, replication and release models from Fig 2B.**

1403 A sample simulation of the viral replication model in a single epithelial cell. The model is initialized with one unit of  
 1404 internalized virus ( $U = 1$ ), and the rest of the state variables set to zero ( $R = 0$ ,  $P = 0$ ,  $A = 0$ ). No additional virus  
 1405 internalization occurs during this sample simulation. Dashed line indicates the time of the cell's transition from the  
 1406 infected to virus-releasing cell type.

1407

1408 *E3 - Viral release.* Virus releasing cells release viral particles into the extracellular virus  
 1409 field (**T1**). The amount of virus released by a cell per unit time is proportional to the state  
 1410 variable for assembled virions in the viral replication module (**E2**),

$$Release = r_s A. \quad (10)$$

1411 Here  $r_s$  is the release rate of viral particles and  $A$  is the level of assembled virus in the cell  
 1412 (defined in **E2**). The total amount released by each cell  $r_s A \Delta t$  is subtracted from the cell's  
 1413 state variable for assembled virions  $A$  and passed to the source term of the extracellular  
 1414 virus field (**T1**) to maintain mass balance.

1415

1416 *E4 - Cell death.* For cell death due to virally-induced apoptosis, each infected and virus-  
1417 releasing cell can die due to the amount of intracellular virus. The rate of death is defined  
1418 as a stochastic function of the state variable for assembled new virions from the viral  
1419 replication module (**E2**). If a virus releasing cell dies then it changes its cell type to dead  
1420 and the cell's instances of the viral internalization, replication and release modules are  
1421 disabled. The probability of virus-induced apoptosis per simulation step is a Hill equation  
1422 of the current load of assembled virus,

$$\Pr(\tau(\sigma) \rightarrow \text{Dead} | \tau(\sigma) = \text{Virus releasing}) = \frac{\Delta t}{\alpha_{apo}} \frac{(A(\sigma))^{h_{apo}}}{(A(\sigma))^{h_{apo}} + V_{apo}^{h_{apo}}}. \quad (11)$$

1423 where  $A(\sigma)$  is the number of assembled virions in cell  $\sigma$ ,  $h_{apo}$  is a Hill coefficient,  $V_{apo}$  is  
1424 the amount of assembled virions at which the apoptosis probability is 0.5 per unit time  
1425 and  $\alpha_{apo}$  is a characteristic time constant of virally-induced apoptosis. For modeling of  
1426 cell death due to contact cytotoxicity, see *13 - Immune cell direct cytotoxicity and*  
1427 *bystander effect*. For modeling of cell death due to oxidizing cytotoxicity, see *14 - Immune*  
1428 *cell oxidizing agent cytotoxicity*. Regardless of the death mechanism the internally  
1429 assembled virions are not released to the environment and do not take action in further  
1430 infection. We assume that in the process of death the assembled virus and viral particles  
1431 are either damaged or deactivated.

1432

1433 **Lymph node modules.** *L1 - Immune cell recruitment.* The total immune cell population  
1434 is governed by an ordinary differential equation of a dimensionless state variable  $S$  that  
1435 represents immune response due to local conditions and long-distance signaling. Our



1436 convention is that when  $S > 0$ , immune cells are recruited to the simulation domain;  
1437 likewise, immune cells are removed from the simulation domain when  $S < 0$ . Probability  
1438 functions of  $S$  describe the likelihood of immune cell seeding and removal,

$$\Pr(\text{add immune cell}) = \text{erf}(\alpha_{\text{immune}}S), \quad S > 0, \quad (12)$$

$$\Pr(\text{remove immune cell}) = \text{erf}(-\alpha_{\text{immune}}S), \quad S < 0. \quad (13)$$

1439 Here the coefficient  $\alpha_{\text{immune}}$  is the sensitivity of immune cell addition and removal to the  
1440 state variable  $S$ . The dynamics of  $S$  are cast such that, in a homeostatic condition, a typical  
1441 number of immune cells can be found in the simulation domain, and production of cytokine  
1442 (**T2**) results in additional recruitment via long-distance signaling (*i.e.*, with some delay).  
1443 We model this homeostatic feature using the feedback mechanism of the total number of  
1444 immune cells  $N_{\text{immune}}$  in the simulation domain. Cytokine signaling is modeled as  
1445 perturbing the homeostatic state using the term  $\alpha_{\text{sig}}\delta$ . Here  $\delta$  is the total amount of  
1446 decayed cytokine in the simulation domain and  $\alpha_{\text{sig}} > 0$  models signaling by transmission  
1447 of cytokine to some far-away source of immune cells. We write the rate of change of  $S$  as

$$\frac{dS}{dt} = \beta_{\text{add}} - \beta_{\text{sub}}N_{\text{immune}} + \frac{\alpha_{\text{sig}}}{\beta_{\text{delay}}}\delta - \beta_{\text{decay}}S. \quad (14)$$

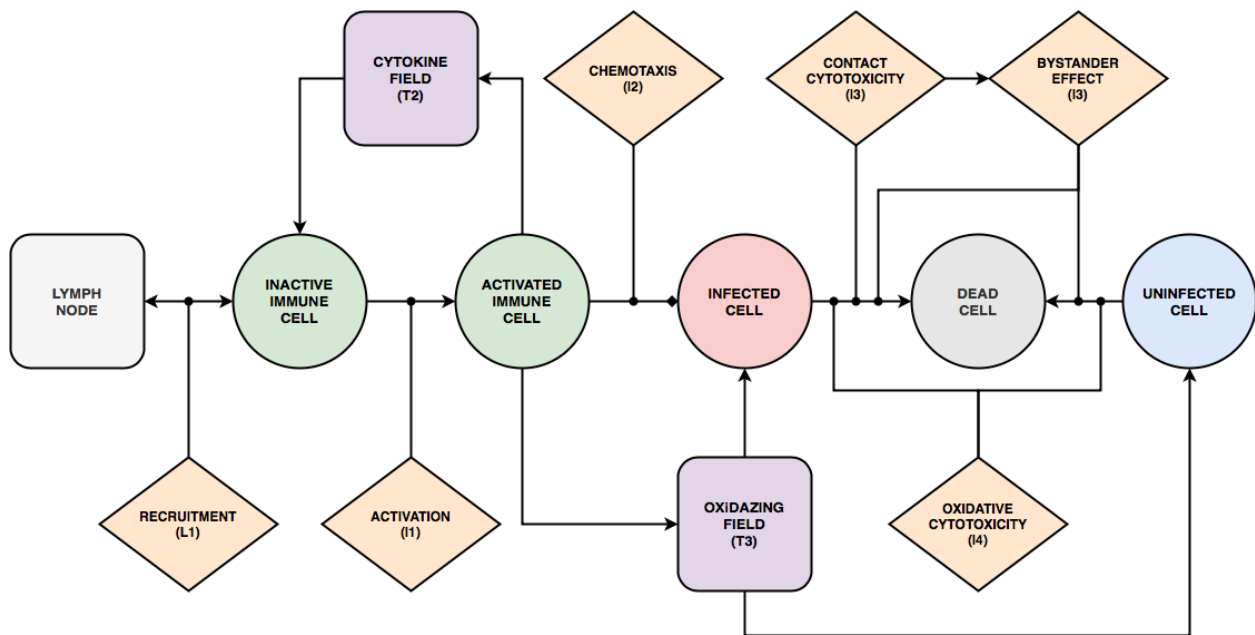
1448 Here  $\beta_{\text{add}}$  and  $\beta_{\text{sub}}$  control the number of immune cells in the simulation domain under  
1449 homeostatic conditions.  $\beta_{\text{delay}}$  controls the delay between transmission of the cytokine to  
1450 the lymph node and corresponding immune response by adjusting the rate of recruitment  
1451 due to total cytokine (*i.e.*, increasing  $\beta_{\text{delay}}$  increases the resulting delay).  $\beta_{\text{decay}}$  regulates  
1452 the return of  $S$  to an unperturbed state (*i.e.*,  $S = 0$ , increasing  $\beta_{\text{decay}}$  increases the rate of  
1453 return to  $S = 0$ ). To determine the seeding location, the simulation space is randomly  
1454 sampled  $n_{\text{seeding}}$  times, and an immune cell is seeded at the unoccupied location with the

1455 highest amount of the virus field. If no location is unoccupied, then the immune cell is not  
 1456 seeded. The removal probability is evaluated for each immune cell at each simulation  
 1457 step. Immune cells are removed by setting their volume constraint to zero.

1458

1459 **Immune cell modules.** The four processes **I1-I4** capture immune cell functions which  
 1460 are defined below. These processes control how immune cells are activated,  
 1461 translocate, and kill other cells. Their interactions with epithelial cells and other model  
 1462 components are illustrated in Fig 17.

1463



1464

1465 **Fig 17. State diagram and interactions of Immune cells.**

1466 Immune cells can adopt two different generalized types: inactive and activated. Inactive immune cells are recruited by  
 1467 the cytokine levels according to the immune recruitment module (**L1**). Transition from inactive to activated immune cells  
 1468 is determined by the immune activation module (**I1**) when cells are exposed to cytokines in the tissue. Activated immune  
 1469 cells amplify the cytokine signal by secreting cytokines to the extracellular environment. Activated immune cells  
 1470 chemotax towards virus-releasing cells (**I2**). Immune cells induce death of epithelial cells by direct cytotoxicity when

1471 coming into contact with infected cells (**I3**), bystander effect by killing neighbors of infected cells (**I3**) and through  
 1472 oxidative cytotoxicity (**I4**) by releasing cytotoxic oxidizing agents (**T3**) into the extracellular environment.

1473

1474 *I1 - Immune cell activation.* Inactive immune cells become activated with a probability  
 1475 according to a Hill equation of the total cytokine bound to the cell  $B_{cyt}(\sigma, t)$ ,

$$\Pr(\tau(\sigma, t) \rightarrow \text{activated immune} | \tau(\sigma, t) = \text{inactive immune}) = \frac{(B_{cyt}(\sigma, t))^{h_{act}}}{(B_{cyt}(\sigma, t))^{h_{act}} + (EC50_{cytact})^{h_{act}}}. \quad (15)$$

1476 After ten hours, an activated immune cell becomes inactive, in which case evaluations of  
 1477 activation (Equation (15)) recommence. The immune cells “forget” a percentage  $(1 - \rho_{cyt})$   
 1478 of the bound cytokine each time step while taking up an amount of cytokine from the  
 1479 environment ( $\omega_{cyt}(\tau(\sigma), t)$  defined in **T2**),

$$B_{cyt}(\sigma, t) = \rho_{cyt} B_{cyt}(\sigma, t - \Delta t) + \omega_{cyt}(\tau(\sigma(x)), t). \quad (16)$$

1480

1481 *I2 - Immune cell chemotaxis.* Activated immune cells experience a motile force as a  
 1482 response to a signaling field. Immune cells chemotax along concentration gradients of  
 1483 the cytokine field. The chemotactic effective energy  $\mathcal{H}_{chemotaxis}$  associated with the  
 1484 gradient is calculated according to a chemotactic sensitivity parameter  $\lambda_{chemotaxis}$  and  
 1485 calculated chemotactic force  $F_{chemotaxis}$ . The contribution of  $\mathcal{H}_{chemotaxis}$  to the change in  
 1486 the system’s total effective energy is calculated using  $F_{chemotaxis}$  when considering copy  
 1487 attempts. The chemotactic force at a location  $x$  is saturated by normalizing the  
 1488 chemotactic sensitivity parameter by the concentration of cytokine at the center of mass  
 1489 of the cell at  $x$ ,  $c_{cyt,CM}(\sigma(x))$ ,

$$F_{chemotaxis}(x) = \frac{\lambda_{chemotaxis}}{1 + c_{cyt,CM}(\sigma(x))} \nabla c_{cyt}(x). \quad (17)$$

1490

1491 *I3 - Immune cell direct cytotoxicity and bystander effect.* Immune cells, whether activated  
 1492 or not, have the ability to kill infected cells by direct contact. At each simulation step,  
 1493 immune cells trigger cell death in the infected and virus-releasing epithelial cells with  
 1494 which they come in contact. When an infected cell is killed by direct cytotoxicity, each of  
 1495 its first-order neighbors is evaluated for cell death by a bystander effect model. Each of  
 1496 those neighbors  $\sigma' \in N(\sigma)$  in the first-order neighborhood  $N(\sigma)$  of a cell  $\sigma$  killed by direct  
 1497 cytotoxicity has a probability  $k_{bystander}$  of dying from the bystander effect given by,

$$\Pr(\tau(\sigma', t) \rightarrow \text{Dead} | \text{Direct Cytotoxicity}(\sigma) = \text{True}) = k_{bystander} \forall \sigma' \in N(\sigma). \quad (18)$$

1498

1499 *I4 - Immune cell oxidizing agent cytotoxicity.* Immune cells release a short-range, diffusive  
 1500 oxidizing agent when exposed to high cytokine concentration (**T3**). The oxidizing agent  
 1501 kills an epithelial cell of any type when the total amount of oxidizing agent in the domain  
 1502 of the cell  $c_{oxi}(\sigma)$  exceeds a threshold for death  $\tau_{oxi}^{death}$ ,

$$\Pr(\tau(\sigma, t) \rightarrow \text{Dead} | c_{oxi}(\sigma) > \tau_{oxi}^{death}) = 1. \quad (19)$$

1503

1504 **Extracellular environment modules.** *T1 - Viral transport.* The change in concentration  
 1505 of the virus field  $c_{vir}$  is calculated at each location in the simulation domain by solving the  
 1506 following reaction-diffusion equation,

$$\frac{\partial c_{vir}(x)}{\partial t} = D_{vir} \nabla^2 c_{vir}(x) - \gamma_{vir} c_{vir}(x) + \frac{1}{v(\sigma(x))} (\text{Release}(\sigma(x)) - \text{Uptake}(\sigma(x))). \quad (20)$$

1507 Here  $D_{vir}$  is the diffusion constant of the extracellular virus and  $\gamma_{vir}$  is the decay rate is  
 1508 the decay rate. Uptake and release by a cell at each location are determined using the  
 1509 viral internalization (**E1**) and the viral release (**E3**) modules, and are uniformly applied  
 1510 over all sites of the domain of the cell.

1511

1512 *T2 - Cytokine transport.* The change in concentration of the cytokine field  $c_{cyt}$  is obtained  
 1513 by solving a reaction-diffusion equation of the following general form,

$$\frac{\partial c_{cyt}}{\partial t} = D_{cyt} \nabla^2 c_{cyt} - \gamma_{cyt} c_{cyt} + s_{cyt}. \quad (21)$$

1514 The decay term  $\gamma_{cyt} c_{cyt}$  represents cytokine leaving the simulation domain (e.g., in  
 1515 immune recruitment). To model immune signaling, the rate of cytokine secretion is  
 1516 described by an increasing Hill function of  $c_{sig}(\sigma(x))$  with Hill exponent  $h_{cyt} = 2$ . The  
 1517 meaning of  $c_{sig}(\sigma(x))$  depends on the cell type and the Hill exponent can differ for other  
 1518 cell types and states. The rate of cytokine secretion  $s_{cyt}$  is written as,

$$s_{cyt}(x, t) = \sigma_{cyt}(\tau(\sigma(x), t)) \frac{(c_{sig}(\sigma(x), t))^{h_{cyt}}}{(c_{sig}(\sigma(x), t))^{h_{cyt}} + (V_{cyt}(\tau(\sigma(x), t)))^{h_{cyt}}} - \omega_{cyt}(\tau(\sigma(x), t)). \quad (22)$$

1519 Here  $\sigma_{cyt}(\tau(\sigma(x), t))$  is the maximum cytokine secretion rate for the cell type at  $x$ ,  
 1520  $c_{sig}(\sigma(x))$  is a quantity that affects the cells cytokine secretion,  $\omega_{cyt}(\tau(\sigma(x), t))$  is the  
 1521 cytokine uptake rate of the cell type at  $x$  and  $V_{cyt}(\tau(\sigma(x), t))$  is a dissociation coefficient  
 1522 of cytokine secretion for the cell type at  $x$ .  $\sigma_{cyt}$  is nonzero for infected epithelial cells,  
 1523 virus-releasing epithelial cells and activated immune cells. For infected and virus-  
 1524 releasing epithelial cells  $c_{sig}$  is the amount of assembled virus  $A$  in the viral replication  
 1525 module, and for activated immune cells  $c_{sig}$  is the total amount of cytokine in the domain

1526 of the cell. Similarly, for epithelial cells  $V_{cyt}$  is the amount of assembled virus, and for  
1527 immune cells  $V_{cyt}$  is the amount of cytokine in the domain of the cell.  $\omega_{cyt}(\tau(\sigma(x), t))$  is  
1528 constant and nonzero for activated and inactive immune cells.

1529

1530 *T3 - Oxidizing agent transport.* The oxidizing agent field diffuses according to the reaction-  
1531 diffusion equation,

$$\frac{\partial c_{oxi}}{\partial t} = D_{oxi} \nabla^2 c_{oxi} - \gamma_{oxi} c_{oxi} + s_{oxi}. \quad (23)$$

1532 Bursts of oxidizing agent are implemented as a source term for one time step according  
1533 to a rate coefficient  $\sigma_{oxi}$ , which is uniformly mapped onto the source term  $s_{oxi}$  over the  
1534 domain of each activated immune cell. An oxidizing burst occurs in immune cells with an  
1535 activated state when the total cytokine in the immune cell's domain exceeds a threshold  
1536  $\tau_{oxi}^{sec}$ .

1537

1538 **Initial and boundary conditions.** The domain of all simulations had dimensions of 90 x  
1539 90 x 2 lattice sites. The initial cell configuration consisted of a 30 x 30 sheet of uninfected  
1540 epithelial cells, each of size 3 x 3, on the lower layer of lattice sites (see Fig S23 for a  
1541 demonstration of the negligible effects of a non-uniform arrangement of epithelial cells).  
1542 Epithelial cells were “frozen”, in that they were immobile, leaving the remaining 90 x 90  
1543 subdomain for occupancy by recruited immune cells. For cellular dynamics and mass  
1544 transport, periodic boundary conditions were applied in the plane of the epithelial sheet,  
1545 and Neumann conditions were applied along the direction orthogonal to the epithelial  
1546 sheet. All field solutions for the diffusive viral, cytokine and oxidizing agent fields were  
1547 initialized as zero everywhere.



1548 At each first simulation step, the epithelial cell in the center of the sheet was set to  
1549 infected, and the amount of internalized virus  $U$  of the viral replication model was set to a  
1550 value of one. All epithelial cells were initialized with a number of unbound surface  
1551 receptors  $SR = R_o$ . All immune cells, when introduced to the simulation by recruitment,  
1552 were initialized in an inactive state, and with a bound cytokine value equal to zero ( $B_{cyt} =$   
1553 0). During transition of an uninfected epithelial cell to the infected type, all state variables  
1554 of the viral replication model were initialized with a value of zero.

1555

1556 **Simulation specifications.** Model implementation and all simulations were performed  
1557 using CompuCell3D, which uses a non-dimensional lattice for CPM-based cellular  
1558 dynamics and non-dimensional explicit time integration of reaction-diffusion field  
1559 solutions. As such, a baseline parameter set was constructed for all CPM parameters and  
1560 modules developed in this work (Table 1). Non-dimensionalization was performed on  
1561 model parameters for a lattice dimension of 4  $\mu\text{m}$  per pixel along each dimension, at 20  
1562 minutes (1/3 hours) per MCS. All replicas were simulated for ten trials, each 1,000 MCS  
1563 (20000 minutes, 333 hours, 14 days) long. Simulation data was collected at a frequency  
1564 of 10 MCSs (200 minutes, 3 hours) for all simulations.

1565

1566 **Table 1. Parameter values in baseline parameter set.**

Conversion Factors	Value	References / Justification
Simulation step $\Delta t$	1200.0 s	Selected for approximately 14 days of simulation time in 1k simulation steps
Lattice width	4.0 $\mu\text{m}$	Selected according to cell diameter
Scale factor for concentration	$1 \times 10^{-14}$ mol	Selected for conversion from $\text{mol L}^{-1}$ to $\text{mol } \mu\text{m}^{-1}$ ( $10^{-15}$ ) with 10x adjustment for fewer concentrations less than 1

Simulation parameters	Value	References / Justification
Cell diameter	12.0 $\mu\text{m}$	Selected according to typical epithelial cell size
Replication rate $r_{max}$	$(1/12)\times 10^{-3} \text{ s}^{-1}$	Calibrated to timescale of SARS-CoV-2 [56]
Translating rate $r_t$	$(1/18)\times 10^{-3} \text{ s}^{-1}$	Calibrated to timescale of SARS-CoV-2 [56]
Unpacking rate $r_u$	$(1/6)\times 10^{-3} \text{ s}^{-1}$	Calibrated to timescale of SARS-CoV-2 [56]
Packaging rate $r_p$	$(1/6)\times 10^{-3} \text{ s}^{-1}$	Calibrated to timescale of SARS-CoV-2 [56]
Release rate $r_s$	$(1/6)\times 10^{-3} \text{ s}^{-1}$	Calibrated to timescale of SARS-CoV-2 [56]
Scale factor for number of mRNA per infected cell $mRNA_{avg}$	1000 cell <sup>-1</sup>	Selected for average production of 2000 virions per cell before death per influenza [75]
Viral dissociation coefficient $r_{half}$	2000	Derived from $mRNA_{avg}$ , $r_{max}$ and $r_t$
Viral diffusion coefficient $D_{vir}$	0.01 $\mu\text{m}^2 \text{ s}^{-1}$	Selected according to sensitivity analysis and estimated from physiological ranges for lung mucus <sup>1</sup>
Viral diffusion length $\lambda_{vir}$	36 $\mu\text{m}$	Selected according to sensitivity analysis
Viral decay rate $\gamma_{vir}$	$7.71\times 10^{-6} \text{ s}^{-1}$	Derived from $\lambda_{vir}$ and $D_{vir}$
Cytokine diffusion coefficient $D_{cyt}$	0.16 $\mu\text{m}^2 \text{ s}^{-1}$	[69,70] (IL-2 cytokine)
Cytokine diffusion length $\lambda_{cyt}$	100 $\mu\text{m}$	[69] (IL-2 cytokine)
Cytokine decay rate $\gamma_{cyt}$	$1.32\times 10^{-5} \text{ s}^{-1}$	Derived from $\lambda_{cyt}$ and $D_{cyt}$
Maximum cytokine immune secretion rate $\sigma_{cyt}(immune\ activated)$	$3.5\times 10^{-4} \text{ pM s}^{-1}$	Estimated as 1/10 of $\sigma_{cyt}(infected)$
Immune secretion midpoint $V_{cyt}(immune\ activated)$	1 pM	[70]
Cytokine immune uptake rate $\omega_{cyt}(immune\ activated)$	$3.5\times 10^{-4} \text{ pM s}^{-1}$	[69]
Maximum cytokine infected cell secretion rate $\sigma_{cyt}(infected)$	$3.5\times 10^{-3} \text{ pM s}^{-1}$	[69]
Infected cell cytokine secretion mid-point $V_{cyt}(infected)$ , $V_{cyt}(virus\ releasing)$	0.1	Chosen from typical simulation values of assembled virus. Values stay around 0.1 and increase as infection progresses
Cytokine secretion Hill coefficient $h_{cyt}$	2	Selected for simplest form with inflection of model response
Immune cell cytokine activation $EC50_{cyt,act}$	10 pM	[69]
Immune cell equilibrium bound cytokine $EQ_{ck}$	210 pM	Chosen to be $2.1 \times EC50_{cyt,act}$
Immune cell bound cytokine memory $\rho_{cyt}$	$0.99998 \text{ s}^{-1}$	Derived from $\omega_{cyt}(immune\ activated)$ and $EQ_{ck}$
Immune cell activated time	10 h	[71]

Oxidation Agent diffusion coefficient $D_{oxi}$	$0.64 \mu\text{m}^2 \text{s}^{-1}$	Selected to be $4 \times D_{cyl}$ to model high diffusivity relative to IL-2
Oxidation Agent diffusion length $\lambda_{oxi}$	$36 \mu\text{m}$	Selected to be 3 cell diameters to model high reactivity
Oxidation Agent decay rate $\gamma_{oxi}$	$1.32 \times 10^{-5} \text{s}^{-1}$	Derived from $\lambda_{oxi}$ and $D_{oxi}$
Immune cell oxidation agent secretion rate $\sigma_{oxi}$	$3.5 \times 10^{-3} \text{pM s}^{-1}$	Selected to be the same as $\sigma_{cyl}(\text{infected})$
Immune cell $C_{cyl}$ threshold for Oxidation Agent release $\tau_{oxi}^{sec}$	10 A.U. = 1.5625 pM	Selected according to sensitivity analysis
Tissue cell $C_{oxi}$ threshold for death $\tau_{oxi}^{death}$	1.5 A.U. = 0.234375 pM	Selected according to sensitivity analysis
Initial density of unbound cell surface receptors $R_o$	$200 \text{cell}^{-1}$	Selected for potential limiting factor (availability of receptors) from typical simulation extracellular virus field values
Virus-receptor association affinity $k_{on}$	$1.4 \times 10^4 \text{M}^{-1} \text{s}^{-1}$	[72,73]
Virus-receptor dissociation affinity $k_{off}$	$1.4 \times 10^{-4} \text{s}^{-1}$	[72,73]
Infection threshold	1	Calibrated to timescale of SARS-CoV-2 [56]
Uptake Hill coefficient $h_{upt}$	2	Selected for simplest form with inflection of model response
Uptake characteristic time constant $\alpha_{upt}$	20 min	Selected to be the same as $\Delta t$
Virally-induced apoptosis Hill coefficient $h_{apo}$	2	Selected for simplest form with inflection of model response
Virally-induced apoptosis dissociation coefficient $V_{apo}$	100	Selected according to sensitivity analysis
Virally-induced apoptosis characteristic time constant $\alpha_{apo}$	20 min	Selected to be the same as $\Delta t$
Immune cell activation Hill coefficient $h_{act}$	2	Selected for simplest form with inflection of model response
Immune response add immune cell coefficient $\beta_{add}$	$1/1200 \text{s}^{-1}$	Selected for sensitivity analysis of $\beta_{delay}$
Immune response subtract immune cell coefficient $\beta_{sub}$	$1/6000 \text{cell}^{-1} \text{s}^{-1}$	Selected according to $\beta_{add}$ for 5 resident immune cells (mean of all immune cell counts per epithelial cell from Control in [22] applied to 900 epithelial cells)
Immune response delay coefficient $\beta_{delay}$	$1.2 \times 10^6 \text{s}$	Selected according to sensitivity analysis
Immune response decay coefficient $\beta_{decay}$	$1/12000 \text{s}^{-1}$	Selected for sensitivity analysis of $\beta_{delay}$
Immune response cytokine transmission coefficient $\alpha_{sig}$	0.5	Selected for sensitivity analysis of $\beta_{delay}$
Immune response probability scaling coefficient $\alpha_{immune}$	0.01	Selected for sensitivity analysis of $\beta_{delay}$
Number of immune cell seeding samples $n_{seeding}$	10	Selected for sensitivity analysis of $\beta_{delay}$
Initial target volume	$64 \mu\text{m}^3$	Derived from cell diameter and lattice width

Lambda volume $\lambda_{volume}$	9	Selected for acceptable deformation of immune cells
Initial number of immune cells	0	Selected to demonstrate model feature of resident immune cells
Lambda chemotaxis $\lambda_{chemotaxis}$	1	Selected for appreciable chemotaxis without excessive cell deformation
Intrinsic Random Motility $\mathcal{H}^*$	10	[68]
Contact coefficients $J$ (all interfaces)	10	Selected comparably to [68] for low adhesion immune cell-immune cell and immune cell-medium interfaces

1567 <sup>1</sup> The diffusivity in water for a virus of radius 0.1 microns like SARS-CoV-2 according to Stokes-Einstein is about 3 microns<sup>2</sup>/s. The  
1568 average steady-shear viscosity for lung mucus varies significantly and is shear thinning, but in the more viscous regions is found to  
1569 vary for frequencies between 10<sup>-4</sup> and 102 Hz, spanning viscosity values as high as 103 Pa-s and as low as 10<sup>-2</sup> Pa-s. In general, at  
1570 low shear rates, the viscosity of human mucus is as high as 104–106 times that of water [74]. Thus the minimal diffusion constant  
1571 possible would be 3 x 10<sup>-6</sup> microns<sup>2</sup>/s and the maximal rate in water would be 3 microns<sup>2</sup>/s. 0.01 microns<sup>2</sup>/s is a reasonable geometric  
1572 interpolation.

1573

## 1574 References

- 1575 1. Cao Y-C, Deng Q-X, Dai S-X. Remdesivir for severe acute respiratory syndrome  
1576 coronavirus 2 causing COVID-19: An evaluation of the evidence. *Travel Med Infect*  
1577 *Dis.* 2020; 101647–101647. doi:10.1016/j.tmaid.2020.101647
- 1578 2. Wang D, Yin Y, Hu C, Liu X, Zhang X, Zhou S, et al. Clinical course and outcome of  
1579 107 patients infected with the novel coronavirus, SARS-CoV-2, discharged from two  
1580 hospitals in Wuhan, China. *Critical Care.* 2020;24: 188. doi:10.1186/s13054-020-  
1581 02895-6
- 1582 3. Eckhardt M, Hultquist JF, Kaake RM, Hüttenhain R, Krogan NJ. A systems approach  
1583 to infectious disease. *Nature Reviews Genetics.* 2020;21: 339–354.  
1584 doi:10.1038/s41576-020-0212-5
- 1585 4. Dolley S. Big Data’s Role in Precision Public Health. *Front Public Health.* 2018;6: 68–  
1586 68. doi:10.3389/fpubh.2018.00068
- 1587 5. Garira W. A primer on multiscale modelling of infectious disease systems. *Infectious*  
1588 *Disease Modelling.* 2018;3: 176–191. doi:10.1016/j.idm.2018.09.005
- 1589 6. Koelle K, Farrell AP, Brooke CB, Ke R. Within-host infectious disease models  
1590 accommodating cellular coinfection, with an application to influenza†. *Virus Evolution.*  
1591 2019;5. doi:10.1093/ve/vez018
- 1592 7. Wang Y, Heiland R, Craig M, Davis C, Ford Versypt AN, Jenner A, et al. Rapid  
1593 community-driven development of a SARS-CoV-2 tissue simulator. *bioRxiv.* 2020;  
1594 2020.04.02.019075. doi:10.1101/2020.04.02.019075
- 1595 8. Hernandez Vargas EA, Velasco-Hernandez JX. In-host Modelling of COVID-19  
1596 Kinetics in Humans. *medRxiv.* 2020; 2020.03.26.20044487.  
1597 doi:10.1101/2020.03.26.20044487
- 1598 9. Dee KU, Hammer DA, Shuler ML. A model of the binding, entry, uncoating, and RNA  
1599 synthesis of Semliki Forest virus in baby hamster kidney (BHK-21) cells.  
1600 *Biotechnology and Bioengineering.* 1995;46: 485–496. doi:10.1002/bit.260460513
- 1601 10. English TJ, Hammer DA. Brownian adhesive dynamics (BRAD) for simulating the  
1602 receptor-mediated binding of viruses. *Biophys J.* 2004;86: 3359–3372.  
1603 doi:10.1529/biophysj.103.027813
- 1604 11. Boireau S, Maiuri P, Basyuk E, de la Mata M, Knezevich A, Pradet-Balade B, et al.  
1605 The transcriptional cycle of HIV-1 in real-time and live cells. *J Cell Biol.* 2007;179:  
1606 291–304. doi:10.1083/jcb.200706018
- 1607 12. Roldão A, Vieira HLA, Charpilienne A, Poncet D, Roy P, Carrondo MJT, et al.  
1608 Modeling rotavirus-like particles production in a baculovirus expression vector system:  
1609 Infection kinetics, baculovirus DNA replication, mRNA synthesis and protein  
1610 production. *Journal of Biotechnology.* 2007;128: 875–894.  
1611 doi:10.1016/j.jbiotec.2007.01.003
- 1612 13. Purohit PK, Inamdar MM, Grayson PD, Squires TM, Kondev J, Phillips R. Forces  
1613 during bacteriophage DNA packaging and ejection. *Biophys J.* 2004/11/19 ed.  
1614 2005;88: 851–866. doi:10.1529/biophysj.104.047134
- 1615 14. Yang Q, Catalano CE. A minimal kinetic model for a viral DNA packaging machine.  
1616 *Biochemistry.* 2004;43: 289–299. doi:10.1021/bi035532h
- 1617 15. Graw F, Perelson A. Spatial aspects of HIV infection. 2013. pp. 3–31.  
1618 doi:10.1007/978-1-4614-4178-6\_1
- 1619 16. Ferl GZ, Theil F-P, Wong H. Physiologically based pharmacokinetic models of

- 1620 small molecules and therapeutic antibodies: a mini-review on fundamental concepts  
1621 and applications. *Biopharmaceutics & Drug Disposition*. 2016;37: 75–92.  
1622 doi:10.1002/bdd.1994
- 1623 17. Bauer AL, Beauchemin CAA, Perelson AS. Agent-based modeling of host–  
1624 pathogen systems: The successes and challenges. *Inf Sci (N Y)*. 2009;179: 1379–  
1625 1389. doi:10.1016/j.ins.2008.11.012
- 1626 18. Beauchemin C. Probing the effects of the well-mixed assumption on viral infection  
1627 dynamics. *J Theor Biol*. 2006;242: 464–477. doi:10.1016/j.jtbi.2006.03.014
- 1628 19. Olafuyi O, Badhan RKS. Dose Optimization of Chloroquine by Pharmacokinetic  
1629 Modeling During Pregnancy for the Treatment of Zika Virus Infection. *JPharmSci*.  
1630 2019;108: 661–673. doi:10.1016/j.xphs.2018.10.056
- 1631 20. Holder BP, Liao LE, Simon P, Boivin G, Beauchemin CAA. Design considerations  
1632 in building in silico equivalents of common experimental influenza virus assays.  
1633 *Autoimmunity*. 2011;44: 282–293. doi:10.3109/08916934.2011.523267
- 1634 21. Miao C, Jin M, Miao L, Yang X, Huang P, Xiong H, et al. Early chest computed  
1635 tomography to diagnose COVID-19 from suspected patients: A multicenter  
1636 retrospective study. *The American Journal of Emergency Medicine*. 2020;0.  
1637 doi:10.1016/j.ajem.2020.04.051
- 1638 22. Chua RL, Lukassen S, Trump S, Hennig BP, Wendisch D, Pott F, et al. COVID-19  
1639 severity correlates with airway epithelium–immune cell interactions identified by  
1640 single-cell analysis. *Nature Biotechnology*. 2020;38: 970–979. doi:10.1038/s41587-  
1641 020-0602-4
- 1642 23. Zhou S, Zhu T, Wang Y, Xia L. Imaging features and evolution on CT in 100  
1643 COVID-19 pneumonia patients in Wuhan, China. *Eur Radiol*. 2020; 1–9.  
1644 doi:10.1007/s00330-020-06879-6
- 1645 24. Taubenberger JK, Morens DM. The pathology of influenza virus infections. *Annu*  
1646 *Rev Pathol*. 2008;3: 499–522. doi:10.1146/annurev.pathmechdis.3.121806.154316
- 1647 25. Bocharov G, Meyerhans A, Bessonov N, Trofimchuk S, Volpert V. Spatiotemporal  
1648 Dynamics of Virus Infection Spreading in Tissues. *PLOS ONE*. 2016;11: e0168576.  
1649 doi:10.1371/journal.pone.0168576
- 1650 26. Hattaf K. Spatiotemporal Dynamics of a Generalized Viral Infection Model with  
1651 Distributed Delays and CTL Immune Response. *Computation*. 2019;7: 21.  
1652 doi:10.3390/computation7020021
- 1653 27. Koullapis PG, Stylianou FS, Sznitman J, Olsson B, Kassinos SC. Towards whole-  
1654 lung simulations of aerosol deposition: A model of the deep lung. *J Aerosol Sci*.  
1655 2020;144: 105541. doi:10.1016/j.jaerosci.2020.105541
- 1656 28. Strain MC, Richman DD, Wong JK, Levine H. Spatiotemporal Dynamics of HIV  
1657 Propagation. *Journal of Theoretical Biology*. 2002;218: 85–96.  
1658 doi:10.1006/jtbi.2002.3055
- 1659 29. Dong X, Foteinou PT, Calvano SE, Lowry SF, Androulakis IP. Agent-Based  
1660 Modeling of Endotoxin-Induced Acute Inflammatory Response in Human Blood  
1661 Leukocytes. *PLOS ONE*. 2010;5: e9249. doi:10.1371/journal.pone.0009249
- 1662 30. Linderman JJ, Riggs T, Pande M, Miller M, Marino S, Kirschner DE. Characterizing  
1663 the Dynamics of CD4+ T Cell Priming within a Lymph Node. *The Journal of*  
1664 *Immunology*. 2010;184: 2873–2885. doi:10.4049/jimmunol.0903117
- 1665 31. Immonen T, Gibson R, Leitner T, Miller M, Arts E, Somersalo E, et al. A hybrid



- 1666 stochastic-deterministic computational model accurately describes spatial dynamics  
1667 and virus diffusion in HIV-1 growth competition assay. *Journal of theoretical biology*.  
1668 2012;312C: 120–132. doi:10.1016/j.jtbi.2012.07.005
- 1669 32. Zorzenon dos Santos RM, Coutinho S. Dynamics of HIV Infection: A cellular  
1670 automata approach. *Phys Rev Lett*. 2001;87: 168102.  
1671 doi:10.1103/PhysRevLett.87.168102
- 1672 33. Imle A, Kumberger P, Schnellbacher ND, Fehr J, Carrillo-Bustamante P, Ales J, et  
1673 al. Experimental and computational analyses reveal that environmental restrictions  
1674 shape HIV-1 spread in 3D cultures. *Nat Commun*. 2019;10: 2144.  
1675 doi:10.1038/s41467-019-09879-3
- 1676 34. Myers MA, Smith AP, Lane LC, Moquin DJ, Vogel P, Woolard S, et al. Dynamically  
1677 linking influenza virus infection with lung injury to predict disease severity. *bioRxiv*.  
1678 2019; 555276. doi:10.1101/555276
- 1679 35. Funk GA, Jansen VAA, Bonhoeffer S, Killingback T. Spatial models of virus-  
1680 immune dynamics. *Journal of Theoretical Biology*. 2005;233: 221–236.  
1681 doi:10.1016/j.jtbi.2004.10.004
- 1682 36. Lippi G, Sanchis-Gomar F, Henry BM. COVID-19: unravelling the clinical  
1683 progression of nature's virtually perfect biological weapon. *Ann Transl Med*. 2020;8.  
1684 doi:10.21037/atm-20-3989
- 1685 37. Carrasco Pro S, Dafonte Imedio A, Santoso CS, Gan KA, Sewell JA, Martinez M,  
1686 et al. Global landscape of mouse and human cytokine transcriptional regulation.  
1687 *Nucleic Acids Research*. 2018;46: 9321–9337. doi:10.1093/nar/gky787
- 1688 38. Akira S, Uematsu S, Takeuchi O. Pathogen Recognition and Innate Immunity. *Cell*.  
1689 2006;124: 783–801. doi:10.1016/j.cell.2006.02.015
- 1690 39. Ahlquist P, Noueiry AO, Lee W-M, Kushner DB, Dye BT. Host Factors in Positive-  
1691 Strand RNA Virus Genome Replication. *J Virol*. 2003;77: 8181.  
1692 doi:10.1128/JVI.77.15.8181-8186.2003
- 1693 40. Shuster DE, Kehrl ME, Rainard P, Paape M. Complement fragment C5a and  
1694 inflammatory cytokines in neutrophil recruitment during intramammary infection with  
1695 *Escherichia coli*. *Infect Immun*. 1997;65: 3286.
- 1696 41. Strieter RM, Lukacs NW, Standiford TJ, Kunkel SL. Cytokines. 2. Cytokines and  
1697 lung inflammation: mechanisms of neutrophil recruitment to the lung. *Thorax*.  
1698 1993;48: 765. doi:10.1136/thx.48.7.765
- 1699 42. Chou RC, Kim ND, Sadik CD, Seung E, Lan Y, Byrne MH, et al. Lipid-Cytokine-  
1700 Chemokine Cascade Drives Neutrophil Recruitment in a Murine Model of  
1701 Inflammatory Arthritis. *Immunity*. 2010;33: 266–278.  
1702 doi:10.1016/j.immuni.2010.07.018
- 1703 43. Edelblum KL, Turner JR. Chapter 12 - Epithelial cells: structure, transport, and  
1704 barrier function. In: Mestecky J, Strober W, Russell MW, Kelsall BL, Cheroutre H,  
1705 Lambrecht BN, editors. *Mucosal Immunology (Fourth Edition)*. Boston: Academic  
1706 Press; 2015. pp. 187–210. doi:10.1016/B978-0-12-415847-4.00012-4
- 1707 44. Smith AM. Validated Models of Immune Response to Virus Infection. *Curr Opin*  
1708 *Syst Biol*. 2018/10/31 ed. 2018;12: 46–52. doi:10.1016/j.coisb.2018.10.005
- 1709 45. Smith AM, Perelson AS. Influenza A virus infection kinetics: quantitative data and  
1710 models. *Wiley Interdiscip Rev Syst Biol Med*. 2011;3: 429–445.  
1711 doi:10.1002/wsbm.129

- 1712 46. Dusséaux M, Masse-Ranson G, Darche S, Ahodantin J, Li Y, Fiquet O, et al. Viral  
1713 Load Affects the Immune Response to HBV in Mice With Humanized Immune System  
1714 and Liver. *Gastroenterology*. 2017;153: 1647-1661.e9.  
1715 doi:10.1053/j.gastro.2017.08.034
- 1716 47. Veiga-Parga T, Sehrawat S, Rouse BT. Role of Regulatory T Cells during Virus  
1717 Infection. *Immunol Rev*. 2013;255: 182–196. doi:10.1111/imr.12085
- 1718 48. Rosendahl Huber S, van Beek J, de Jonge J, Luytjes W, van Baarle D. T cell  
1719 responses to viral infections - opportunities for Peptide vaccination. *Front Immunol*.  
1720 2014;5: 171–171. doi:10.3389/fimmu.2014.00171
- 1721 49. Le Page C, Génin P, Baines M, Hiscott J. Interferon activation and innate immunity.  
1722 *Rev Immunogenet*. 2000;2: 374–386.
- 1723 50. Abbas AK, Lichtman AH, Pillai S. Cellular and molecular immunology. 9th ed.  
1724 Philadelphia, PA: Saunders/Elsevier; 2017.
- 1725 51. Ploquin A, Zhou Y, Sullivan NJ. Ebola Immunity: Gaining a Winning Position in  
1726 Lightning Chess. *Jl*. 2018;201: 833–842. doi:10.4049/jimmunol.1700827
- 1727 52. Regoes RR, Crotty S, Antia R, Tanaka MM. Optimal Replication of Poliovirus within  
1728 Cells. *The American Naturalist*. 2005;165: 364–373. doi:10.1086/428295
- 1729 53. Yin J, Redovich J. Kinetic Modeling of Virus Growth in Cells. *Microbiol Mol Biol*  
1730 *Rev*. 2018;82: e00066-17. doi:10.1128/MMBR.00066-17
- 1731 54. Yu X, Zeng X, Shi W, Hu Y, Nie W, Chu N, et al. Validation of Cycloserine Efficacy  
1732 in Treatment of Multidrug-Resistant and Extensively Drug-Resistant Tuberculosis in  
1733 Beijing, China. *Antimicrobial Agents and Chemotherapy*. 2018;62.  
1734 doi:10.1128/AAC.01824-17
- 1735 55. Swat MH, Thomas GL, Belmonte JM, Shirinifard A, Hmeljak D, Glazier JA. Multi-  
1736 scale modeling of tissues using CompuCell3D. *Methods Cell Biol*. 2012;110: 325–  
1737 366. doi:10.1016/B978-0-12-388403-9.00013-8
- 1738 56. Harcourt J, Tamin A, Lu X, Kamili S, Sakthivel SK, Murray J, et al. Severe Acute  
1739 Respiratory Syndrome Coronavirus 2 from Patient with Coronavirus Disease, United  
1740 States. *Emerg Infect Dis*. 2020;26: 1266–1273. doi:10.3201/eid2606.200516
- 1741 57. Cheng AH-D, Cheng DT. Heritage and early history of the boundary element  
1742 method. *Eng Anal Bound Elem*. 2005;29: 268–302.  
1743 doi:10.1016/j.enganabound.2004.12.001
- 1744 58. Zhao X, Wang W. Fisher waves in an epidemic model. *Discrete Cont Dyn-B*.  
1745 2004;4: 1117–1128. doi:10.3934/dcdsb.2004.4.1117
- 1746 59. Dahari H, Ribeiro RM, Rice CM, Perelson AS. Mathematical modeling of  
1747 subgenomic hepatitis C virus replication in Huh-7 cells. *J Virol*. 2007;81: 750.  
1748 doi:10.1128/JVI.01304-06
- 1749 60. Warren TK, Jordan R, Lo MK, Ray AS, Mackman RL, Soloveva V, et al.  
1750 Therapeutic efficacy of the small molecule GS-5734 against Ebola virus in rhesus  
1751 monkeys. *Nature*. 2016/03/02 ed. 2016;531: 381–385. doi:10.1038/nature17180
- 1752 61. Gonçalves A, Bertrand J, Ke R, Comets E, Lamballerie X de, Malvy D, et al. Timing  
1753 of Antiviral Treatment Initiation is Critical to Reduce SARS- CoV- 2 Viral Load. In:  
1754 CPT: Pharmacometrics & Systems Pharmacology [Internet]. John Wiley & Sons, Ltd;  
1755 7 Aug 2020 [cited 1 Sep 2020]. Available:  
1756 <https://ascpt.onlinelibrary.wiley.com/doi/abs/10.1002/psp4.12543>
- 1757 62. Goyal A, Cardozo-Ojeda EF, Schiffer JT. Potency and timing of antiviral therapy

- 1758 as determinants of duration of SARS CoV-2 shedding and intensity of inflammatory  
1759 response. medRxiv. 2020; 2020.04.10.20061325. doi:10.1101/2020.04.10.20061325
- 1760 63. Weaver JJA, Shoemaker JE. Mathematical Modeling of RNA Virus Sensing  
1761 Pathways Reveals Paracrine Signaling as the Primary Factor Regulating Excessive  
1762 Cytokine Production. *Processes*. 2020;8: 719. doi:10.3390/pr8060719
- 1763 64. Mirams GR, Arthurs CJ, Bernabeu MO, Bordas R, Cooper J, Corrias A, et al.  
1764 Chaste: an open source C++ library for computational physiology and biology. *PLoS*  
1765 *Comput Biol*. 2013;9: e1002970. doi:10.1371/journal.pcbi.1002970
- 1766 65. Pitt-Francis J, Pathmanathan P, Bernabeu MO, Bordas R, Cooper J, Fletcher AG,  
1767 et al. Chaste: A test-driven approach to software development for biological modelling.  
1768 *Comput Phys Commun*. 2009;180: 2452–2471. doi:10.1016/j.cpc.2009.07.019
- 1769 66. Starruß J, de Back W, Brusch L, Deutsch A. Morpheus: a user-friendly modeling  
1770 environment for multiscale and multicellular systems biology. *Bioinformatics*. 2014;30:  
1771 1331–1332. doi:10.1093/bioinformatics/btt772
- 1772 67. Smith LP, Bergmann FT, Chandran D, Sauro HM. Antimony: a modular model  
1773 definition language. *Bioinformatics*. 2009/07/03 ed. 2009;25: 2452–2454.  
1774 doi:10.1093/bioinformatics/btp401
- 1775 68. Graner F, Glazier JA. Simulation of biological cell sorting using a two-dimensional  
1776 extended Potts model. *Phys Rev Lett*. 1992;69: 2013–2016.  
1777 doi:10.1103/PhysRevLett.69.2013
- 1778 69. Oyler-Yaniv A, Oyler-Yaniv J, Whitlock BM, Liu Z, Germain RN, Huse M, et al. A  
1779 tunable diffusion-consumption mechanism of cytokine propagation enables plasticity  
1780 in cell-to-cell communication in the immune system. *Immunity*. 2017;46: 609–620.  
1781 doi:10.1016/j.immuni.2017.03.011
- 1782 70. Höfer T, Krichevsky O, Altan-Bonnet G. Competition for IL-2 between regulatory  
1783 and effector T cells to chisel immune responses. *Front Immunol*. 2012;3: 268–268.  
1784 doi:10.3389/fimmu.2012.00268
- 1785 71. Hugues S, Fetler L, Bonifaz L, Helft J, Amblard F, Amigorena S. Distinct T cell  
1786 dynamics in lymph nodes during the induction of tolerance and immunity. *Nature*  
1787 *Immunology*. 2004;5: 1235–1242. doi:10.1038/ni1134
- 1788 72. Walls AC, Park Y-J, Tortorici MA, Wall A, McGuire AT, Velesler D. Structure,  
1789 Function, and Antigenicity of the SARS-CoV-2 Spike Glycoprotein. *Cell*. 2020;181:  
1790 281-292.e6. doi:10.1016/j.cell.2020.02.058
- 1791 73. Wrapp D, Wang N, Corbett KS, Goldsmith JA, Hsieh C-L, Abiona O, et al. Cryo-  
1792 EM structure of the 2019-nCoV spike in the prefusion conformation. *Science*.  
1793 2020;367: 1260–1263. doi:10.1126/science.abb2507
- 1794 74. Lai SK, Wang Y-Y, Wirtz D, Hanes J. Micro- and macrorheology of mucus. *Adv*  
1795 *Drug Deliv Rev*. 2009;61: 86–100. doi:10.1016/j.addr.2008.09.012
- 1796 75. Stray SJ, Air GM. Apoptosis by influenza viruses correlates with efficiency of viral  
1797 mRNA synthesis. *Virus Res*. 2001;77: 3–17. doi:10.1016/s0168-1702(01)00260-x
- 1798

## 1799 **Acknowledgments**

1800           We would like to thank Ramray Bhat, Ryan Danehy, Javier Toledo, Bard  
1801 Ermentrout, Geoffrey Fox, Yi Jiang, Paul Macklin, Jairaj Mathur, Roeland Merks, Ericka  
1802 Mochan, Jason Shoemaker and Amber Smith for useful discussions and ideas and for  
1803 comments on the manuscript. JAG, TJS, JFG and JAS acknowledge funding from  
1804 National Institutes of Health grants U24 EB028887 and R01 GM122424 and National  
1805 Science Foundation grant NSF 1720625. LB acknowledges grant 01ZX1707A within the  
1806 German e:Med initiative (BMBF) and grant 391070520 from the German Research  
1807 Foundation (DFG). R.K.P. was supported, in part, by National Institutes of Health grants  
1808 R01 AI071002, R01 AI141222 and R01 HD079327. This research was supported in part  
1809 by Lilly Endowment, Inc., through its support for the Indiana University Pervasive  
1810 Technology Institute. The funders had no role in manuscript preparation or the decision  
1811 to submit the work for publication.

1812

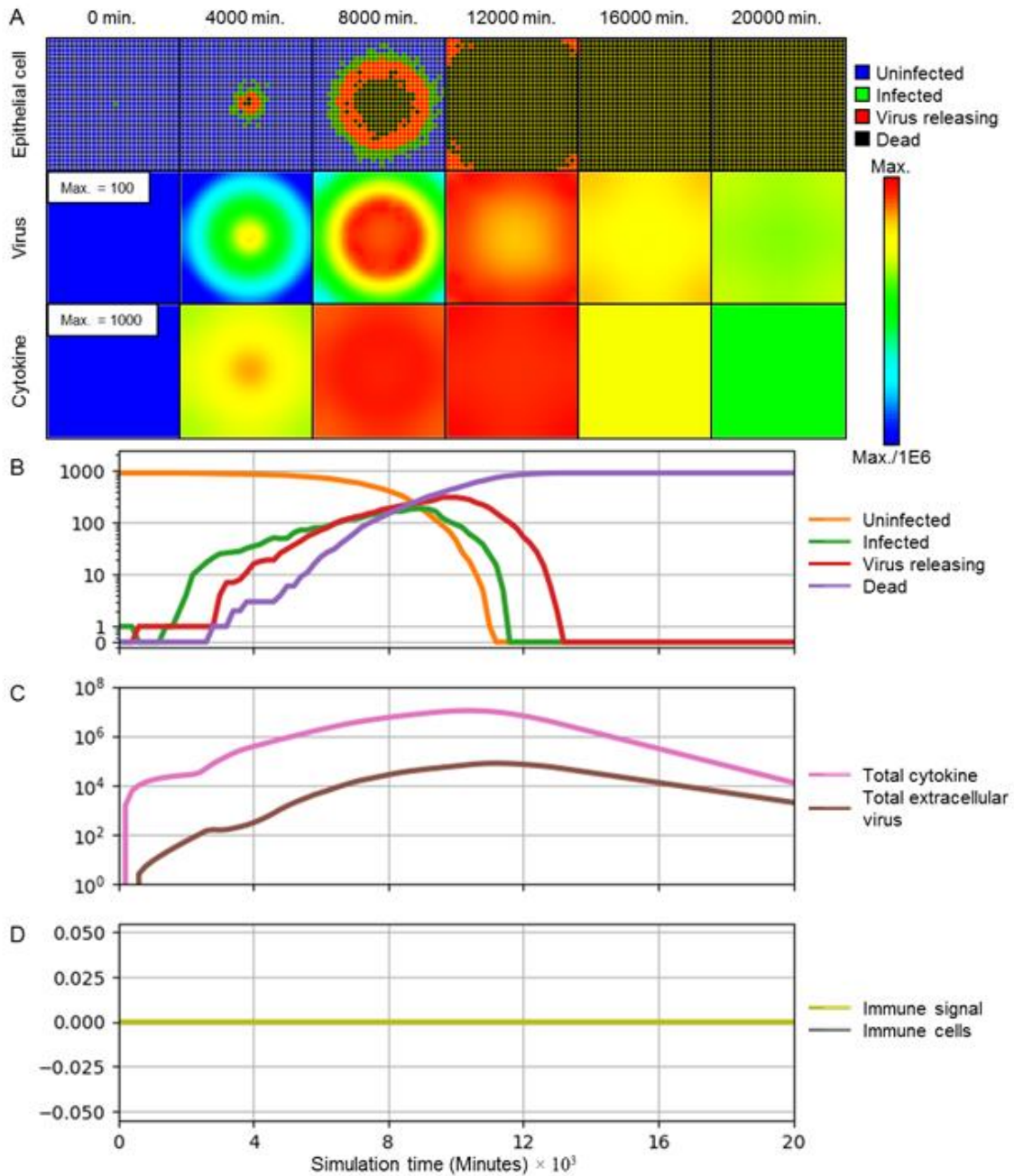
## 1813 **Competing Interests**

1814           JAG is the owner/operator of Virtual Tissues for Health, LLC, which develops  
1815 applications of multiscale tissue models in medical applications and is a shareholder in  
1816 Gilead Life Sciences.

1817

1818 **Supplementary Materials**

1819



1820

1821 **Fig S1. No immune system.**

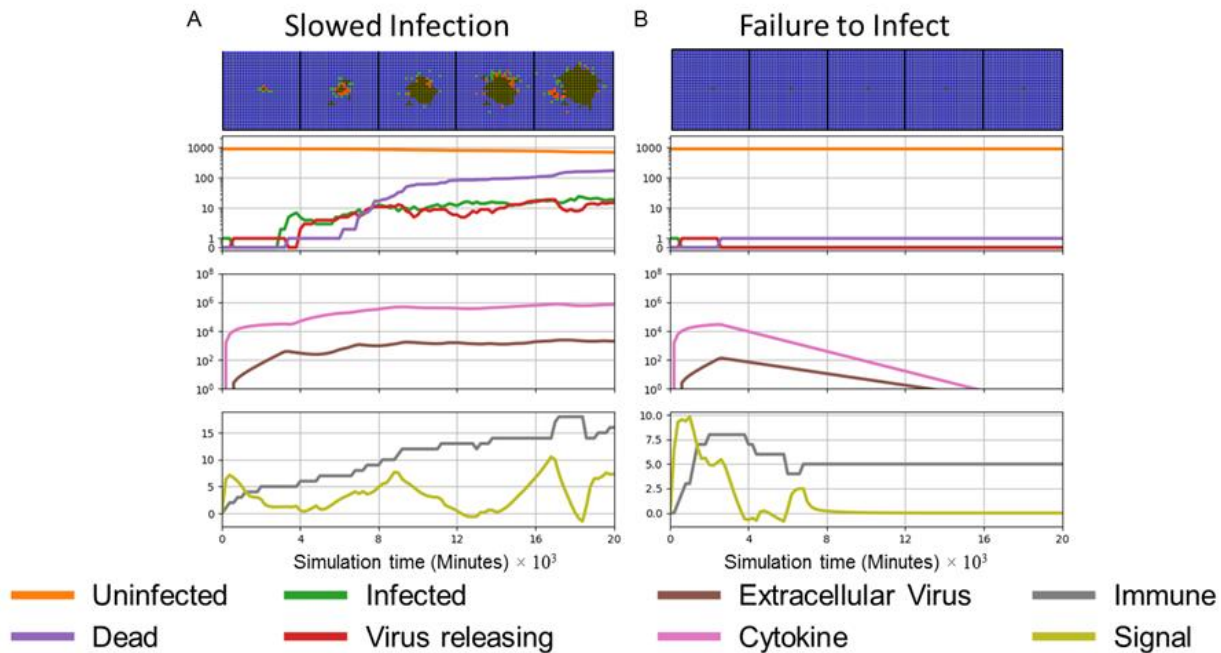
1822 Simulation of the progression of infection in a patch of epithelial tissue, with all parameters as in Fig 3, but with no

1823 cellular immune system response corresponding to virus spread in an *in vitro* or organoid culture, or a severely

1824 immunosuppressed individual. (A) Snapshots of spatial configuration vs time showing progression of simulated



1825 infection. Columns, left to right: 0 minutes (time of initial infection), 4000 minutes (67 hours, 2  $\frac{3}{4}$  days) after infection,  
 1826 8000 minutes (133 hours, 5  $\frac{1}{2}$  days), 12000 minutes (200 hours, 8  $\frac{1}{3}$  days), 16000 minutes (267 hours, 11 days), and  
 1827 20000 minutes (333 hours, 14 days). First row: epithelial cell layer composed of uninfected (blue), infected (green),  
 1828 virus releasing (red) cells and dead cells (black). Second row: level of extracellular virus field. Third row: extracellular  
 1829 cytokine field. Fields are color-coded on a logarithmic scale: red corresponds to the chosen maximum value specified  
 1830 in the first panel, blue to six orders of magnitude lower than the maximum value, and values outside this range are  
 1831 colored as their closest border value. (B-D) Simulation time series. (B) Number of uninfected (orange), infected (green),  
 1832 virus releasing (red) and dead (purple) epithelial cells on a logarithmic scale vs time vs time in minutes. (C) Total  
 1833 extracellular cytokine (magenta) and total extracellular virus (brown) on a logarithmic scale vs time in minutes. (D)  
 1834 Value of the immune recruitment signal  $S$  (yellow) and number of immune cells (grey) on a linear scale vs time in  
 1835 minutes.  
 1836



1837

1838 **Fig S2. Special cases of spatiotemporal infection dynamics.**

1839 (A) A border case of slowed infection towards containment is Slowed Infection with constant virus: when the net  
 1840 effectiveness of viral and immune dynamics are balanced, the number of infected cells and the total extracellular virus  
 1841 fluctuate around steady state levels. (B) A limit case of Clearance is the failure to infect: initially infected cells may  
 1842 replicate and secrete virus, but insufficiently so to infect other cells during simulation time such that any initially infected  
 1843 cells vanish and total extracellular virus drops below a threshold of  $10^{-3}$  per cell area.

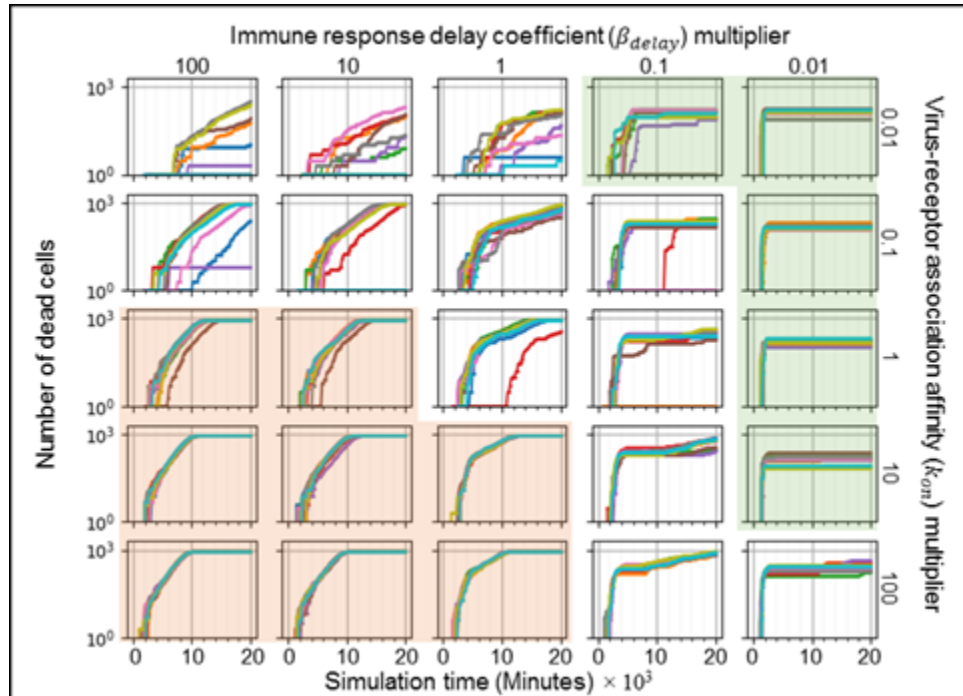


1844

1845 **Table S1. Varying parameters in simulations shown in Fig 4.** Virus-receptor association affinity and immune  
 1846 response delay coefficient shown for no immune response (Fig 4A), widespread infection (Fig 4B), slowed infection  
 1847 (Fig 4C), containment (Fig 4D), recurrence (Fig 4E) and clearance (Fig 4F). All other parameters are as in Table 1.

Parameter	No immune response	Widespread infection	Slowed infection	Containment	Recurrence	Clearance
Virus-receptor association affinity $k_{on}$ ( $M^{-1} s^{-1}$ )	$1.4 \times 10^4$	$1.4 \times 10^4$	$1.4 \times 10^3$	$1.4 \times 10^2$	$1.4 \times 10^6$	$1.4 \times 10^4$
Immune response delay coefficient $\beta_{delay}$ (s)	-	$1.2 \times 10^7$ s	$1.2 \times 10^8$ s	$1.2 \times 10^5$ s	$1.2 \times 10^4$ s	$1.2 \times 10^5$ s

1848

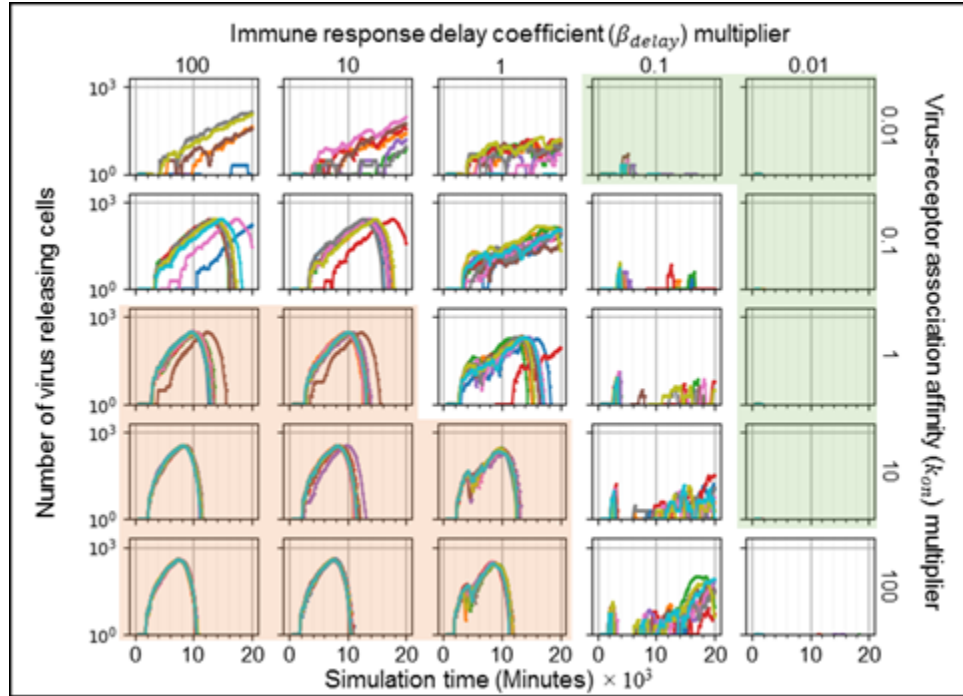


1849

1850 **Fig S3. Time series of the number of uninfected cells for simulations in Fig 5.**

1851 Logarithmic multidimensional parameter sweep performed by running 10 simulation replicas increasing and decreasing  
 1852 the baseline parameter values 10-fold and 100-fold for all parameter sets and replicas in Fig 5. Results show consistent  
 1853 containment/clearance for small  $k_{on}$  and small  $\beta_{delay}$  (upper right, green-shaded subplots), widespread infection for  
 1854 high  $k_{on}$  and small  $\beta_{delay}$  (lower left, orange-shaded subplots), and multiple outcomes for the same parameter values  
 1855 (uncolored subplots). Number of cells are shown on a logarithmic scale vs time in minutes.

1856

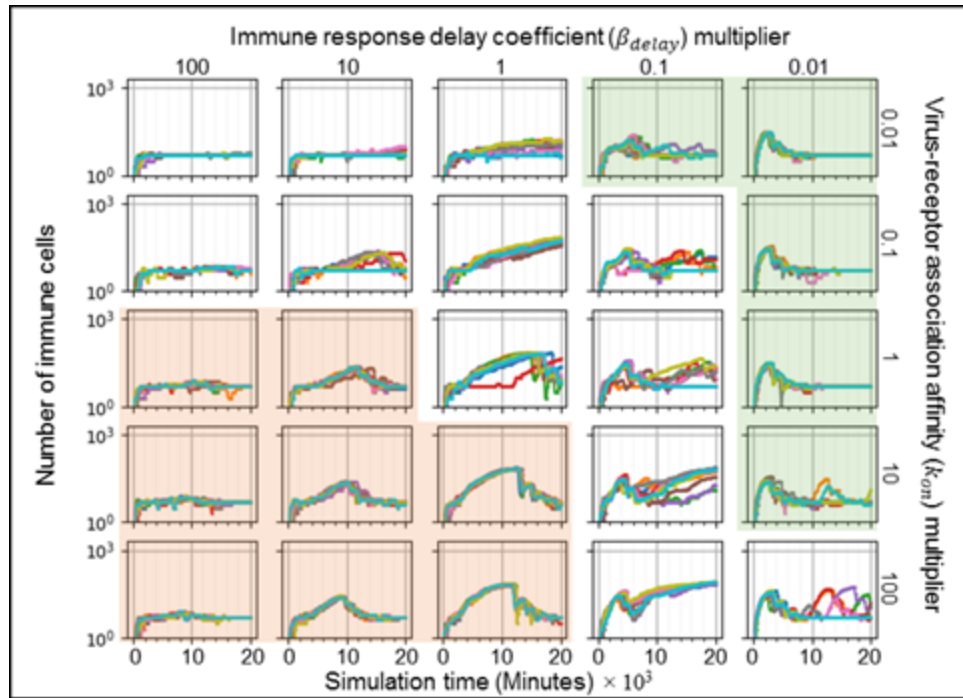


1857

1858 **Fig S4. Time series of the number of virus releasing cells for simulations in Fig 5.**

1859 Logarithmic multidimensional parameter sweep performed by running 10 simulation replicas increasing and decreasing  
1860 the baseline parameter values 10-fold and 100-fold for all parameter sets and replicas in Fig 5. Results show consistent  
1861 containment/clearance for small  $k_{on}$  and small  $\beta_{delay}$  (upper right, green-shaded subplots), widespread infection for  
1862 high  $k_{on}$  and small  $\beta_{delay}$  (lower left, orange-shaded subplots), and multiple outcomes for the same parameter values  
1863 (uncolored subplots). Number of cells are shown on a logarithmic scale vs time in minutes.

1864

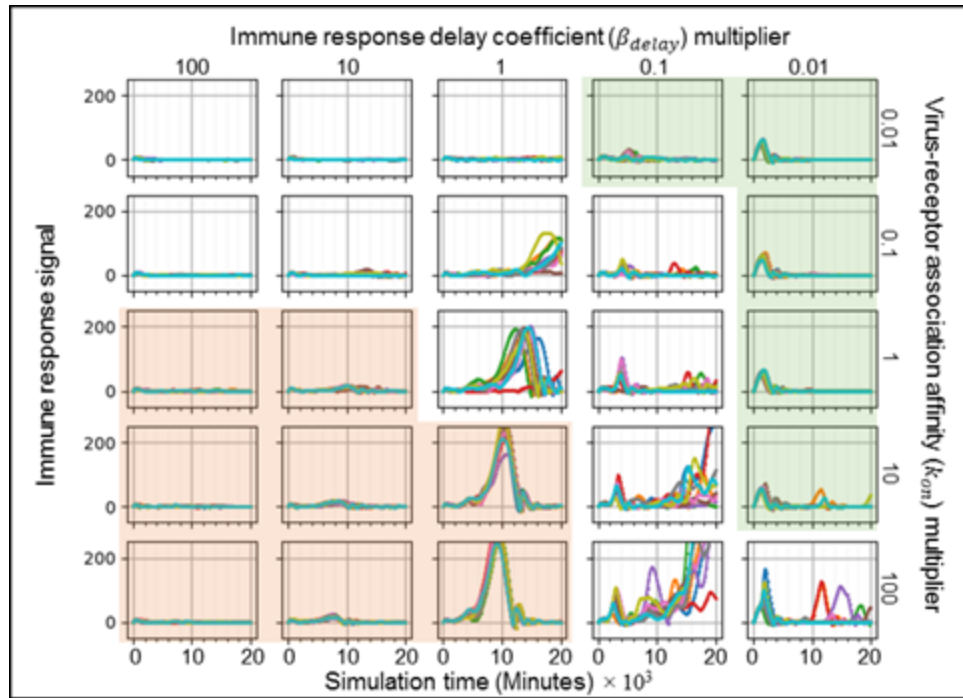


1865

1866 **Fig S5. Time series of the number of immune cells for simulations in Fig 5.**

1867 Logarithmic multidimensional parameter sweep performed by running 10 simulation replicas increasing and decreasing  
1868 the baseline parameter values 10-fold and 100-fold for all parameter sets and replicas in Fig 5. Results show consistent  
1869 containment/clearance for small  $k_{on}$  and small  $\beta_{delay}$  (upper right, green-shaded subplots), widespread infection for  
1870 high  $k_{on}$  and small  $\beta_{delay}$  (lower left, orange-shaded subplots), and multiple outcomes for the same parameter values  
1871 (uncolored subplots). Number of cells are shown on a logarithmic scale vs time in minutes.

1872



1873

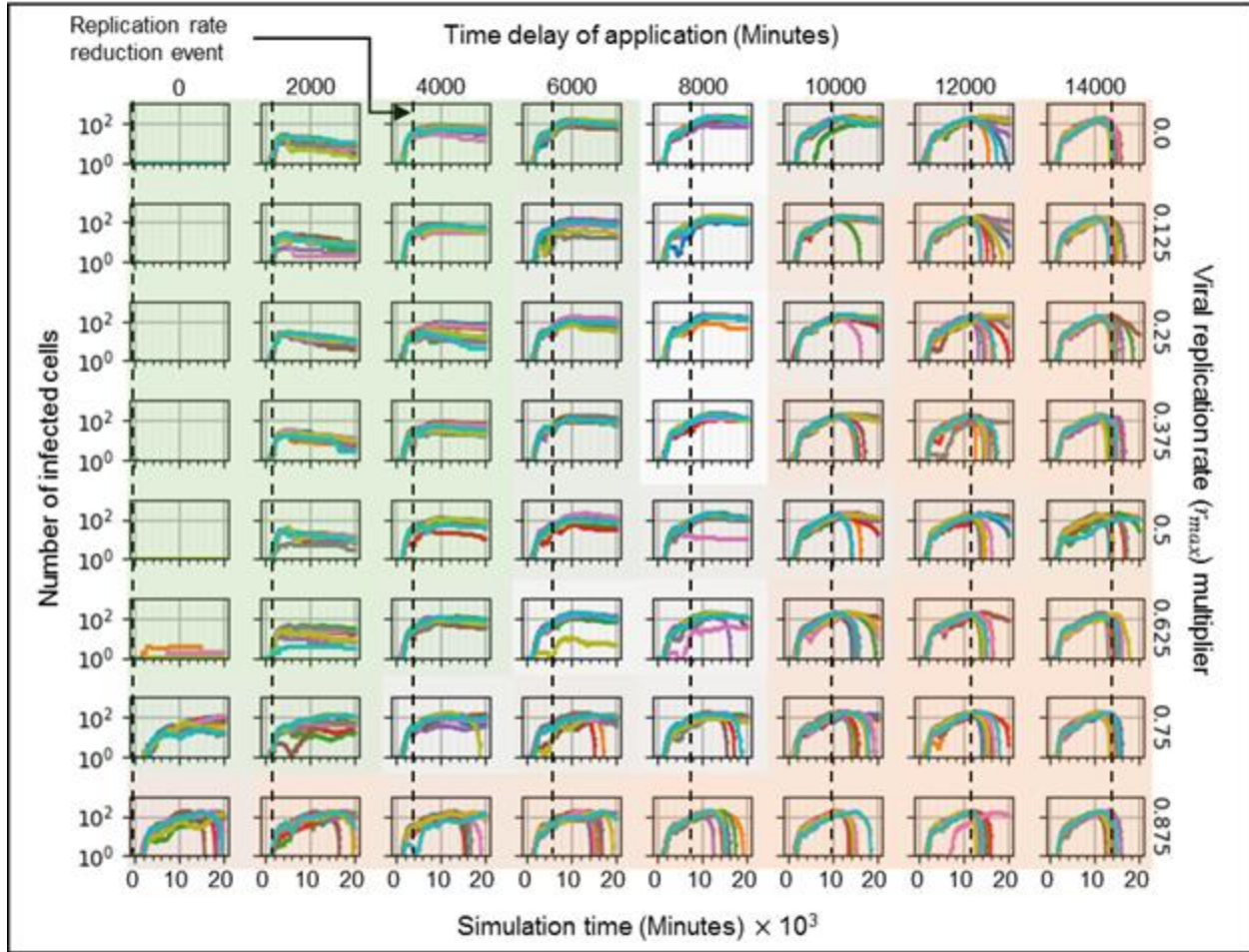
1874 **Fig S6. Time series of the immune response state variable  $S$  for simulations in Fig 5.**

1875 Logarithmic multidimensional parameter sweep performed by running 10 simulation replicas increasing and decreasing  
1876 the baseline parameter values 10-fold and 100-fold for all parameter sets and replicas in Fig 5. Results show consistent  
1877 containment/clearance for small  $k_{on}$  and small  $\beta_{delay}$  (upper right, green-shaded subplots), widespread infection for  
1878 high  $k_{on}$  and small  $\beta_{delay}$  (lower left, orange-shaded subplots), and multiple outcomes for some parameter sets  
1879 (unshaded subplots).  $S$  is shown on a linear scale vs time in minutes.

1880





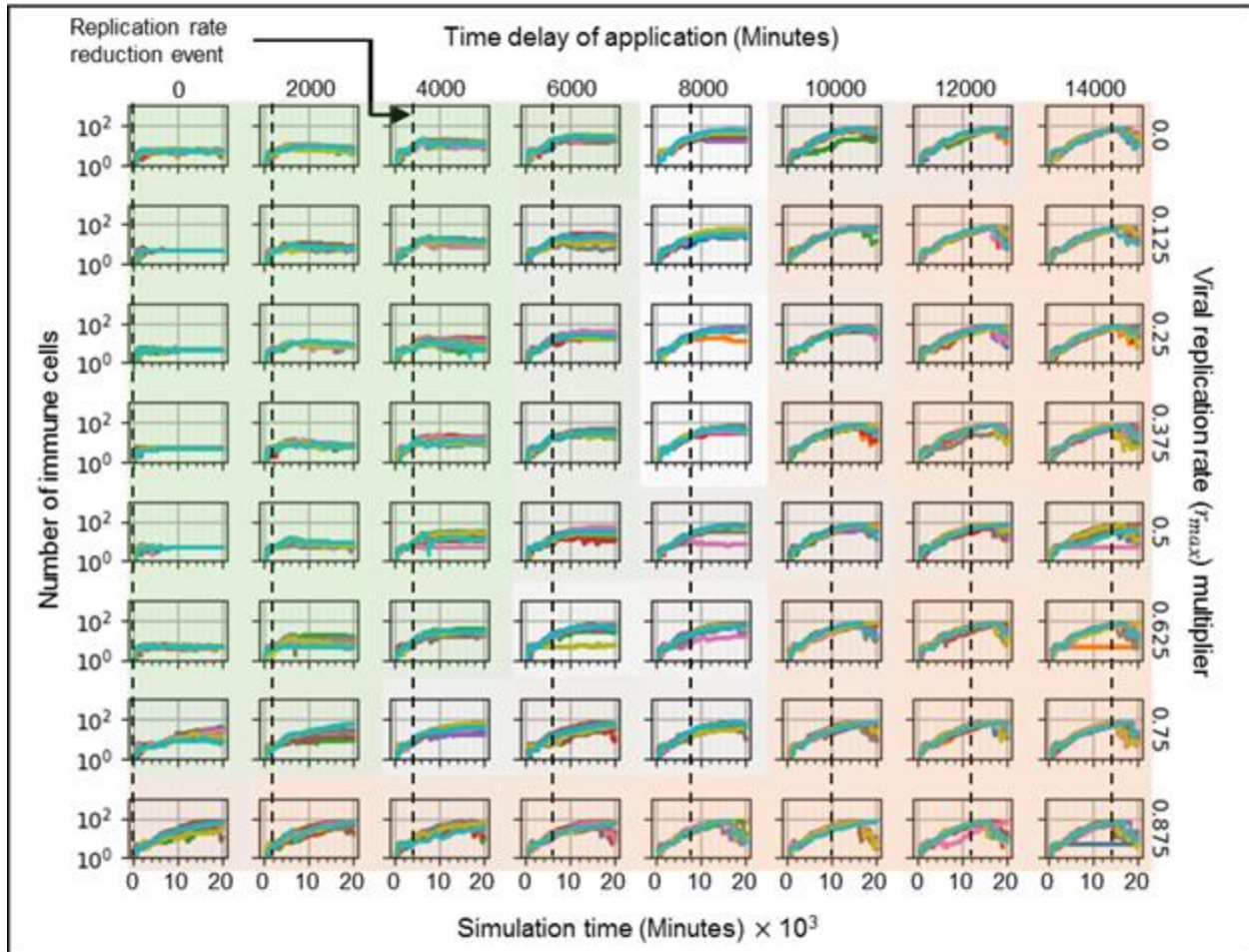


1886

1887 **Fig S8. Simulations from Fig 8, showing the number of infected cells.**

1888 Time series of the number of infected cells for each simulation replica in Fig 8. Number of cells is shown on a logarithmic  
1889 scale vs time in minutes.

1890



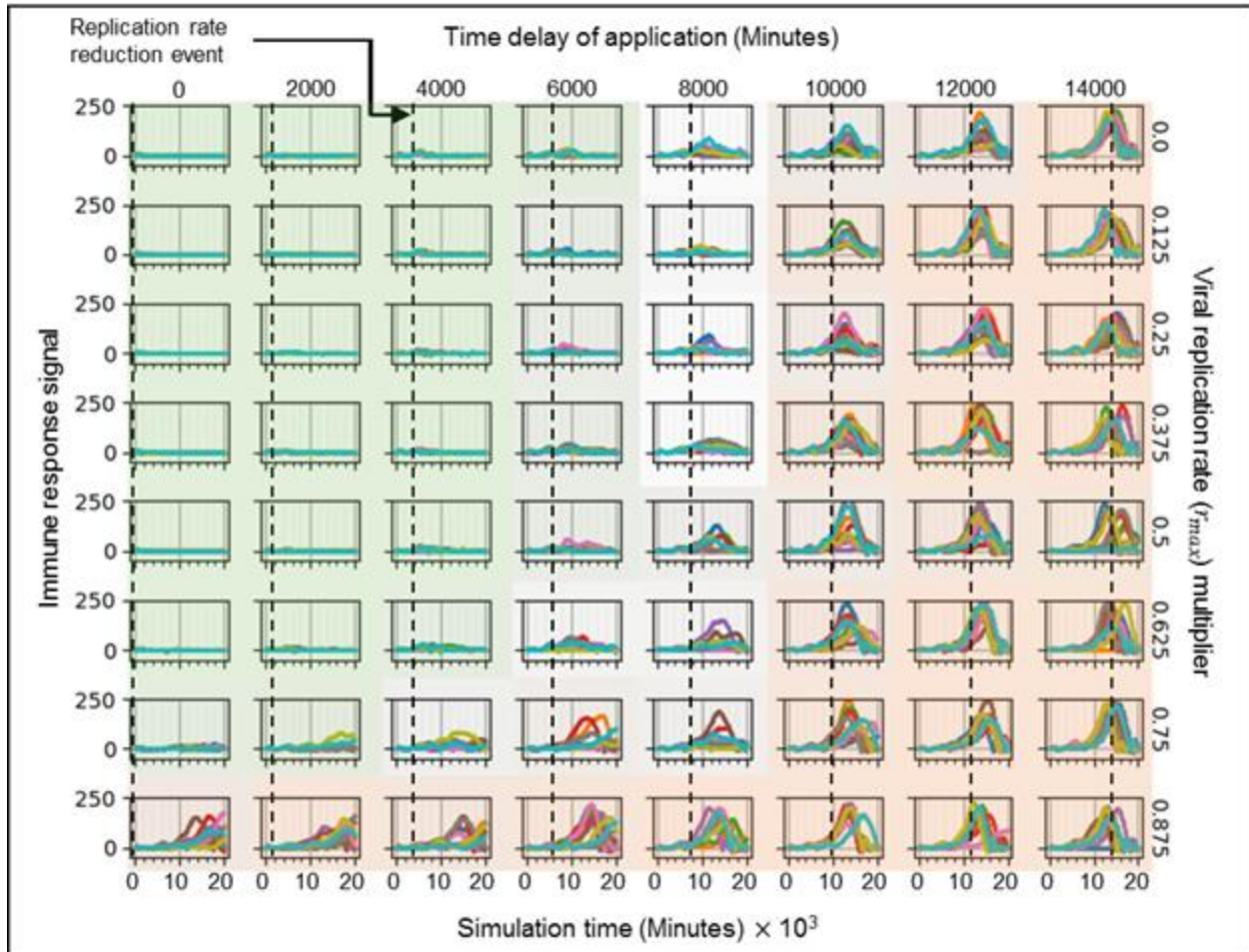
1891

1892 **Fig S9. Simulations from Fig 8 showing the number of immune cells.**

1893 Time series of the number of immune cells for each simulation replica in Fig 8. Number of cells is shown on a logarithmic  
1894 scale vs time in minutes.

1895



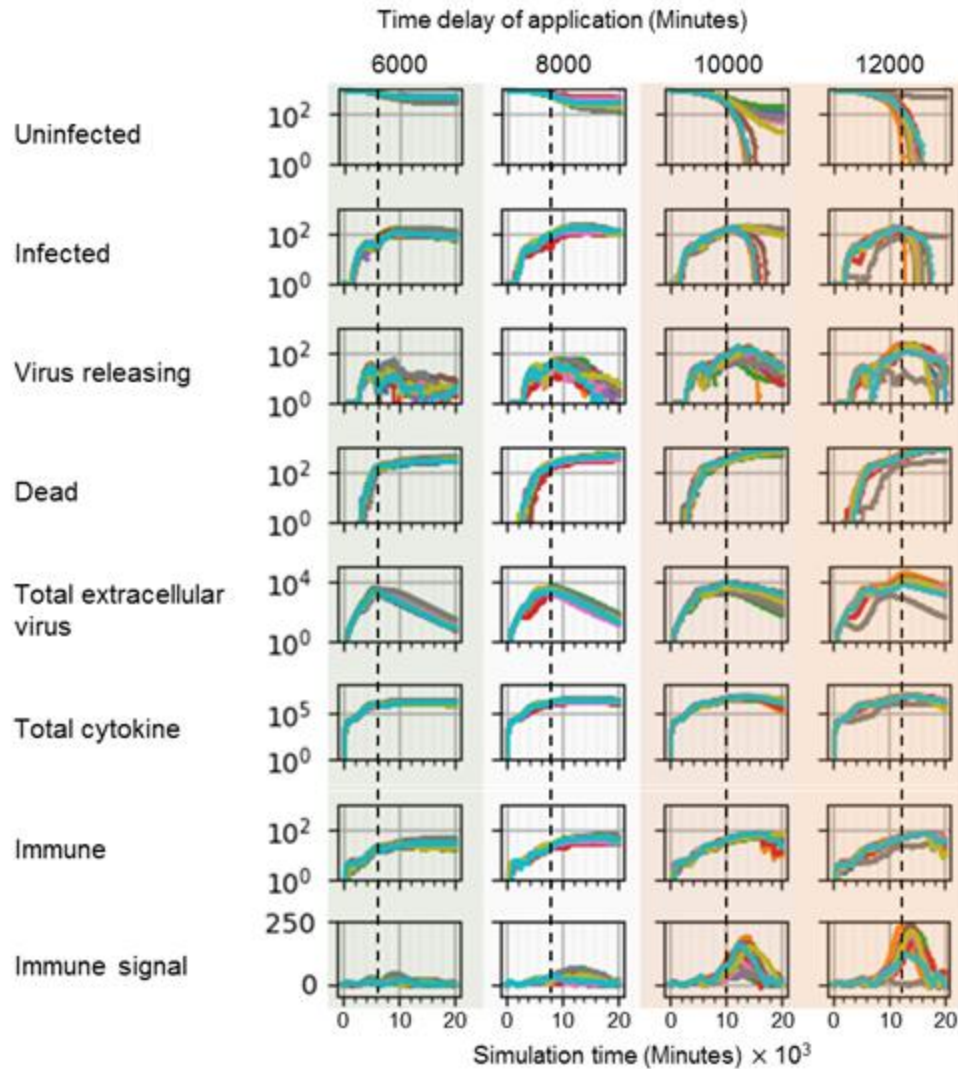


1896

1897 **Fig S10. Simulations from Fig 8 showing the immune response state variable.**

1898 Time series of the immune response state variable  $S$  for each simulation replica in Fig 8.  $S$  is shown on a linear scale  
1899 vs time in minutes.

1900



1901

1902 **Fig S11. Variation in time of first treatment after infection with a reduced viral RNA replication rate causes a**  
 1903 **bifurcation in simulation outcomes.**

1904 Simulations and parameters are as in Figs 9-11, for a viral replication rate multiplier of 0.375 and, from left to right, time  
 1905 delays of application of 6000, 8000, 10000, and 12000 minutes (100, 133, 167 and 200 hours, 4, 5 ½, 7 and 8 ½ days)  
 1906 (dashed lines). Results from all simulation replicas are shown vs time in minutes for, from top to bottom: number of  
 1907 uninfected cells, number of infected cells, number of virus releasing cells, number of dead cells, total extracellular virus,  
 1908 total cytokine, number of immune cells, and immune response state variable *S*. Parameter set subplots are shaded as  
 1909 in Figs 9-11 according to simulation outcomes.

1910

## 1911 **Downloading and running the simulation**

1912           The COVID-19 simulation's source code is available in the GitHub repository  
1913 <https://github.com/covid-tissue-models/covid-tissue-response->  
1914 [models/tree/master/CC3D/Models/BiocIU/SARSCoV2MultiscaleVTM](https://github.com/covid-tissue-models/covid-tissue-response-models/tree/master/CC3D/Models/BiocIU/SARSCoV2MultiscaleVTM). The simulation is a  
1915 model specification which runs in the CompuCell3D virtual-tissue simulation environment.  
1916 To run the simulation requires installation of CompuCell3D version 4.1.1 or later.  
1917 CompuCell3D is open-source and runs on Windows, Mac and Linux operating systems.  
1918 It can be downloaded from <https://compucell3d.org/SrcBin>. Installers are available for  
1919 Windows operating systems and Mac installation also does not require compilation.  
1920 CompuCell3D's manuals are available at <https://compucell3d.org/Manuals>. The COVID-  
1921 19 simulation can also be run online without requiring any installations or downloads on  
1922 the nanoHUB servers at <https://nanohub.org/tools/cc3dcovid19/>. Use of nanoHUB is free  
1923 but requires user registration. The simulation may take a few moments to load in its  
1924 nanoHUB deployment; during load the simulation area will be blue.

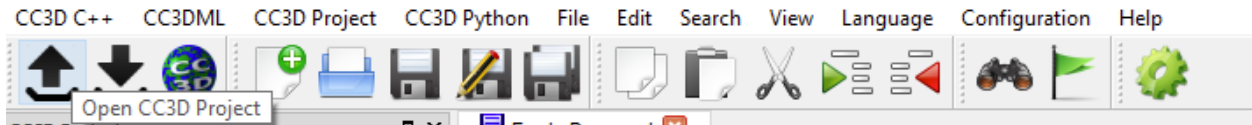
1925           *Twedit++* is a specialized text editor for CompuCell3D simulations which comes  
1926 packaged with CompuCell3D. *Twedit++* can open *cc3d* file extensions which contain the  
1927 simulation file structure for CompuCell3D simulations. To open the COVID-19 simulation  
1928 click "Open CC3D Project" (Fig S12) and select *VirallInfectionVTM.cc3d* in  
1929 `<repository-folder>/covid-tissue-response-`  
1930 `models/CC3D/Models/BiocIU/SARSCoV2MultiscaleVTM/Model`. Once opened,  
1931 *VirallInfectionVTM.cc3d* will appear in the left-hand panel "CC3D Simulation" (Fig S13).  
1932 Double click on it to open all simulation files. The main simulation files are:  
1933 *VirallInfectionVTM.xml*, which defines certain simulation properties (e.g., cell types, lattice

1934 size, energy-constraint plugins, diffusive fields); *VirallInfectionVTMSteppables.py*, which  
1935 defines the simulation's initial conditions, main interactions and dynamics (e.g., cell  
1936 initialization, immune-cell recruitment, secretion by cells into fields, uptake by cells from  
1937 fields); *VirallInfectionVTMSteppableBasePy.py*, where the viral infection Antimony  
1938 submodel is declared; *VirallInfectionVTMModelInputs.py*, which sets the parameters. The  
1939 submodels in *VirallInfectionVTMSteppables.py* are organized as python classes, making  
1940 them easy to modify. Tweedit++ can also copy and rename the simulation project to a  
1941 new directory by using `CC3D Project; Save Project As`. However the save as  
1942 does not copy the folder `<...>/Model/nCoVToolkit`, which must be copied into the  
1943 new simulation directory separately.

1944 `CompuCell3D Player` is a GUI tool which executes `CompuCell3D` simulations  
1945 during desktop execution (or on nanoHUB). In order to run the simulation either right click  
1946 *VirallInfectionVTM.cc3d* in the left hand panel and select "Open In Player" or open  
1947 *CompuCell3D.exe* to open the `CompuCell3D Player` and select `File; Open`  
1948 `Simulation File` and open *VirallInfectionVTM.cc3d*. Once the simulation is open in  
1949 Player click play (on the nanoHub deployment the simulation should start automatically).  
1950 Player will display windows with the cell lattice rendered (Fig S14), set the z-plane to 0 to  
1951 visualize the epithelial cells and the z-plane to 1 to visualize the immune cells. More  
1952 windows can be created (menu `Window; New graphics Window`, Fig S15) as  
1953 needed to visualize the virus, cytokine, oxidative agent fields. Each window has a drop-  
1954 down menu containing the selection of fields that can be rendered (i.e., the chemical fields  
1955 and the cell field, Fig S16).

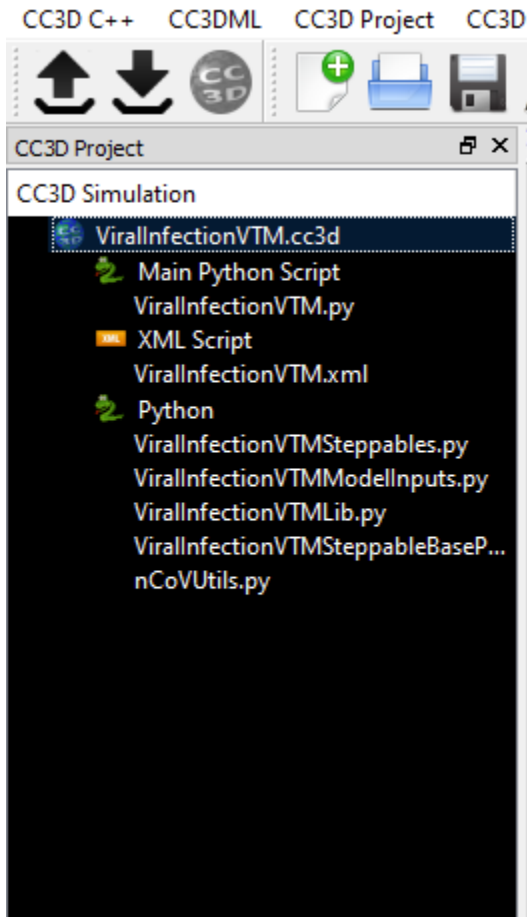
1956

1957



1958

**Fig S12. Opening a CompuCell3D project in Tweedit++.**

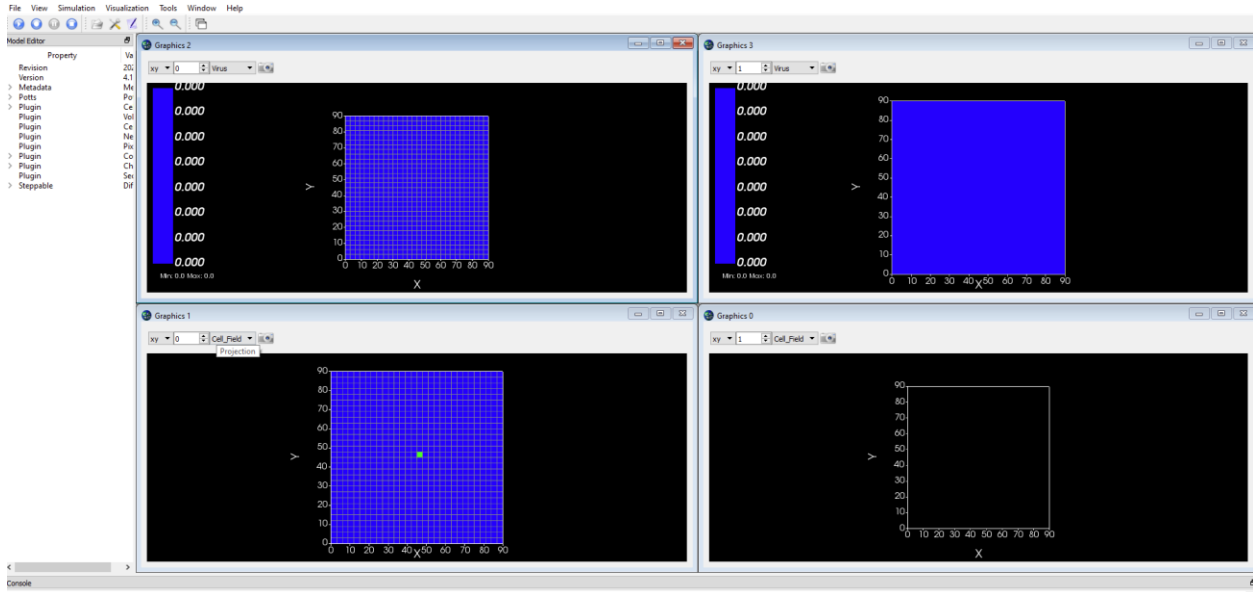


1959

1960

**Fig S13. Tweedit++'s left hand panel with simulation project files opened.**

1961

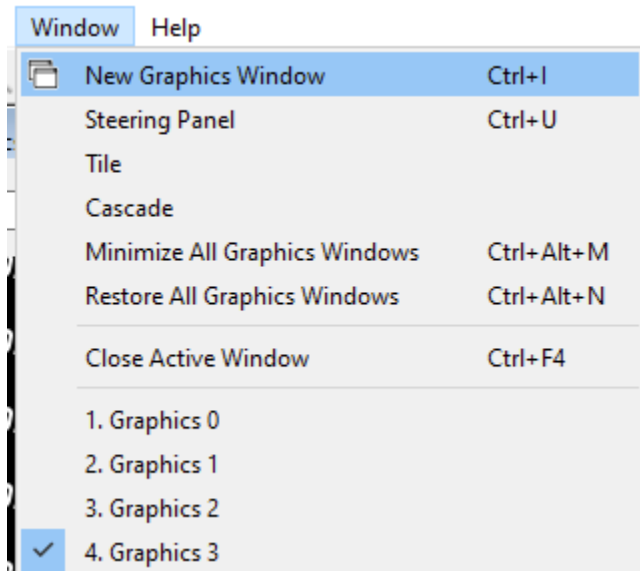


1962

1963

**Fig S14. Example of CompuCell3D's player open with the COVID-19 simulation loaded.**

1964

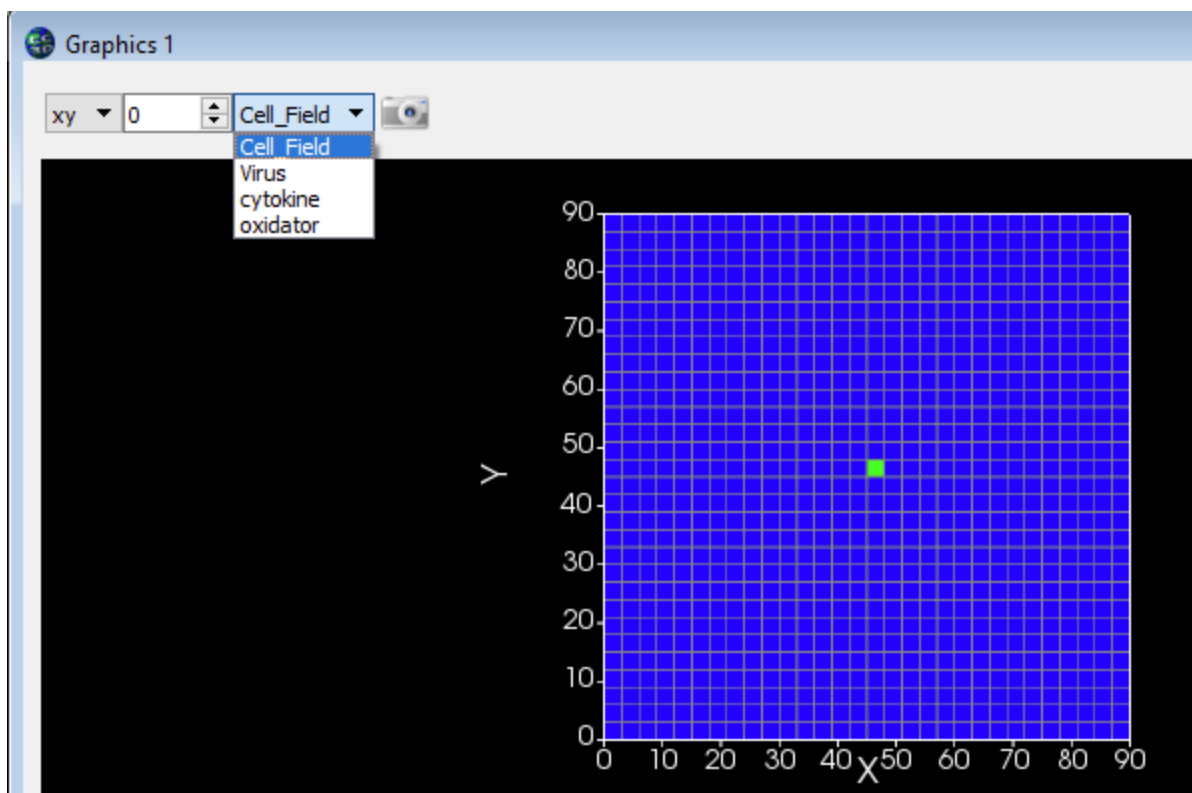


1965

1966

**Fig S15. How to open a new simulation render window in CompuCell3D Player.**

1967



1968

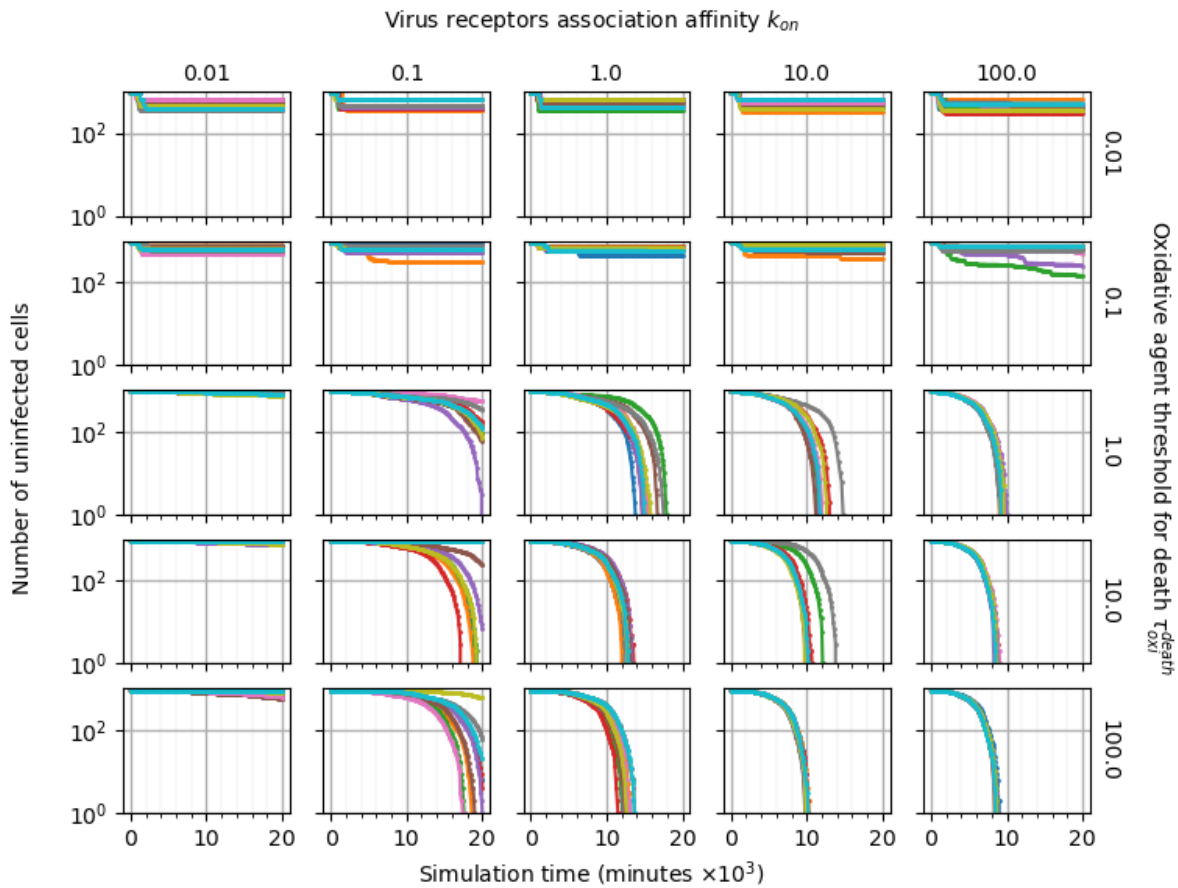
1969

**Fig S16.** Drop-down menu in simulation render window to select which field to render.

1970



1971 **Sensitivity analysis of the baseline parameter set**

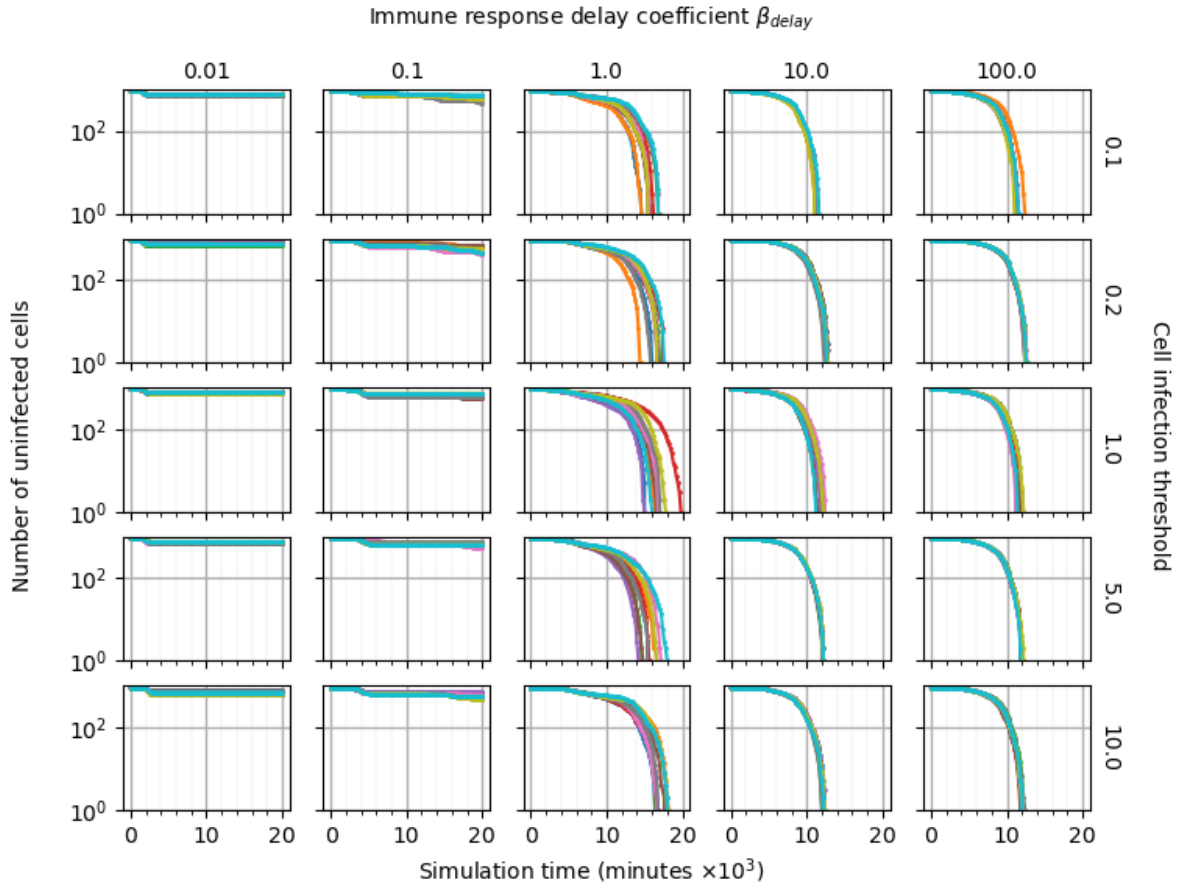


1972

1973 **Fig S17. Pairwise parameter sweep of the oxidative agent threshold for death  $\tau_{oxi}^{death}$  and the virus-receptor**  
1974 **association affinity  $k_{on}$  ( $\times 0.01, \times 0.1, \times 1, \times 10, \times 100$ ) around their baseline values, with ten simulation**  
1975 **replicas per parameter set (all other parameters have their baseline values as given in Table 1).**

1976 The number of uninfected epithelial cells for each simulation replica for each parameter set, plotted on a logarithmic  
1977 scale, vs time displayed in minutes.

1978

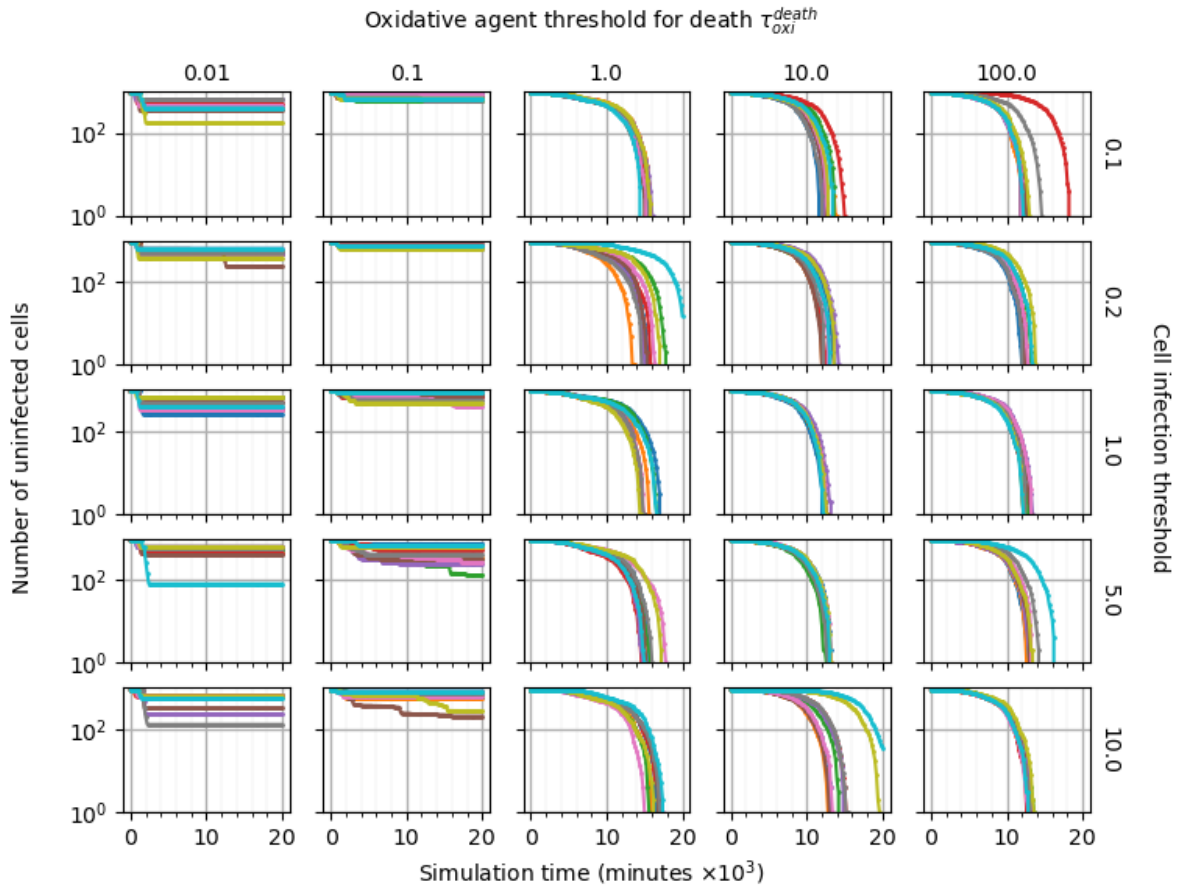


1979

1980 **Fig S18. Pairwise parameter sweep of the immune response delay  $\beta_{delay}$  ( $\times 0.01, \times 0.1, \times 1, \times 10, \times 100$ ) and**  
1981 **infection threshold ( $\times 0.1, \times 0.2, \times 1, \times 5, \times 10$ ) around their baseline values, with ten simulation replicas per**  
1982 **parameter set (all other parameters have their baseline values as given in Table 1).**

1983 The number of uninfected epithelial cells for each simulation replica for each parameter set, plotted on a logarithmic  
1984 scale, vs time displayed in minutes.

1985

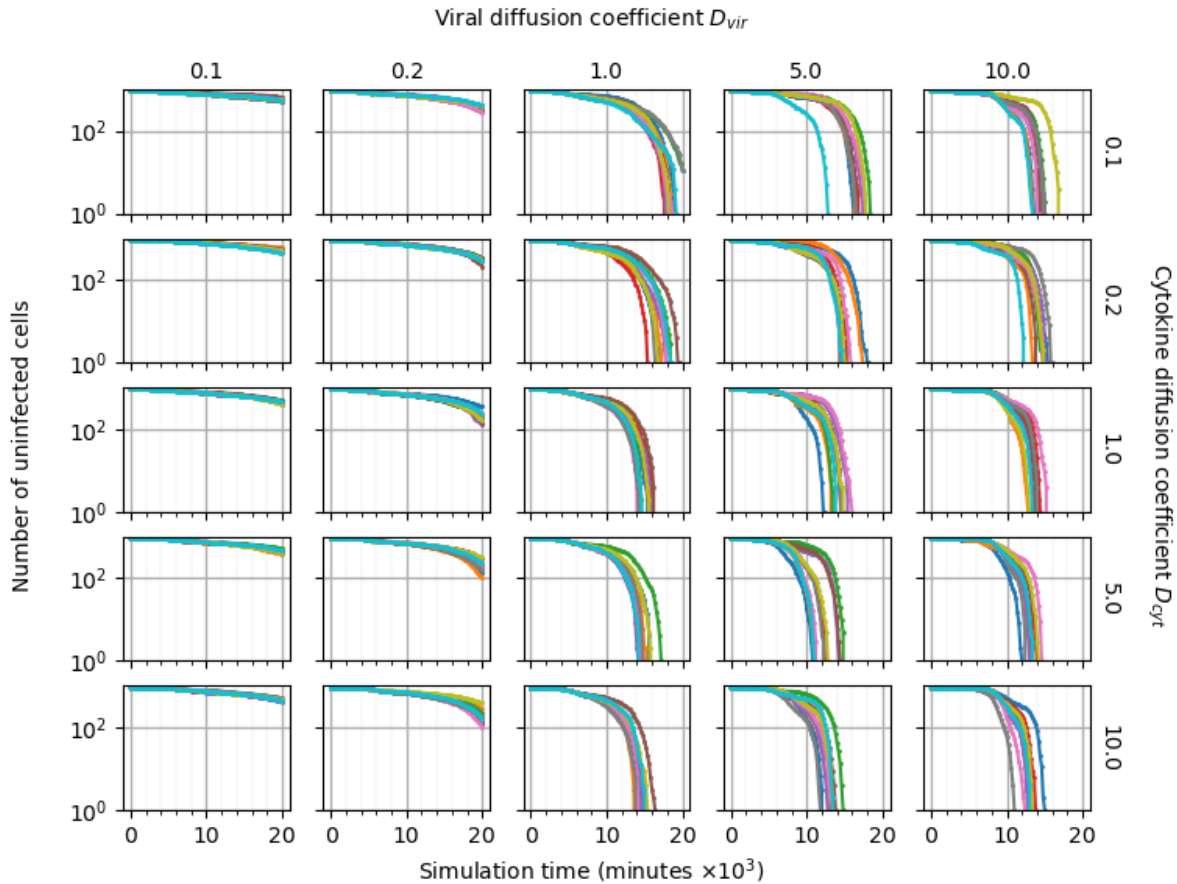


1986

1987 **Fig S19. Pairwise parameter sweep of the oxidative agent threshold for death  $\tau_{oxi}^{death}$  ( $\times 0.01, \times 0.1, \times 1, \times 10, \times$**   
1988  **$100$ ) and the infection threshold ( $\times 0.1, \times 0.2, \times 1, \times 5, \times 10$ ) around their baseline values, with ten simulation**  
1989 **replicas per parameter set (all other parameters have their baseline values as given in Table 1).**

1990 The number of uninfected epithelial cells for each simulation replica for each parameter set, plotted on a logarithmic  
1991 scale, vs time displayed in minutes.

1992



1993

1994 **Fig S20. Pairwise parameter sweep of the viral diffusion coefficient  $D_{vir}$  and the cytokine diffusion coefficient**

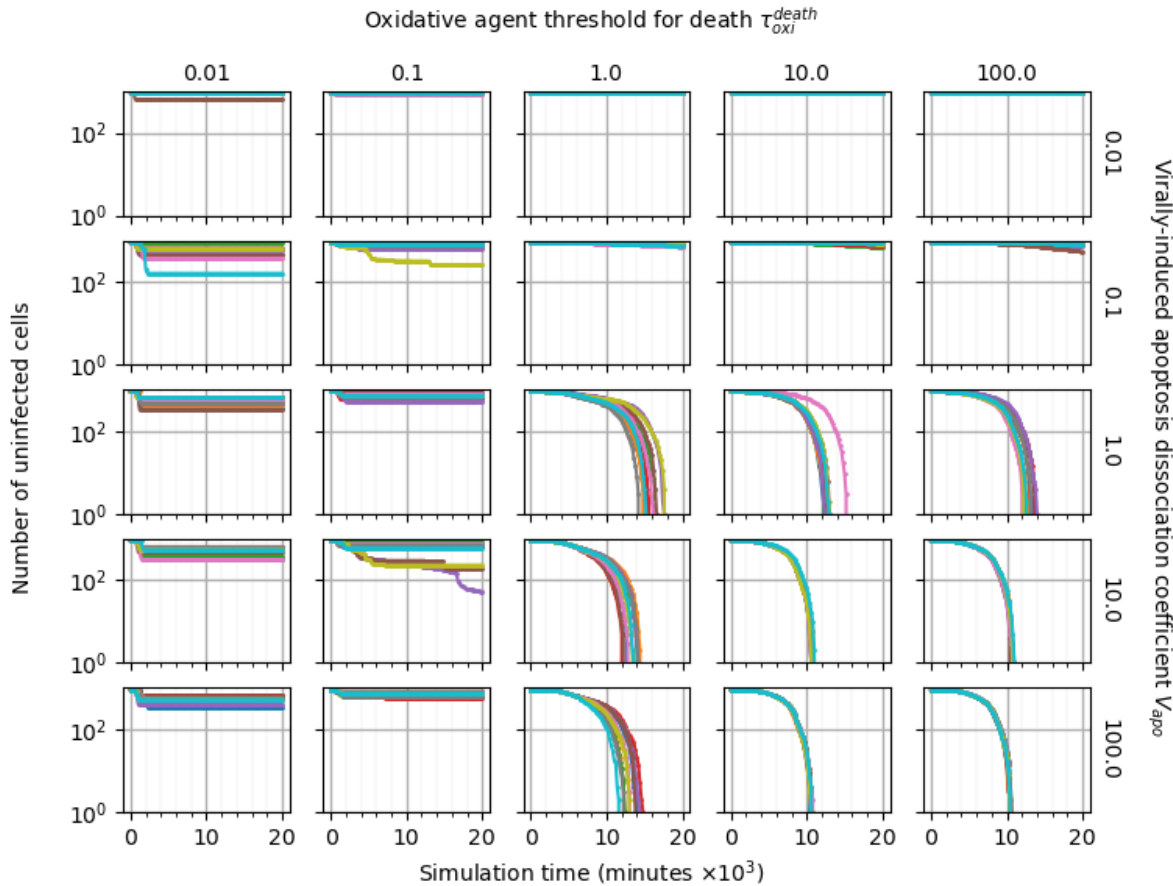
1995  **$D_{cyt}$  ( $\times 0.1, \times 0.2, \times 1, \times 5, \times 10$ ) around their baseline values, with ten simulation replicas per parameter set**

1996 **(all other parameters have their baseline values as given in Table 1).**

1997 The number of uninfected epithelial cells for each simulation replica for each parameter set, plotted on a logarithmic

1998 scale, vs time displayed in minutes.

1999

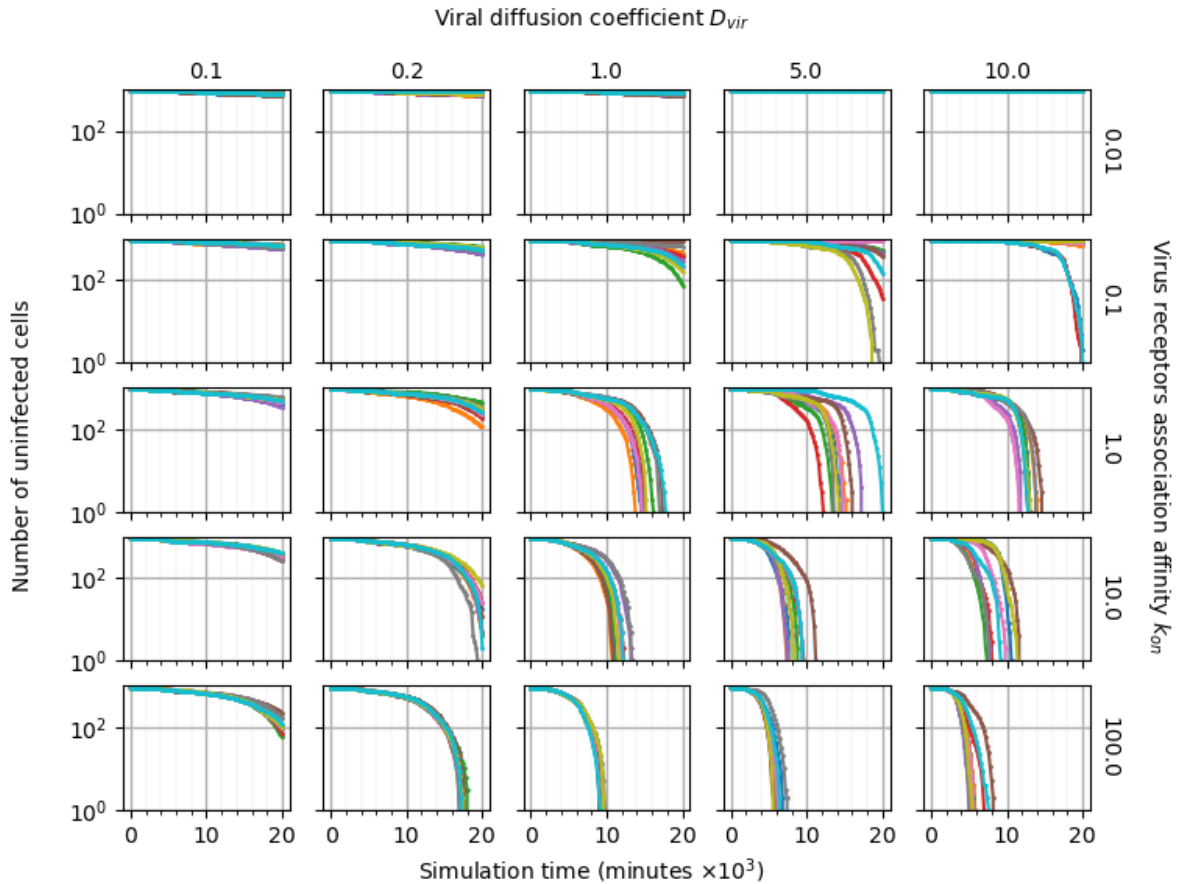


2000

2001 **Fig S21. Pairwise parameter sweep of the oxidative agent threshold for death  $\tau_{oxi}^{death}$  and the virally-induced**  
 2002 **apoptosis dissociation coefficient  $V_{apo}$  ( $\times 0.01, \times 0.1, \times 1, \times 10, \times 100$ ) around their baseline values, with ten**  
 2003 **simulation replicas per parameter set (all other parameters have their baseline values as given in Table 1).**

2004 The number of uninfected epithelial cells for each simulation replica for each parameter set, plotted on a logarithmic  
 2005 scale, vs time displayed in minutes.

2006



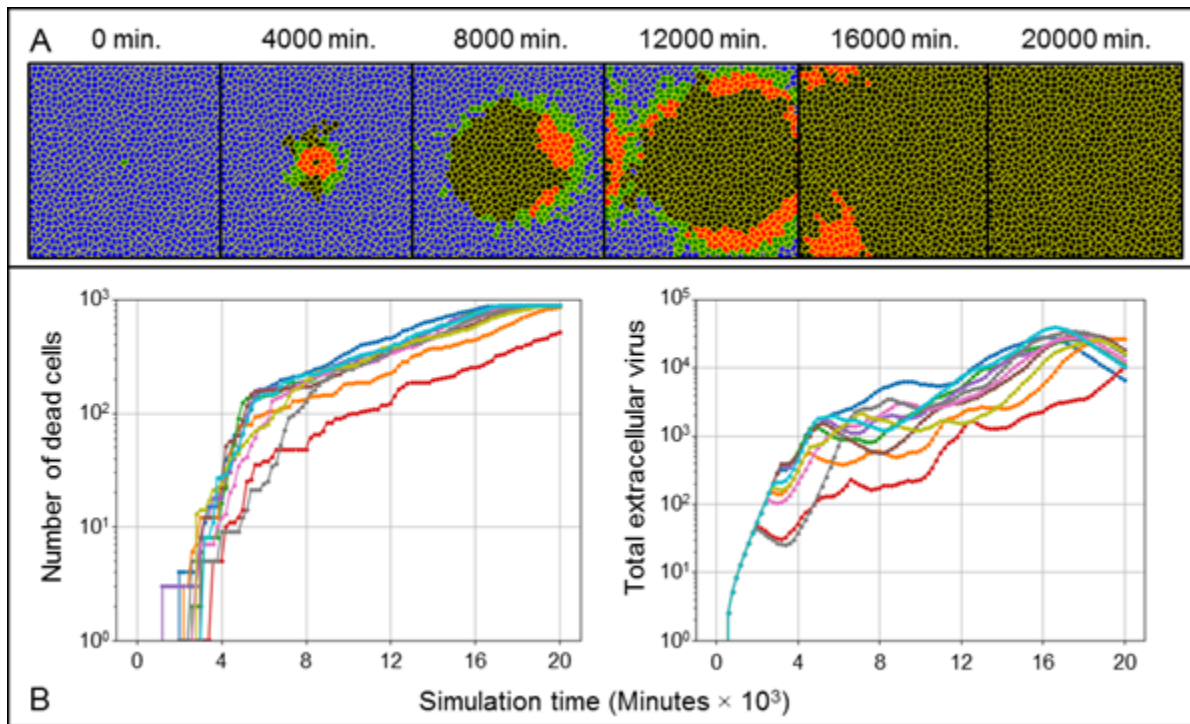
2007

2008 **Fig S22. Pairwise parameter sweep of the viral diffusion coefficient  $D_{vir}$  ( $\times 0.1, \times 0.2, \times 1, \times 5, \times 10$ ) and the**  
2009 **virus-receptor association affinity  $k_{on}$  ( $\times 0.01, \times 0.1, \times 1, \times 10, \times 100$ ) around their baseline values, with ten**  
2010 **simulation replicas per parameter set (all other parameters have their baseline values as given in Table 1).**

2011 The number of uninfected epithelial cells for each simulation replica for each parameter set, plotted on a logarithmic  
2012 scale, vs time displayed in minutes.

2013

2014 **A non-uniform epithelial sheet shows no significant effects in emergent dynamics**  
2015 **of simulation outcomes**



2016  
2017 **Fig S23. Simulation of viral infection using the baseline parameter set as in Fig 3 but with a non-uniform**  
2018 **epithelial sheet.**  
2019 (A) Widespread infection occurs with the same spatiotemporal features as in Fig 3A in a non-uniform epithelial sheet.  
2020 (B) Ten simulation replicas with a non-uniform epithelial sheet showed no significant differences in transient metrics  
2021 compared to simulations with a uniform epithelial sheet.

2022  
2023 **Integration of an explicit RNA synthesis model**

2024 The HCV model in [59] describes subgenomic replication in two compartments,  
2025 namely the cytoplasm and vesicular membrane structures (VMS). Integration with the  
2026 viral replication model described in *Quantitative model and implementation* requires the  
2027 two modifications, one to the HCV model, and one to the viral replication model of the  
2028 main framework, such that the viral genome taking part in genomic replication from (7) is



2029 a proxy for the cytoplasmic plus-strand RNA molecules of the HCV model. Both  
 2030 modifications are described here.

2031 According to the HCV model, in the cytoplasm,

$$2032 \quad \frac{dR_p^{cyt}}{dt} = k_2 T_c + k_{Pout} R_P - k_I R_{ibo} R_P^{cyt} - k_{Pin} R_P^{cyt} - \mu_P^{cyt} R_P^{cyt} + n_{HCV} r_u U, \quad (S1)$$

$$2033 \quad \frac{dT_c}{dt} = k_I R_{ibo} R_P^{cyt} - k_2 T_c - \mu_{Tc} T_c, \quad (S2)$$

$$2034 \quad \frac{dP^{cyt}}{dt} = k_2 T_c - k_c P^{cyt}, \quad (S3)$$

$$2035 \quad \frac{dE^{cyt}}{dt} = k_c P^{cyt} - k_{Ein} E^{cyt} - \mu_E^{cyt} E^{cyt}, \quad (S4)$$

2036 where  $R_p^{cyt}$  is the number of plus-strand HCV RNA molecules in the cytoplasm,  $T_c$  is the  
 2037 number of translation complexes in the cytoplasm,  $P^{cyt}$  is the number of HCV polyprotein  
 2038 molecules in the cytoplasm,  $E^{cyt}$  is the number of enzyme NS5B and other viral proteins  
 2039 needed for RNA synthesis in the cytoplasm,  $R_{ibo}$  is the number of host cell ribosomes  
 2040 ( $R_{ibo} = R_{ibo}^{tot} - T_c$  for fixed total available ribosomes  $R_{ibo}^{tot}$ ), and  $n_{HCV}$  relates  $R_p^{cyt}$  to unitless  
 2041  $R$ . Simulations of the HCV model were performed as in [59] by initializing  $R_p^{cyt}$  with an  
 2042 initial nonzero value in the initially infected cell. In the case of a spatial context, where  
 2043 cells are infected at various times according to progression of infection and subsequent  
 2044 internalization events, subgenomic replication within a particular cell occurs due to  
 2045 internalization of virus by the cell (6). As such, the final term of (S1) was added during  
 2046 integration such that internalized virus acts as a source for  $R_p^{cyt}$ .

2047 Likewise, in the VMS,

$$2048 \quad \frac{dR_P}{dt} = -k_3 R_P E + k_{4p} R_{Ids} + k_{Pin} R_P^{cyt} - (k_{Pout} + \mu_P) R_P, \quad (S5)$$

$$2049 \quad \frac{dR_{ds}}{dt} = k_{4m} R_{Ip} + k_{4p} R_{Ids} - k_5 R_{ds} E - \mu_{ds} R_{ds}, \quad (S6)$$

$$2050 \quad \frac{dE}{dt} = k_{Ein} E^{cyt} + k_{4m} R_{Ip} + k_{4p} R_{Ids} - k_3 R_P E - k_5 R_{ds} E - \mu_E E, \quad (S7)$$

$$2051 \quad \frac{dR_{Ip}}{dt} = k_3 R_P E - k_{4m} R_{Ip} - \mu_{Ip} R_{Ip}, \quad (S8)$$

$$2052 \quad \frac{dR_{Ids}}{dt} = k_5 R_{ds} E - k_{4p} R_{Ids} - \mu_{Ids} R_{Ids}, \quad (S9)$$

2053 where  $R_P$  is the number of plus-strand RNA in the VMS,  $R_{ds}$  is the number of dsRNA in  
 2054 the VMS,  $E$  is the number of HCV polymerase complexes in the VMS,  $R_{Ip}$  is the number  
 2055 of plus-strand RNA replicative intermediate complexes in the VMS and  $R_{Ids}$  is the number  
 2056 of plus-strand dsRNA replicative intermediate complexes in the VMS.

2057 Having selected  $R_P^{cyt}$  and  $R$  as the shared biological object of the two models, mass  
 2058 action  $R \rightarrow P$  of the viral replication model of the main framework requires modification.  
 2059 We assume that decay of  $R_P^{cyt}$  described in the HCV model leads to production of  $P$   
 2060 through intermediate processes. The viral replication model of the main framework ((6)–  
 2061 (10)) then takes the modified form,

$$2062 \quad \frac{dU}{dt} = U_{take} - r_u U, \quad (S10)$$

$$2063 \quad n_{HCV} R = R_P^{cyt}, \quad (S11)$$

2064 
$$\frac{dP}{dt} = r_t' R - r_p P, \quad (\text{S12})$$

2065 
$$\frac{dA}{dt} = r_p P - \text{Release}, \quad (\text{S13})$$

2066 where  $r_t'$  is the rate of production of  $P$  per unit of  $R$  associated with decay of  $R_p^{cyt}$ . Note  
 2067 that without the introduction of additional decay to the HCV model equations, the  
 2068 integrated form of the HCV model effectively acts the same as its original form within each  
 2069 cell, subject to the cellular and spatial aspects of internalization events. All parameters of  
 2070 the integrated HCV model in simulations shown in *Particularization to hepatitis C virus by*  
 2071 *integration of an explicit RNA synthesis model* were taken from [59] (Table S2).

2072

2073 **Table S2. Parameter values of integrated HCV model.**

Simulation parameters	Value
$T_c$ formation rate $k_1$	4800 molecule <sup>-1</sup> min. <sup>-1</sup>
Nascent polyprotein cleavage rate $k_2$	6000 min. <sup>-1</sup>
Viral polyprotein cleavage rate $k_c$	36 min. <sup>-1</sup>
$R_p^{cyt}$ transport rate into cytoplasm $k_{pin}$	12 min. <sup>-1</sup>
$R_p$ transport rate into VMS $k_{pout}$	12 min. <sup>-1</sup>
$E^{cyt}$ transport rate in VMS $k_{Ein}$	7.8×10 <sup>-4</sup> min. <sup>-1</sup>
$R_{Ip}$ formation rate $k_3$	1.2 molecule <sup>-1</sup> min. <sup>-1</sup>
$R_p$ synthesis rate $k_{Ap}$	102 min. <sup>-1</sup>
$R_{ds}$ synthesis rate $k_{Am}$	102 min. <sup>-1</sup>
$R_{Ids}$ formation rate $k_5$	240 min. <sup>-1</sup>
$R_p^{cyt}$ degradation rate $\mu_p^{cyt}$	600 min. <sup>-1</sup>
$R_p$ degradation rate $\mu_p$	4.2 min. <sup>-1</sup>
$R_{ds}$ degradation rate $\mu_{ds}$	3.6 min. <sup>-1</sup>

$R_{Ip}$ degradation rate $\mu_{Ip}$	2.4 min. <sup>-1</sup>
$R_{Ids}$ degradation rate $\mu_{Ids}$	7.8 min. <sup>-1</sup>
$T_c$ degradation rate $\mu_{Tc}$	0.9 min. <sup>-1</sup>
$E$ degradation rate $\mu_E$	2.4 min. <sup>-1</sup>
$E^{cyt}$ degradation rate $\mu_E^{cyt}$	3.6 min. <sup>-1</sup>
Total number of available ribosomes $R_{ibo}^{tot}$	700
RNA conversion factor $n_{HCV}$	100 molecule $R^{-1}$
$P$ production rate $r_t'$	2.5 min. <sup>-1</sup> $R^{-1}$

2074

## 2075 Collaborative viral infection modeling environment

2076           Given the immense amount of complexity associated with viral infection,  
2077 supporting collaborative, independent, concurrent, and even conflicting, model  
2078 development is critical to building an informative and predictive multiscale model of viral  
2079 infection. As such, the simulation architecture developed for the CompuCell3D  
2080 implementation, as demonstrated in *Model extensions*, supports development,  
2081 deployment and distribution of add-on modules following the Python programming  
2082 language design principles and practices of extensibility and modularity. This architecture  
2083 exploits the architecture of CompuCell3D itself, specifically, that model implementation in  
2084 CompuCell3D consists of designing a set of Python classes called “steppables”, each of  
2085 which is imported into CompuCell3D and simulated (via exactly two simple lines of Python  
2086 code per steppable, see *Deploying a model extension in CompuCell3D*). Each steppable  
2087 typically implements a particular model, function, or feature (e.g., viral internalization, data  
2088 post-processing and exporting), and provides instructions to CompuCell3D about what to  
2089 do during each simulation step along with the core simulation engine (e.g., implementing

2090 the Cellular Potts Model), as well as what to do before and after simulation, through a  
2091 simple interface (e.g., procedures to perform by a steppable during each simulation step  
2092 are described in a function “step” in the steppable class definition). This approach is  
2093 particularly well suited for supporting collaborative, independent, and concurrent model  
2094 development because model specification of a particular simulation in CompuCell3D  
2095 consists of selecting and loading a particular set of steppables, each of which can be  
2096 specified in separate Python scripts and packaged in uniquely named directories,  
2097 developed by collaborating or independent and otherwise disconnected research groups,  
2098 and intended to model specific biological phenomena. Furthermore, specification of  
2099 model implementations using Python classes also enables development of model  
2100 extensions from existing modules (whether from the main framework or an add-on  
2101 module) using basic Python class inheritance functionality (where class definitions can  
2102 be constructed from other class definitions and subsequently modified, see *Extending a*  
2103 *model in CompuCell3D*).

2104 We envision a community of modelers much like the community of Python  
2105 developers, which develops Python packages, called “modules”, that can be publicly  
2106 distributed and imported into software using a simple, one-line Python command (e.g.,  
2107 import MyModule). As such, we have built into the CompuCell3D implementation used in  
2108 this work a location for storing a library of add-on modules, as well as supporting  
2109 architecture to facilitate development and deployment of add-on modules. Furthermore,  
2110 along with making the simulation framework publicly available online as described in  
2111 *Downloading and running the simulation*, the online repository also hosts this library of  
2112 add-on modules as part of the standard download package, which we continue to develop

2113 and maintain, and for which we are currently developing standards (e.g., standard  
2114 documentation) and supporting tools (e.g., documentation generators). We welcome  
2115 usage by, and contributions from, all interested groups, and provide a basic overview of  
2116 deploying and developing model extensions in the remaining discussion of this section.

2117

2118 **Deploying a model extension in CompuCell3D.** As in any typical CompuCell3D  
2119 model specification, one script of the simulation files shown in Fig S13,  
2120 Simulation/ViralInfectionVTM.py, imports all modules of the main framework and loads  
2121 them into CompuCell3D for simulation. The directory “Simulation” contains all source  
2122 code of the main framework, while an additional directory “Models” is dedicated to  
2123 storing source code of the add-on module library. Each add-on module is an importable  
2124 Python module stored in its own, uniquely named subdirectory (e.g.,  
2125 Models/IUBIOCAAddons). Code Snippet S1 shows a section of the contents of  
2126 Simulation/ViralInfectionVTM.py for a simulation using the Simple Recovery model  
2127 described in *An extensible framework architecture enables the inclusion of tissue*  
2128 *recovery*.

2129

```
1 from ViralInfectionVTMSteppables import ViralInternalizationSteppable
2 CompuCellSetup.register_steppable(steppable=ViralInternalizationSteppable(frequency=1))
3
4 from Models.RecoverySimple.RecoverySteppables import SimpleRecoverySteppable
5 CompuCellSetup.register_steppable(steppable=SimpleRecoverySteppable(frequency=1))
```

2130

2131 **Code Snippet S1. Select import and load commands from Simulation/ViralInfectionVTM.py.**



2132

2133           Lines 1 and 2 in Code Snippet S1 import and load the steppable  
2134 “VirallInternalizationSteppable” that implements the internalization model described in *E1*  
2135 - *Viral internalization* from Simulation/ViralInfectionVTMSteppables.py. Lines 4 and 5  
2136 show that not much is different concerning loading and importing add-on modules. The  
2137 steppable “SimpleRecoverySteppable” implements the Simple Recovery Model, and is  
2138 defined in Models/RecoverySimple/RecoverySteppables.py. The only difference between  
2139 importing and loading a module from the main framework or add-on module library is  
2140 specifying the location of the Python script containing the steppable to be deployed in a  
2141 simulation. This way, two model modules can define steppables in Python scripts of the  
2142 same name without overwriting each other (e.g., Models/GroupX/Steppables.py or  
2143 Models/GroupY/Steppables.py). The only necessarily unique aspect of a particular model  
2144 module is the name of its containing directory (e.g., the directory Models/GroupX or  
2145 Models/GroupY). This scheme isolates model-specific development to the directory in  
2146 which the add-on model is defined, and modularizes the overall simulation framework into  
2147 *shareable, interchangeable* model components. Furthermore, since development of add-  
2148 on modules is isolated to a uniquely named directory, the framework promotes concurrent  
2149 development and implementation of unrelated or even competing models.

2150

2151 **Developing a Model Extension in CompuCell3D.** Developing a model extension is as  
2152 simple as the typical CompuCell3D model implementation procedure of developing  
2153 steppables in Python using the CompuCell3D steppable class “SteppableBasePy” (see

2154 *Extending a model in CompuCell3D* for discussion of Python class inheritance). Code  
2155 Snippet S2 shows the application programming interface (API) and select code from the  
2156 Python script `Models/RecoverySimple/RecoverySteppables.py` in the add-on module  
2157 library that implements the Simple Recovery model described in *An extensible*  
2158 *framework architecture enables the inclusion of tissue recovery*.  
2159

```
1  import sys
2  import os
3  # Import from simulation environment
4  sys.path.append(os.environ["ViralInfectionVTM"])
5  # Import parameter values from RecoveryInputs.py and other stuff
6  from .RecoveryInputs import *
7  from Simulation.ViralInfectionVTMModelInputs import s_to_mcs
8  import random
9  from cc3d.core.PySteppables import *
10
11 class SimpleRecoverySteppable(SteppableBasePy):
12     def __init__(self, frequency=1):
13         """
14         Initialize recovery steppable
15         """
16
17     def start(self):
18         """
19         Share self with framework
20         """
21
22     def step(self, mcs):
23         """
24         Perform recovery test in each dead cell
25         """
26
27     def recover_cell(self, _cell):
28         """
29         Implement recovery
30         """
31
32     def cell_recovers(self, _cell) -> bool:
33         """
34         Test for simple recovery in a cell
35         """
36         return random.random() < recovery_rate * s_to_mcs
```

2160

2161 **Code Snippet S2. API for the steppable implementing the Simple Recovery model, derived from**  
2162 **Models/RecoverySimple/RecoverySteppables.py.**

2163 The exact code of the implementation is shown for the steppable function "cell\_recovers" (Lines 32-36).

2164

2165           Lines 1-4 in Code Snippet S2 add the directory containing both the main framework  
2166 and add-on modules library directories using the environment variable  
2167 “VirallInfectionVTM”, which makes both available to any module loaded into CompuCell3D  
2168 from Simulation/VirallInfectionVTM.py, whether directly or indirectly (e.g., when  
2169 Simulation/VirallInfectionVTM.py imports module “A” that imports module “B”). Line 6  
2170 imports parameter values of this module defined in  
2171 Models/RecoverySimple/RecoveryInputs.py, while Line 7 imports a parameter value from  
2172 the main framework for use in calculations. Line 8 imports the Python standard module  
2173 “random” for generating random numbers, which, like the rest of the Python standard  
2174 library and many others, is distributed with CompuCell3D. Line 9 imports everything from  
2175 the CompuCell3D module “PySteppables”, which contains the available Python classes  
2176 for Python model implementation in CompuCell3D.

2177           Line 11 in Code Snippet S2 begins the definition of the Simple Recovery model  
2178 steppable, “SimpleRecoverySteppable”. SimpleRecoverySteppable inherits from  
2179 “SteppableBasePy”, a steppable class defined in the PySteppables module. Its first three  
2180 functions, “\_\_init\_\_”, “start”, and “step”, are all functions of the CompuCell3D steppable  
2181 interface. “\_\_init\_\_” defines the procedures to be performed for initializing the steppable.  
2182 “start” defines the procedures to be performed after CompuCell3D has initialized but  
2183 before simulation begins (in the case of this steppable, sharing a reference to itself with  
2184 the rest of the framework). “step” defines the procedures to be performed during each  
2185 simulation step (in this case of this steppable, evaluating recovery in each dead cell and

2186 executing recovery when it occurs). The final two functions are specific to this steppable.  
2187 The first, “recover\_cell”, performs the necessary procedures associated with recovery on  
2188 a cell when given one as an argument (*i.e.*, “\_cell”). The second, “cell\_recovers”,  
2189 evaluates whether or not a particular cell is recovered. It should be noted that deployment  
2190 of the SimpleRecoverySteppable class is not limited to usage directly in CompuCell3D as  
2191 a simulated steppable. Rather, like the importing of a parameter value from the main  
2192 framework in Line 7 of Code Snippet S2, the SimpleRecoverySteppable class can be  
2193 imported into other modules for other purposes, like performing recovery of a dead cell  
2194 but due to an alternative recovery criterion. The following section describes an example  
2195 of such functionality.

2196  
2197 **Extending a model in CompuCell3D.** Like any other Python class, steppables (and  
2198 other code) defined in one model module can be extended by, or integrated into, other  
2199 modules, such that the components of the overall simulation framework are not only  
2200 interchangeable and shareable, but also extensible. In the previous section, Code  
2201 Snippet S2 demonstrated the ability to import a parameter value (*i.e.*, “s\_to\_mcs”, Line  
2202 7) from the main framework for usage in an add-on module. The same can be done for  
2203 integrating modules (whether from the main framework or add-on library) into other add-  
2204 on modules, as well as for extending model modules using Python class inheritance.  
2205 Python class inheritance enables the construction of classes from the definition of other  
2206 classes, such that functionality and interfaces defined by one class can be employed,  
2207 selectively adapted, and extended, by subsequent classes that inherit from it. Any  
2208 inheriting class, called a “derived class”, can replace (*i.e.*, “overwrite”) the executed

2209 code of a function in the definition of an inherited class, called a “base class”, if the  
2210 derived class defines a function with the same name and arguments. All inherited  
2211 functions that are not overwritten by a derived class are the same.

2212 Simulation results of the Neighbor Recovery model in *An extensible framework*  
2213 *architecture enables the inclusion of tissue recovery* demonstrate deployment using the  
2214 framework capability of constructing add-on modules from other add-on modules.  
2215 Computationally, nearly all aspects of the Recovery Model are the same as the Simple  
2216 Recovery model (e.g., test for recovery in every cell during each simulation step,  
2217 implement recovery when it occurs). The only difference between the two models is the  
2218 criterion by which recovery of a dead cell is evaluated, making the implementation of the  
2219 Neighbor Recovery model a strong candidate for exploiting Python class inheritance, as  
2220 demonstrated in Code Snippet S3.

2221

```
1 import sys
2 import os
3 # Inherit from Simple Recovery model
4 sys.path.append(os.environ["ViralInfectionVTM"])
5 from Models.RecoverySimple.RecoverySteppables import SimpleRecoverySteppable
6
7 class NeighborRecoverySteppable(SimpleRecoverySteppable):
8     def __init__(self, frequency=1):
9         super().__init__(frequency)
10
11     def cell_recovers(self, _cell) -> bool:
12         """
13         Test for neighbor-dependent recovery in a cell
14         """
```

2222



2223 **Code Snippet S3. API for the steppable implementing the Simple Recovery model, derived from**  
2224 **Models/RecoveryNeighbor/RecoverySteppables.py.**

2225

2226       As in Code Snippet S2, Lines 1-4 of Code Snippet S3 makes available the entire  
2227 framework, while Line 5 imports the Simple Recovery model steppable definition for  
2228 extension. Line 7 begins the definition of the steppable “NeighborRecoverySteppable”  
2229 that implements the Neighbor Recovery model by inheriting from the class definition for  
2230 the Simple Recovery model “SimpleRecoverySteppable”. Since all functionality of the  
2231 Neighbor Recovery steppable is to be the same as the Simple Recovery steppable except  
2232 for the recovery criterion, Lines 8-9 initialize the Neighbor Recovery steppable exactly the  
2233 same as the Simple Recovery steppable. Lines 11-14 begin overwriting the definition of  
2234 the recovery criterion from Simple Recovery according to the Neighbor Recovery model.  
2235 Since no other functions of the Simple Recovery steppable are overwritten, they are then  
2236 exactly the same for the Neighbor Recovery steppable. Furthermore, since the signature  
2237 of the function that implements the recovery criterion (*i.e.*, “cell\_recovers(self, \_cell)”) has  
2238 the exact same name and arguments in both steppables (*i.e.*, the function “cell\_recovers”  
2239 is overwritten by NeighborRecoverySteppable), they can be used in the exact same way  
2240 by other modules (e.g., a variable “my\_recovery\_steppable”, whether an instance of  
2241 SimpleRecoverySteppable or NeighborRecoverySteppable, receives and returns the  
2242 same type of information). The only difference in behavior between using one or the other  
2243 is the potential outcome of asking either recovery steppable whether or not a particular  
2244 dead cell recovers, about which the two models will often disagree.